ENERGY DEPLETION CAUSES ENDOTHELIAL HYPERPERMEABILITY IN HYPERGLYCEMIA

by

STEWART RUSSELL

A dissertation submitted to the Graduate Faculty in Engineering in partial fulfilment of the requirements for the degree of Doctor of Philosophy, The City University of New York

2008

This manuscript has been read and accepted for the
Graduate Faculty in Engineering in satisfaction of the
dissertation requirement for the degree of Doctor of Philosophy.

18 Sept 2008	Professor David Rumschitzki, Ph.D.
Date	Chair of Examining Committee
18 Sept 2008	Dean Mumtaz K. Kassir, Ph.D.
Date	Executive Officer

Professor John Tarbell, Ph.D.

Professor Bingmei Fu, Ph.D.

Professor Akira Kawaguchi, Ph.D.

Kung-ming Jan, M.D. Ph. D., Columbia University

Supervision Committee

THE CITY UNIVERSITY OF NEW YORK

Abstract

ENERGY DEPLETION CAUSES ENDOTHELIAL HYPERPERMEABILITY IN HYPERGLYCEMIA

by

Stewart Russell

Advisor: Professor David S. Rumschitzki, Ph.D.

Diabetes is strongly correlated to an increased risk of cardiovascular disease (CVD). Reduced endothelial barrier function has been identified as a result of unregulated hyperglycemia in diabetes, and as risk factor in the development of atherosclerosis. Endothelial barrier dysfunction is measured by hyperpermeability to water and solutes, and by reduced dynamic response to a change in pressure. To investigate the relationship between endothelial dysfunction and high blood glucose we cultured bovine aortic endothelial cells (BAEC) in confluent monolayers on polycarbonate filters in a series of increasing glucose concentrations from 5mM (normal) to 30mM (hyperglycemic) for use in a pressure-flow apparatus, with which we measured the hydraulic conductivity of water, and the convective and diffusive transport of low-density lipoprotein (LDL) through the monolayers in response to a 10-cmH_2O transmural pressure gradient. We developed a mathematical model of intracellular protein diffusion to extract parameters from this data to quantify the initial water volume flow rate (flux), the rate of attenuation of flow by the endothelial sealing effect, and the steady-state flux. Analysis of these extracted parameters revealed that endothelial monolayers grown in high glucose media have a statistically higher permeability to water and solute compared to cells grown in normal glucose media. Steady state hydraulic conductivity increased by 57.9 ±

10.0 % at 30 mM glucose, and by 30.1 ± 12.3 % at the physiologically relevant level of 10 mM glucose, compared to normal. A similar trend was observed for the initial water flux for the same conditions. Permeability to LDL increased by 46.8 ± 14.1 % at 30 mM glucose, and 42.1 ± 8.1 % at 10 mM glucose. Further analysis revealed that the dynamic response of cells grown in high glucose was significantly slower at physiological levels of hyperglycemia. We conducted parallel investigations into the effect of the depletion of adenosine tri-phosphate (ATP), caused either by 1) high glucose mediated activation of the DNA repair enzyme poly(ADP-ribose) polymerase (PARP), or 2) antimycin-A induced chemical impairment of the mitochondria. Our results support the hypothesis that increased steady-state hydraulic conductivity and LDL permeability are strongly linked to ATP depletion independent of mechanism.

Acknowledgements

Without these people, this work could not have been accomplished: David Rumschitzki, Ph.D., mentor, John Tarbell, Ph.D., Bingmei Fu, Ph.D., Akira Kawaguchi, Ph.D.. Morton Denn, Ph.D., Tieuvi Nguyen, Ph.D., Limary Cancel, Jimmy Toussaint, Yan Xue. This work was partially funded by the National Institues of Health grant number 1RO1HL67383, and by the Benjamin Levich Institute of Physio-chemical Hydrodynamics NSF IGERT grant in Soft Materials and Multi-Scale Phenomena number DGE-0221589. My doctoral research was partly funded by the Office of Student Programs at CUNY. My CUNY Dissertation Year Fellowship was funded by the very generous gift of Ms. Barbara Slifka, to whom I am most exceedingly grateful.

Table of Contents

List of Tables

Table of Figures

Chapter 1. Introduction

Background: Diabetes

Diabetes mellitus is the sixth leading cause of death in the United States, the direct cause of over 69,000 deaths and a contributing factor in over 200,000 deaths in 2000. The National Institutes of Health states that diabetes is underreported as a cause of death (National Institute of Diabetes and Digestive and Kidney Diseases 01/07/2005). Additionally, the risk of cardiovascular disease (CVD) for those with diabetes, is more than double the norm for men, (5.4:2.6), and more than three times normal for women (3.5:1.1) (Rosamond, Flegal *et al.* 2008). Diabetes is correlated so strongly with cardiovascular disease that it has been argued that it should be classified as a premature form of cardiovascular failure (Fisher 2004).

The timescale of diabetic complications is on the order of years, with most symptoms developing within 10 to 20 years of the onset of the disease. But the cellular mechanisms identified in the pathogenesis of diabetes operate on a much shorter time scale, typically hours or days. The central challenge in identifying the causes of diabetic complications in the lab is to find changes that have a short-term effect large enough to detect and a clear correlation to long-term complications. As we shall argue below, a synthesis of the results of research in the pathogenesis of diabetes, cancer therapy, and cellular metabolism suggests a method that may allow for the quantification of some long-term effects of high glucose by examining the kinetics of intracellular energy supply and demand.

Diabetes is a disease characterized by a lack of insulin, or decreased activity of insulin. Low insulin levels or activity disrupt the glucoregulatory mechanisms in the liver and muscle cells, causing chronic systemic hyperglycemia. This manifests itself as an elevated level of blood glucose (> 10mM) compared to normal (5 mM) and an impaired ability to take up and store glucose by insulin-sensitive cells in the liver and skeletal muscle. Almost all cells depend on glucose for energy in the form of adenosine triphosphate (ATP) upon which virtually every cell process—protein production, signalling, movement, adhesion, replication—depends. Two pathways exist by which ATP is synthesized, glycolysis, an enzymatic reaction, and oxidative phosphorylation, which occurs in the mitochondria. The brain, which does not store glucose, depends on a constant external glucose supply, which comes from the release of glucose from the liver and muscles. Although a few minutes reserve is dissolved in our blood at any moment—about 15 g, the liver and muscles can store over 1 kg of glucose in a high-molecular weight form. From the point of view of the brain, the body serves as a glucose battery, providing a steady current of glucose during times of energetic need, and recharging glucose stores in times when energy expenditure is low. Eating a normal meal causes a massive short-term influx of glucose—more than 10 times our normal resting level dissolved in our blood. Without the action of insulin, we lose the ability to store this extra glucose in the muscles and liver, and our blood glucose level will continue to rise. Although this may be over 5 fold of the normal blood glucose level, it is still not enough to sustain the body. In acute hyperglycemia the body is actually starving, and additional metabolism of fat and protein leads to toxic levels of ketones and acidic by-products, with eventual catastrophic general systemic failure. Although the short-term effects of

hyperglycemia can be fatal if untreated, infusion of exogenous insulin can restore the glucoregulatory mechanism, and when treated according to current medical practice, acute hyperglycemia is not the principal form of morbidity. By contrast, the long term effects of chronic moderate to high glucose levels have proven to be much more difficult to regulate, and although they are not immediately fatal, can lead to increased incidence of the diseased state through a variety of mechanisms discussed in the next sections.

Cell Dysfunction, Diabetic Complications, and Atherosclerosis

Cell dysfunction is the underlying cause of diabetic complications. However, it is in the cells that are not insulin sensitive that the greatest harmful effects are found. Cells such as the renal epithelium, retinal ganglion, peripheral neurons, and vascular endothelium are found to dysfunction through a variety of altered genetic, structural, and protein-mediated functions. Glucose is the principal nutritional substrate for these tissues, and it is a peculiar biological irony that an excess of nutrient seems to be the cause of cellular pathology. High glucose levels have been correlated to the incidence of diabetic retinopathy, neuropathy, nephropathy, microvascular complications, and atherosclerosis(Gabbay 1975; Najemnik, Sinzinger *et al.* 1999; Sheetz and King 2002).

It is the barrier function of the endothelium as it pertains to the development of atherosclerosis in diabetes in which we are principally interested. Recent advances in the understanding of the growth of atherosclerotic plaques allow us to work from the inside-out; knowing the preconditions for atherosclerosis allows us to infer what postconditions most likely result from unregulated hyperglycemia. Using an established cell culture model for the study of trans-endothelial transport, we undertake to investigate the

molecular mechanisms that underlie the endothelial dysfunction that is known to be relevant in the development of atherosclerosis.

Molecular Pathways to Cell Dysfunction

Five molecular pathways of the pathogenesis of diabetic complications have been validated by previous experimental investigation: 1) the polyol, or Aldose Reductase pathway (AR); 2) the accumulation of advanced glycation end-products (AGE) produced by non-enzymatic glycation of proteins; 3) inappropriate activation of protein kinase C (PKC); 4) increased flux through the hexosamine pathway (HX); 5) and the formation of reactive oxygen species (ROS).

The polyol pathway theory identifies an increase in the activity of aldose reductase (AR), a necessary cytoplasmic enzyme which converts the glucose metabolite galactose to galactitol. This model proposes osmotic vascular damage (Gabbay 1975), reduced nitric oxide production (Tesfamariam 1994), and altered enzymatic activity as the principal mechanisms of pathology (Williamson, Chang *et al.* 1993). Increased activity of this enzyme leads to the intracellular accumulation of non metabolized sorbitol and fructose and the disruption of the mitochondrial proton shuttle system by creating imbalances in the ratio of nicotinamide adenine dinucleotide (NAD+) to its reduced form (NADH). Early neuronal apoptosis in the retina is mediated by the AR pathway. (Asnaghi, Gerhardinger *et al.* 2003)

The advanced glycation endproduct (AGE) theory proposes that glycosylation and crosslinking of proteins by glucose may cause damage by disrupting multiple protein-mediated functions (Brownlee 1995; Giardino, Edelstein *et al.* 1994; Sharma, Pandey *et al.* 2002).

The protein kinase C (PKC) pathway describes the increased activation of members of the PKC family of intracellular signalling proteins in animals with diabetes (Ishii, Koya *et al.* 1998), to produce physical and enzymatic damage to cells (Sheetz and King 2002). The PKC pathway can be activated either by lipid second messengers, or by inappropriate activation through the ROS pathway.

Diabetes increases the activity of the hexosamine biosynthetic pathway, responsible for the processing of intermediate compounds in the metabolism of sugars. The key enzyme of this pathway is glutamine: fructose-6-phosphate amidotransferase (GFAT), the over activation of which has been shown to alter gene expression and increase extracellular matrix production (Kolm-Litty, Sauer *et al.* 1998).

The reactive oxygen species (ROS) theory draws from the fact that high glucose levels increase the production of free radicals(Nishikawa, Edelstein *et al.* 2000), which have been shown to damage cellular proteins (Hunt, Dean *et al.* 1988), and DNA (Suzuki, Hinokio *et al.* 1999), to alter the NAD+/NADH balance, and, by increasing oxidant stress, to induce a number of conditions found in diabetic complications, including endothelial dysfunction. Increased rates of apoptosis are also found associated with the oxidant stress induced by high glucose, and this may affect endothelial barrier function relevant to prelesion events in atherosclerosis (Russell, Golovoy *et al.* 2002).

ROS as a Unifying Mechanism

Brownlee et al. 2005 proposed (Brownlee 2005) that there is a unifying mechanism for the activation of the AR, AGE, PKC, and HK molecular pathways of cell dysfunction in diabetes. Intracellular high glucose leads to increased glycolysis and an oversupply of glycolytic endproducts to the mitochondria. Increased mitochondrial

metabolism causes a kinetic mismatch at the end of the electron transport chain. At normal metabolic rates—after passing through the mitochondrial membrane—the donated electrons mostly match up with hydrogen ions from which they came. At high metabolic rates, the dwell time for freed electrons is long enough that they can become an "extra" electron to local oxygen species, creating elevated levels of ROS, which can cause DNA nicking. DNA damage will activate the repair enzyme Poly(ADP-ribose) polymerase (PARP). Increased activity of PARP was found to be a precursor to each of the remaining 4 metabolic pathways. In addition, activation of PARP decreased the activity of the key glycolytic enzyme glyceraldehyde-3 phosphate dehydrogenase (GAPDH) by modifying the enzyme with the addition of ADP-ribose from NAD+ (Du, Matsumura *et al.* 2003).

PARP Mediated ATP Depletion

PARP by itself is known to be a strong inhibitor of the production of ATP by immobilizing NAD+. During the DNA repair process, activated PARP uses ADP-ribose from NAD+ to repair damaged DNA. PARP is quickly reactivated, on the order of seconds, while the recycling time for NAD+ is on the order of hours (Szabo 2004). As a result, the production of ATP is slowed. The higher the number of DNA nicks, the slower the ATP synthesis proceeds (Martin and Schwartz 1997). PARP induced GAPDH downregulation further lowers ATP by decreasing glycolysis. (Beauvieux, Couzigou *et al.* 2004) showed that a decrease in ATP production by glycolysis results in a sharp increase in the rate of ATP production by the mitochondria. Thus a positive feedback loop leading from mitochondrial hyperactivity, to PARP activation, to GAPDH downregulation, and further increase in mitochondrial oxidative phosphorylation, can

lead to severe ATP depletion (Kiss and Szabo 2005; Pacher and Szabo 2005; Sheline, Wang *et al.* 2003). It is important to note that the activation of PARP by radiation or chemotherapy, and subsequent ATP depletion, with adjuvant glycolytic inhibition, has long been accepted as a method to induce apoptosis or necrosis in cancer cells (Boulares, Yakovlev *et al.* 1999; Martin and Schwartz 1997; Zong, Ditsworth *et al.* 2004) (Pettitt, Clarke *et al.* 1999). Since cancer cells have an extremely high metabolic rate, and are already awash in reactive oxygen, the additional metabolic burden of induced PARP activation preferentially kills the cancer cells over normal cells. Tumor reduction by ATP depletion is a staple of cancer therapy (Martin, Bertino *et al.* 2000). The fact that ATP depletion in non diabetic cells also increases cell death and causes pathologies similar to those found in diabetes (Nerlich, Hagedorn *et al.* 1998; Weiderpass, Ye *et al.* 2002), provides ample motivation to determine the role that PARP-mediated ATP depletion plays in the mechanism of cell dysfunction in the diabetic environment. Consistent with our hypothesis that it is depressed ATP levels that lead to cell dysfunction is the striking observation of the reduced incidence of cancer in diabetes (Sussman, Carson *et al.* 1988).

Atherosclerosis is not the most dramatic example of diabetic complications, but it may be the most deadly. One in every 3 people has some form of cardiovascular disease CVD, and only about half are over 60 years of age. Although the link between diabetes and atherosclerosis (sometimes called “the burden of heart disease in diabetes”) is statistically known, it is poorly understood. Fortunately, recent advances in describing the development of atherosclerosis in terms of trans-endothelial transport of water and cholesterol, including those made by our group (Zeng, 2006, Yu 2008, Nguyen 2008),

and in quantifying endothelial barrier function (Sill, Tarbell, etc) have allowed us an avenue to further investigate the factors linking them.

The foundation of our hypothesis is that the action of PARP only indirectly influences the fate of the endothelium by regulating ATP depletion, either through ADP-ribosylation of GAPDH, or activation of the other pathways. This admits the possibility that the proximal cause of endothelial cell dysfunction is ATP depletion. The implication is then that if ATP levels can be restored independently of the action of PARP, normal endothelial function can be restored. To determine the feasibility of this strategy, it is necessary to quantify endothelial dysfunction in terms of ATP depletion, independently of the action of PARP. The goal of the research described in this thesis is to investigate this relationship, and to collect limiting or pseudo steady state data to identify the major steps to endothelial dysfunction in which either ATP alone or in conjunction with PARP, plays a role.

Background: Atherosclerosis and endothelial dysfunction

Pathogenesis of Atherosclerosis

Endothelial dysfunction is an important early event in diabetes (Endemann and Schiffrin 2004), principally characterized by hyperfiltration, angiogenesis, and increased rates of turnover. In hyperglycemic conditions endothelial protein expression is reduced (Tesfamariam 1994) and apoptosis is increased (Najemnik, Sinzinger *et al.* 1999). This fact forms the basis for the current investigation into the observed increase in incidence of atherosclerosis in people with diabetes. In vessels where diabetic complications manifest, the large arteries and retinal microvasculature, hyperglycemia induced changes

in hemodynamics, endothelial function, expression of vascular factors and activation of inflammatory cells are directly correlated to cell and tissue pathology.

The endothelium is the principal cellular structure in the blood-tissue barrier, and is hypothesized to be the principal site of cellular dysfunction in diabetic vascular complications. The cleft between endothelial cells is the major pathway for macromolecular transport by convection. It has been shown that intercellular clefts of more complex morphologies represent a greater barrier to transport (Gerrity, Richardson *et al.* 1977; Zimmerman and McGeachie 1986). These complex protein structures are termed tight junctions, and play a principal role in maintaining the integrity of the endothelial monolayer by restricting passage of large molecules and reducing the flow of water to the sub-endothelial region. The intercellular cleft without tight junctions has been shown to be highly permeable to horseradish peroxidase (HRP) (diameter ~ 5 nm) (Huang, A. L., Jan *et al.* 1992). However, breaks in tight junctions can provide a pathway for the transport of macromolecules. (Caplan, Gerrity *et al.* 1974; Okuda and Yamamoto 1983; Weinbaum, Ganatos *et al.* 1988). When cells are in mitosis their junctions also become leaky and allow for transport of larger particles (Ammann, Noel *et al.* 1990; Chuang, Cheng *et al.* 1990; Dennerll, Joshi *et al.* 1988; Stemerman, Morrel *et al.* 1986; Truskey, Roberts *et al.* 1992; Weinbaum, Ganatos *et al.* 1988). Although the total number of endothelial cells going through mitosis at any given time is extremely small, they account for 25% of all leakage sites. (Kast and Hauser 1992). In addition 63% of dead or dying cells co-localize with leaks large enough to admit albumin (diameter ~ 7nm), resulting in a contribution of 37% (Ammann, Noel *et al.* 1990).

Apoptotic or mitotic cells do not account for all leaks observed; normal healthy cells account for the remaining 38% of leaky sites (Truskey, Roberts *et al.* 1992).

Endothelial apoptosis rates, and cellular turnover rates, are of particular interest because they provide insight into the observed increase in endothelial macromolecular permeability associated with atherosclerosis. It has been shown that transmural convection accounts for much of the transport through leaky junctions, because the observed rapid initial growth of tracer spots through leaky junctions is too fast to be solely diffusion mediated. (Weinbaum, Ganatos *et al.* 1988).

Atherosclerosis, endothelial barrier function, and ATP

In diabetes, hyperpermeability of the endothelium, high rates of apoptosis of endothelial cells, and deterioration of the sealing response to increased microvascular pressure may be mediated by cytoskeletal failure (Endemann and Schiffrin 2004; Feigenbaum, Bergeron *et al.* 1994; Ho, Liu *et al.* 2000; Lee and Gotlieb 2003; Najemnik, Sinzinger *et al.* 1999). Cytoskeletal failure itself can be induced by ATP depletion (Carlier 1992; Unno, Menconi *et al.* 1996; Watanabe, Kuhne *et al.* 1991). The fact that tight junctions are connected to cytoskeletal fibers through intermediate membrane proteins, and that leaky junctions form around dead cells, or cells undergoing mitosis (Weinbaum, Ganatos *et al.* 1988), coupled to experimental evidence that both cytoskeletal integrity and barrier function are dependent on ATP concentration (Hart, Andreoli *et al.* 1993) suggests that ATP depletion affects permeability through disruption of the cytoskeleton. In cultured renal epithelium it has been shown that the mechanism of ATP disruption of tight junctions is through the actin cytoskeleton (Bacallao, Garfinkel *et al.* 1994; Golenhofen, Doctor *et al.* 1995). In the case of the endothelium, as noted,

permeability to macromolecules has been linked to apoptosis and subsequent cell turnover, but permeability to water has been linked to the integrity of cell-to-cell tight junctions. Both have been shown to increase in the case of ATP depletion (Holman and Maier 1990; Meyer, Schwesinger *et al.* 2001; Unno, Menconi *et al.* 1996).

Synthesis: Relationship between Diabetes, ATP, and Atherosclerosis

Our hypothesis is that the effect of the unifying mechanism proposed by Brownlee *et al.*is, in fact, to lower ATP levels in the cell by direct activation of PARP, the inhibition of GAPDH, and the depletion of NAD+, and that this ATP depletion induces the observed loss of junctional integrity and increase in apoptosis that lead to increases in vessel permeability and hydraulic conductivity characteristic of diabetic endothelial dysfunction. By quantifying the functional relationship between high glucose, PARP activation, ATP depletion, and cell dysfunction, we can predict the behavior of the endothelium for small changes in glucose.

Outline of Experimental Method

The clinically accepted low end of the range for hyperglycemia that will lead to complications is around 10mM, and hospitalization is recommended for levels above 20mM. *In vivo* experiments typically choose a higher value, 20 or 25mM. For this research, a series of graded glucose concentrations, from 5mM to 30mM was chosen to allow the development of a relational model of glucose to dysfunction, rather than the demonstration of endpoint pathology. The parameters of interest in our investigation were the concentrations of glucose, ROS, PARP activity, ATP levels, cell death, and endothelial permeability to water and macromolecules.

The control condition was the measurement of cell function in the series of graded glucose concentrations. Then we manipulated intracellular ATP concentrations—first by blocking the activity of PARP, and then by blocking the activity of the mitochondria—and compared cell function against control data. Our quantification of the glucose-PARP-ATP relationship proceeds in three parts. In the first, the response of the endothelium under experimental treatment was modelled as an intracellular protein diffusion-limited process of tight junction remodelling. This mathematical model of the sealing effect has allowed us to increase the number of measurable, physically meaningful, relevant parameters that one can extract from a typical data set and that quantify the health of the endothelium. Experimental validation of the sealing model makes up the third chapter of this report. Cells with a known experimentally induced dysfunction were tested and analyzed by the sealing model and the results compared against model predictions. In the fourth chapter, we investigate the relationship between PARP, ATP, and diabetic endothelial dysfunction. We use existing methods to establish the existence of functional dependencies. In this process we apply the sealing model to quantify barrier function. Quantitative measurement of barrier dysfunction the critical parameter used for of evaluation of the glucose-PARP-ATP system. Finally, we discuss future directions for this work.

Chapter 2. Protein Diffusion Model of the Sealing Effect

Chapter Abstract

Motivated by evidence that endothelial tight junctional sealing occurs by the diffusion of presynthesized protein from the interior of the cell to the cell border, we develop a mathematical model of the sealing effect as a diffusion limited closing of intercellular gaps. Water transport across the endothelium is believed primarily to occur through these breaks in the tight junction strand, located at the cell periphery, between neighboring cells. Additional proteins arriving at the tight junction close the breaks, which attenuates the water flux. A single endothelial cell is represented as a thin axi-symmetric disk, initially containing a uniform distribution of junctional protein that does not interact with the apical or basal surfaces of the cell. Upon the application of a transmural pressure gradient, water flows through the junctional cleft, and tight junction remodelling begins. We assume that proteins at the site of the remodeling are instantaneously incorporated into the junction strand, causing the local protein concentration to drop, and the diffusion of intracellular proteins toward the junction to begin. This yields a one-dimensional diffusion initial value problem in cylindrical coordinates with Dirichlet boundary conditions at the periphery, and bounded at the origin. The solution provides an excellent fit to current and previously published experimental data, and yields three physically meaningful parameters for each fit, including a protein diffusivity in the cytoplasm that varies little within experimental treatments. These results suggest that the sealing effect can be explained by protein

diffusion and is consistent with experimentally observed translocation of pre-existing intracellular protein to the cell-cell junction.

List of symbols used in this chapter	
Roman Symbols	
C	*concentration (mmol/mL)*
D	*diffusivity of protein (cm^2/s)*
f_O	*fraction of gap length in total tight junction length*
H	*Depth of intercellular junction (nm)*
h	*Height of endothelial glycocalyx (nm)*
J_0	*Bessel function of the first kind, order 0*
J_1	*Bessel function of the first kind, order 1*
Jp	*Protein flux ($mmol \cdot s^{-1}$)*
Jv	*Water flux ($cm^2 \cdot s^{-1}$)*
K_d	*Darcy permeability of the glycocalyx (nm^2)*
Lp	*Hydraulic conductivity ($cm \cdot s^{-1} \cdot cmH_2O^{-1}$*
L_{tj}	*length of tight junction per unit area (μm^{-1})*
P	*Hydrostatic Pressure ($dynes/cm^2$)*
R	*cell radius (μm)*
S_A	*Surface area (cm^2)*
w	*Width of intercellular cleft (nm)*
Greek symbols	
μ	*Fluid viscosity ($dynes \cdot s/cm^2$)*
σ	*Reflection coefficient*
π	*Osmotic pressure ($dynes/cm^2$)*
λ_n	*The nth zero of the Bessel function*
Subscripts and superscripts	
tj	*tight junction*
EGL	*Endothelial glycocalyx layer*
c	*Endothelial cleft*

Table 2.1) ***List of symbols used in this chapter***

Introduction: The sealing effect

The endothelium forms a selectively permeable barrier to the transport of water and nutrients from the blood to other tissues of the body (Mehta and Malik 2006; Tarbell 2003). One interesting characteristic of this monolayer of cells is that the permeability changes in response to environmental conditions. It has been observed that an increase in pressure across the endothelium will result in an increased volume flow rate, but that this increase will gradually attenuate (the "sealing effect") over a period of minutes to hours, even when the pressure remains constant (DeMaio, Tarbell *et al.* 2004; Turner 1992). The sealing effect, which has been observed *in vivo* and *in vivo*, is intimately connected to barrier function (Kim, Harris *et al.* 2005; Tedgui and Lever 1984).

The tight junction is the principal modulator of endothelial barrier function. It takes the form of a band of proteins which span the cleft between adjacent cells, forming an impermeable junctional strand along approximately 90% of the length of intercellular junctions (Adamson, Lenz *et al.* 2004) see Figure (2.1). It is primarily through the gaps in the junction strand that water flows. The permeability to water, or hydraulic conductivity (L_p), of the endothelium is the ratio of the rate of water transport to the effective pressure drop across the membrane,

(1)

$$L_p = \frac{J_V / S_A}{\left(\Delta P - \sigma \Delta \pi\right)}$$

where J_V is the volume flow rate (cm^3/s) and S_A is the area of the surface through which the water flows. ΔP is the hydrostatic pressure drop across the cell layer. $\Delta \pi$ is the osmotic pressure difference (Curry in (Renkin, Michel *et al.* 1984). The reflection coefficient, σ, which ranges from 0 to 1, accounts for the difference between the transport

through an ideal semipermeable membrane and that through real experimental cell layers, which in fact permit some solute to pass. In addition, the endothelial glycocalyx, a layer composed of long chains of proteoglycans, coats the luminal surface of the endothelium, contributing to the hydraulic resistance.

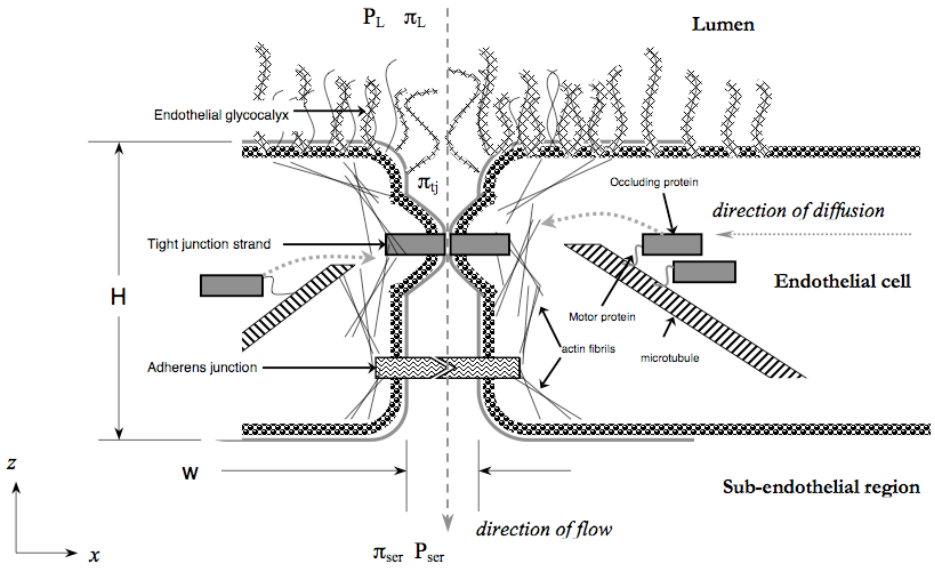

Figure 2.1) Schematic diagram of the inter-endothelial cleft in the *xz* plane. The flow of fluid is from lumen to sub-endothelial region, and is driven through the cleft by the pressure gradient. The tight junction (~3 nm wide) inhibits water flow. The adherens junction (~20 nm wide) maintains the intercellular spacing. Translocation of occluding proteins proceeds from the interior of the cell to the cell border. Adapted from (Tarbell 2003)

Two distinct protein complexes bind across the cleft between adjacent cells. The width of the cleft is kept at a fixed distance of (order 20 nm) by the adherens protein complex. But the tight junction complex, typically found closer to the luminal surface,

narrows the intracellular cleft to less than 3nm in width (Tarbell 2003). Tight junction proteins form a nearly continuous strand that increases hydraulic resistance—almost completely blocking the convective flow of water (Michel and Curry 1999). Breaks in the tight junction strand allow the cleft to open to the full width of the adherens junction, reducing hydraulic resistance and increasing the convection of water and solutes at that point. Hu *et al.* 1999 observed that breaks in the tight junction, with an average length of 150 nm, spaced approximately 4300 nm apart, were consistent with an analytical description of flow through the endothelial cleft in frog mesentery (Hu, Adamson *et al.* 2000), and later (Adamson, Lenz *et al.* 2004) found breaks of 315 nm at 3559 nm spacing in rat mesentery. In the case of an adaptive response to transmural pressure, it is the length of these breaks rather than the width of the cleft that is thought to decrease. It has been shown that, in response to a change in pressure, a translocation of the tight junction protein zonula occludens (ZO)-1 occurs, reducing flow across the endothelium (DeMaio, Tarbell *et al.* 2004). It is reasonable to assume that ZO-1 is taking part in the closing of tight junction breaks, and that the rate at which flow is attenuated may be proportional to the rate at which this protein is accumulating in the junctional interface. As more protein arrives, the length of the leaky portion of the junction becomes smaller, and the flow through the monolayer decreases (as shown in Figure (2.2)). As a first approximation, we assume that this protein transport can be modeled by the diffusion of protein from the interior of the cell to the cell border.

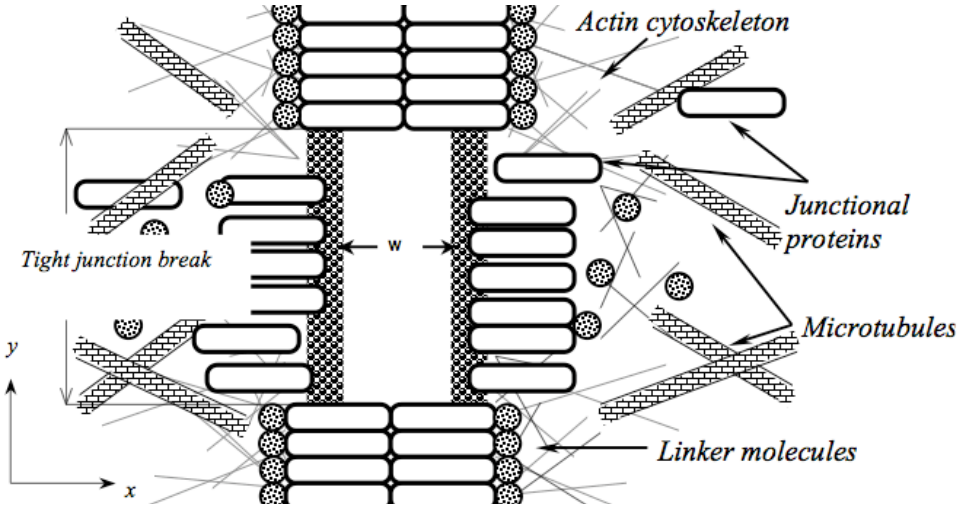

Figure 2.2) Top view of the endothelial cleft (*xy* plane), showing a schematic of the theoretical arrangement of proteins forming the tight junction. Tight junctional proteins are transported from the cytoplasm to the junction. When the junction is formed, these proteins span the width of the cleft between cells, reducing the width *w* from 20nm to less than 3 nm. The adherens junction (not visible) maintains a constant cleft width. As sealing progresses, the area available for flow changes as the length of the break is decreased, not the width.

An early model to characterize the trans-endothelial flow in terms of cell geometry is the slit-pore model, based on simple ideal Poiseuille flow through a slit. In this model the hydraulic conductivity is given by

(2)

$$L_p = \frac{L_{tj} w^3}{12 \mu H} f_O$$

where L_{tj} is the entire length of the intercellular cleft per unit area of the vessel wall, w is the width of the adherens junction, H is the height of the cleft from the base of the cell to the lumen, μ is the effective viscosity of water in the cleft, and f_O is the fraction of the

cleft that is open: the break length to total cleft length. The hydraulic permeability of the glycocalyx layer can be described by Darcy's law:

(3)

$$L_p = \frac{K_p}{h\mu}$$

where K_p is the Darcy permeability, h is the height of the glycocalyx, and μ is the fluid viscosity. Since flow in the *xy* plane is 2 orders of magnitude smaller than in the *z* direction (Hu and Weinbaum 1999), we make the simplifying assumption that there is no flow through the glycocalyx at points that do not correspond to an underlying break in the tight junction. This allows us to write equations (2) and (3) in terms of hydraulic resistance in series ($L_p^{-1} = L_{pc}^{-1} + L_{pEGL}^{-1}$), and with respect to a change in hydraulic conductivity with time ΔL_p, with the result

(4)

$$\Delta L_p = \frac{1}{\mu}\left(\frac{12H}{L_{tj}w^3} + \frac{h}{K_p}\right)^{-1} \Delta f_O .$$

For additional details about the difference between the ideal and experimentally observed flow through the complex geometry and hemodyamic environment of the intercellular cleft see (Sugihara-Seki and Fu 2005). Thus our model will retain the key element of equation (4), the slit-pore model, f_O, that relates hydraulic conductivity to the open fraction of the slit. For it is this open fraction, when considered in light of the proposed mechanism behind the sealing effect in (DeMaio *et al.* 2006), that allows us to propose our model. (DeMaio *et al.* 2006) showed that the diffusion of ZO-1 and other proteins to the cell border, and subsequent incorporation into the tight junction, is correlated to sealing. They were able to demonstrate that disruption of microtubules

within the cell's cytoplasm reduced the migration of protein to the tight junction. Further, they presented evidence that as sealing progresses, it is not the width of the cleft that changes, but rather the length and/or number of gaps in the junction strand.

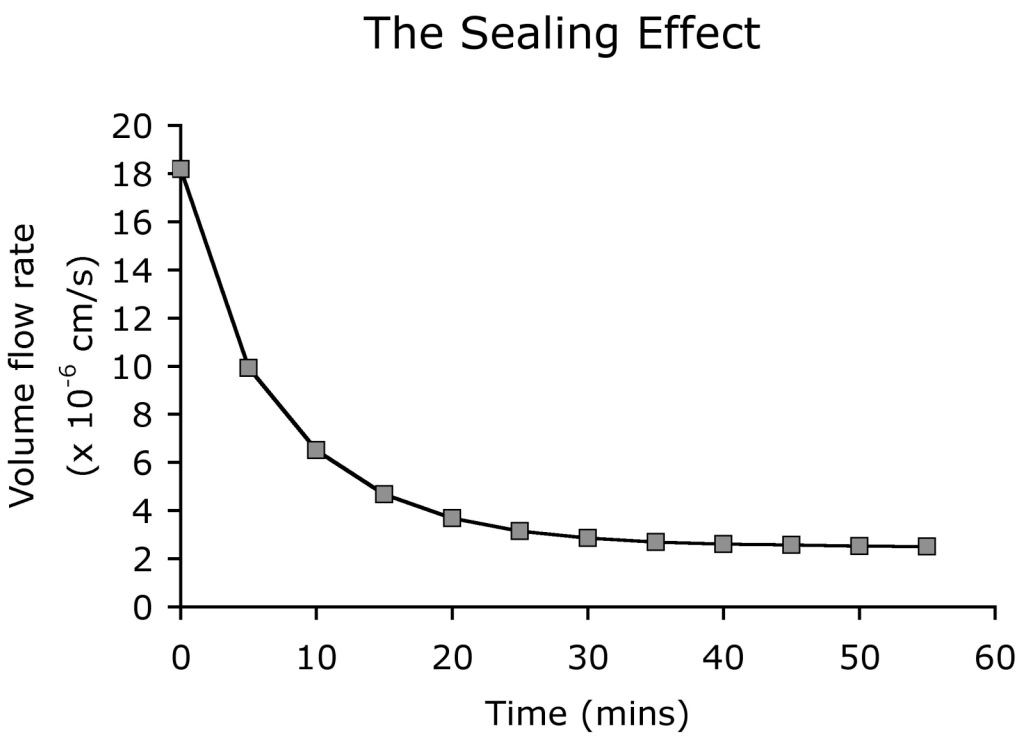

Figure 2.3) Typical volume flow rate vs. time curves for BAEC. Confluent monolayers grown on fibronectin coated polyester filters with 0.4μm pores are placed in a pressure-flow apparatus, and subjected to a 10cmH_2O transmural pressure. A significant attenuation of volume flow rate is seen over a period of 20 to 60 minutes.

The aim of the present model is to quantify the dynamic reorganization of the tight junction, and its attendant effect upon transmural flow. The stoichiometry and kinetics of each step of the dynamical system describing junction formation are largely unknown, although there is general agreement on the basic organization of the structure (see Figure (1). An attempt to develop a fully descriptive model would be inappropriate for the type

of data that is available, i.e. water flux as a function of time. Since the time scale of protein binding to the junction is very short relative to that of diffusion, we consider the kinetics of junction formation to be instantaneous compared to the speed of protein translocation. Similarly, the time scale of a change in the number of microtubules or actin fibers is slow relative to that of protein transport, allowing us to assume that cytoskeletal density is constant over the time course of an experiment.

Experimental considerations

Before beginning a description of the model, it is important to consider the experimental constraints on the pressure-flow experiment that define the sealing effect. The first experiments to determine the hydraulic conductivity of the endothelium were those carried out by (Landis 1927) on microvessels, and later improved upon by (Smaje, Zweifach *et al.* 1970), (Zweifach 1971), and (Michel, Mason *et al.* 1974), in which the relative movement of red blood cells in occluded vessels was tracked to measure outflow. Although the concept is simple, the complexity of the system required mathematical modeling to take into account capillary distensibility and other storage and resistive effects in order to extract meaningful parameters from the data. Developments in cell culture models for the same purpose by (Baetscher and Brune 1983), (Tarbell, Lever *et al.* 1988), (Suttorp, Hessz *et al.* 1988), (Turner 1992) and (Dull, Jo *et al.* 1991), introduced a flow marker (air bubble) in a separate impermeable chamber (a calibrated capillary tube) in-stream with the experimental cell preparation, that ensured that marker movement was a result only of volume flow across the monolayer. Further improvements added automated bubble-tracking components and computerized data acquisition as published in (Sill, Chang *et al.* 1995), where a more comprehensive

description of our complete apparatus and method may be found. Nguyen (2008 thesis) also employed this system to measure L_p in whole vessel explants. The most recent improvements from (Hubert, McJames *et al.* 2006) involve the incorporation of a live video camera to record bubble position, and the integration of a proprietary-platform-based data processing algorithm to reduce errors in data acquisition and processing.

Our system is based upon that of (Sill *et al.* 1995) and is shown in Figure (2.4). Briefly, endothelial monolayers are cultured to confluence on porous polycarbonate filters, and placed in a fluid filled chamber with an upper and lower compartment. The lower compartment is connected to a glass capillary tube with an air bubble in it. When pressure is applied to the fluid in the upper compartment, water flows through the monolayer, into the lower compartment, pushing the bubble along the tube. The entire apparatus is maintained in at 37°C, 5% CO_2. Bubble position is recorded for 20 minutes before, and then for 60 minutes after the application of pressure.

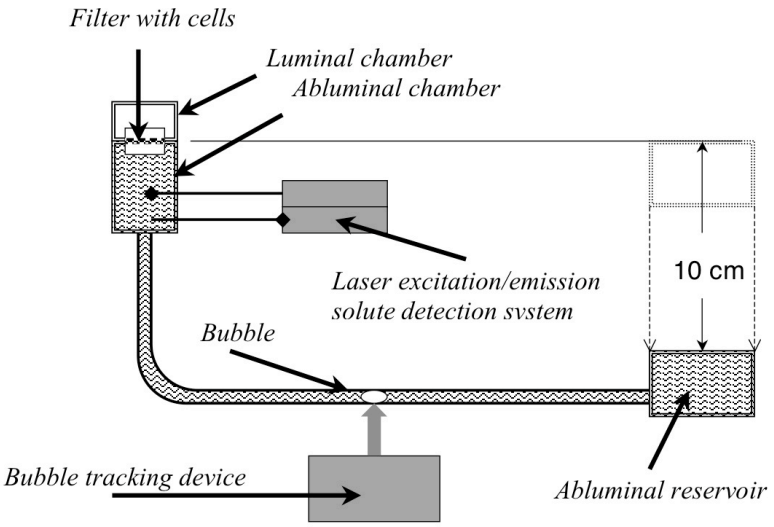

Figure 2.4) Schematic diagram of the pressure-flow apparatus. Bovine aortic endothelial cell (BAEC) monolayers are cultured to confluence on porous polycarbonate filters, and placed in a fluid filled chamber with an upper and lower compartment. The lower compartment is connected to a glass capillary tube with an air bubble in it. When pressure is applied to the fluid in the upper compartment, water flows through the monolayer, into the lower compartment, pushing the bubble along the tube. Bubble movement is detected by a photometer and recorded by an electronic data collection system. The entire apparatus is maintained in at 37°C, 5% CO_2. A fluorescent detection system allows measurement of fluorescent-conjugated solutes. Fluorescence accumulation in the basolateral chamber is measured by recording the emission of the label after excitation by a laser beam.

The experimental data collected is the position of the bubble as a function of time, as shown in Figure (2.5). Typically, bubble displacement is converted to volume flow rate per unit area, J_V, by the following equation:

(5)

$$J_V = \frac{\Delta x}{\Delta t} F$$

where Δx is bubble displacement Δt is the time interval and F is the ratio of the area of the bubble tracker tube to the cross sectional area of the monolayer.

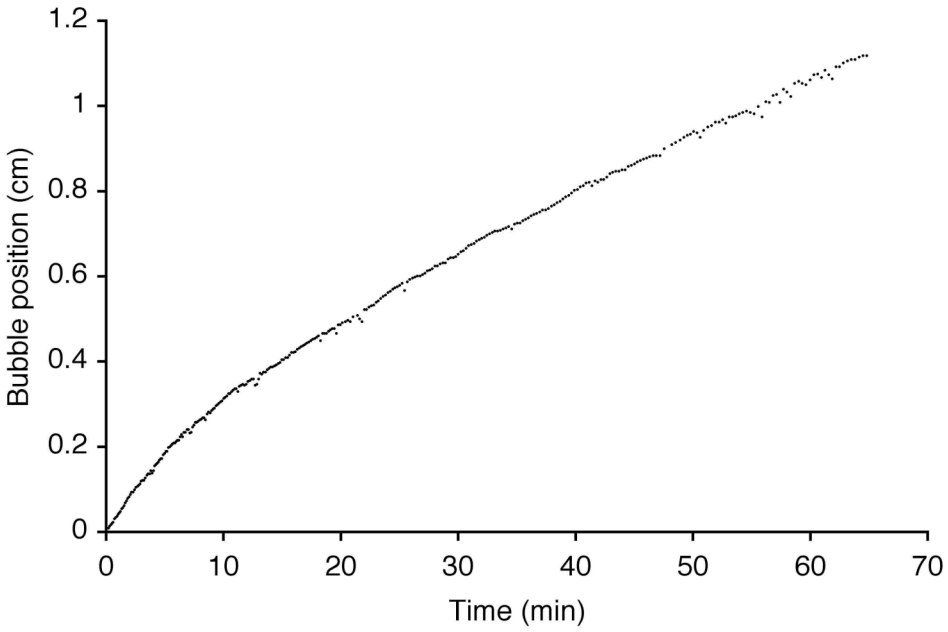

Figure 2.5) Raw data showing bubble position vs. time. Typical raw data for BAEC monolayers, from which the curve in Figure (2.3) is extracted. As the experiment progresses, the sealing effect causes the bubble to move more slowly. After 30 to 60 minutes, sealing is effectively complete.

Ideally, the movement of the bubble will be continuous and smooth, and the position data will be monotonically increasing. However, slight changes in ambient

temperature, environmental vibrations, noise in the trans-endothelial flow, rupture of the lubricating liquid film surrounding the bubble leading to a three-phase contact line on the tube wall—a strong opposing force to bubble movement and one that is more likely at very slow bubble velocities—can all have a small effect on the progress of the bubble, resulting in noisy data. In addition, as the flow attenuates, the movement of the bubble slows, causing the signal to noise ratio to decrease. The numerical approximation of the volume flow rate from noisy marker position data is the largest source of error. Therefore a secondary goal of our transport model is to avoid amplification of error. To address this, we model volume flow from first principles, and then integrate the model to obtain position-time predictions which we can compare directly to raw data without numerical differentiation.

Model description and equations

The primary contribution of our transport model is to mechanistically explain the entire experimental data curve, and to extract the relevant physical parameters. In current methods of studying convective transport in cell culture, only the steady-state volume flow rate ($J_{V\infty}$) is extracted from the data at the end of the curve. The improvement offered by our analysis is the extraction of two additional parameters from early data that, as we shall see, provide valuable information related to monolayer integrity and experimental preparation. These parameters allow the development of predictive hypotheses based on measurable cell properties, and providing additional criteria for the comparison of different cell culture treatments.

Figure (2.6) shows the schematic diagram of the model of a cell in a two-dimensional periodic array. By abuse of geometry (since circles do not tile the plane) we

describe the endothelial cell as an axisymmetric thin disc adjoining neighboring cells along its perimeter. Although endothelial cells *in vivo* often have an elongated shape, aligned with the direction of flow, *in vivo* the cells are close packed in a characteristic cobblestone pattern, approximately hexagonal, and with an aspect ratio (out of plane height, to in plane radius) ranging from 1:15 to 1:30.

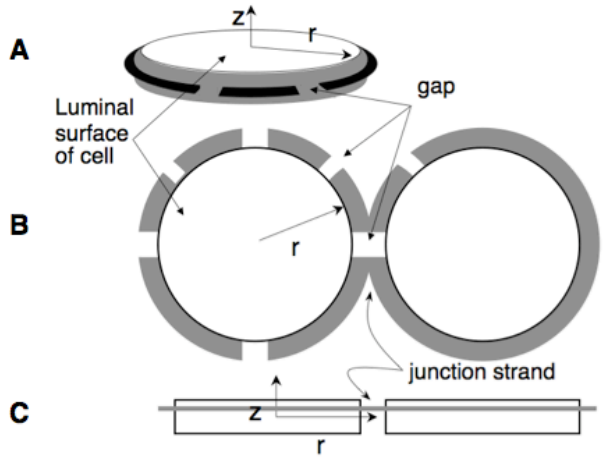

Figure 2.6) Idealized cell and junction geometry showing A, an oblique projection, B an *en face* view, and C, a lateral view. The break in the junction strand between cells is presumed to be the pathway for water flow and solute transport. The tight junction is modeled as a single strand of unit height (*z* direction). Diffusion of protein from the interior of the cell in the *r* direction, to the cell border, allows for the remodeling of the tight junction, and the attenuation of flow.

We do not attempt to resolve the issue of close-packing; gaps at the 3 cell contact point are not considered. Since the tight junction forms only at the periphery of the cell, the occluding proteins have no interaction with the apical and basal surfaces of the cell.

Although the cell has finite thickness, we assume the junction strand is composed of a single band of protein molecules, and the rate of junction formation to be independent of position in the z direction. The problem then reduces to an initial value problem of the diffusion equation in a thin disc, of unit thickness, with insulated top and bottom surfaces.

The equation in axisymmetric coordinates that describes the diffusion of intracellular protein to the tight junction is

(6)

$$\frac{\partial C}{\partial t} = D\left(\frac{\partial^2 C}{\partial r^2} + \frac{1}{r}\frac{\partial C}{\partial r}\right)$$

where C is the concentration of free protein in the cell, and D is the diffusivity of the protein in the cytoplasm. The composition of the tight junction requires the assembly of multiple proteins. ZO-1 has been shown to be necessary for tight junction assembly, and to move from a diffuse cytoplasmic distribution to a concentrated band at the periphery (Anderson, Van Itallie *et al.* 1989). We model the diffusion of a single protein species, such as ZO-1, rather than attempting to track the concentrations of several species. This is equivalent to assuming that the diffusion of ZO-1 or another single species is rate limiting, or that we are approximating the migration of several species into the tight junction by that of an average species. The free protein is assumed to be instantaneously and irreversibly bound into the junctional complex as it arrives at the cell border, $r = R$. Since we assume that the rate of incorporation of free protein into the junction is very fast relative to the rate of free protein diffusion, its concentration is always zero at the outer radius of the cell (diffusion-limited problem). The boundary and initial conditions for

equation (6) are that the concentration is bounded at the origin, with a homogenous Dirlichet condition at the junction, and that initially the occluding protein is dispersed uniformly throughout the cell at a concentration C_0.

(7)

$$C(r=R,t)=0 \qquad |C(r=0,t)|<\infty \qquad C(r,0)=C_0$$

In equation (7), *R*, the cell radius, is known, and C_0, the initial concentration of protein in the cell that is available to build new tight junction, is in general unknown.

We nondimensionalize the variables as follows:

(8)

$$\overline{C}=\frac{C}{C_0} \qquad \overline{R}=\frac{r}{R} \qquad \bar{t}=\frac{t\cdot D}{R^2}$$

yielding

(9)

$$\frac{\partial \overline{C}}{\partial \bar{t}}=\frac{\partial^2 \overline{C}}{\partial \overline{r}^2}+\frac{1}{\overline{r}}\frac{\partial \overline{C}}{\partial \overline{r}}$$

with boundary and initial conditions

(10)

$$\overline{C}(\bar{r}=1,\bar{t})=0 \qquad \overline{C}(\bar{r}=0,\bar{t})<\infty \qquad \overline{C}(\bar{r},0)=1$$

The flux of free protein into the tight junction, J_P, is given by

(11)

$$J_P=-D\left.\frac{\partial C}{\partial r}\right|_{r=R}, \quad or \quad \bar{J}_P=\frac{R}{DC_0}J_P=-\left.\frac{\partial \overline{C}}{\partial \overline{r}}\right|_{\bar{r}=1}.$$

Let $A(\bar{t})$ be the amount of protein entering the junction from time 0 to t. The integration of this flux with respect to time is the total amount of new protein arriving at

and being incorporated into the tight junction per unit area of junction, over the time of the integration. Equation (12) relates $A(\bar{t})$ to the dimensionless form of this integral, with appropriate conversion from concentration to mass:

(12)

$$\beta(\bar{t}) \equiv \frac{A(\bar{t})}{A_\infty} = \frac{A(\bar{t})}{\pi R^2 C_0} = -2\int_0^{\bar{t}} \left.\frac{\partial \overline{C}(\bar{r},\bar{t}')}{\partial \bar{r}}\right|_{\bar{r}=1} d\bar{t}'$$

In equation (12) $A_\infty = \pi R^2 C_0$ is the total amount of *intracellular* protein available for sealing at the beginning of the experiment, and $\beta(\bar{t})$ is the ratio $A(\bar{t})/A_\infty$, the fraction of sealing protein incorporated into the junction between the beginning of the experiment and time $\bar{t}$. The sealing effect occurs as this ratio goes from 0 to 1. It is important to realize that $\beta(\bar{t})$ is a universal function that contains no parameters. As such one can calculate it once and for all.

In addition, we allow that some portion of the junction is already sealed at $t = 0$. This amount of protein, defined as B_0, depends on the ability of the quiescent monolayer to form tight junctions without transmural flow, and is unknown. Therefore, the sealing effect starts with an amount B_0 in the junction, and ends when the total amount of protein in the junction is $B_0 + A_\infty$. The total fraction of sealable junction per cell as a function of time is then

(13)

$$f_S(\bar{t}) = \left(\frac{B_0 + A(\bar{t})}{B_0 + A_\infty}\right)$$

and the unsealed fraction is

(14)

$$f_O(\bar{t}) = \left(\frac{A_\infty - A(\bar{t})}{B_0 + A_\infty}\right) = \frac{A_\infty}{B_0 + A_\infty}\left(1 - \beta(\bar{t})\right)$$

The experimental raw data is bubble position, *x,* vs. time, *t*. After the application of pressure, the bubble begins to move, and the bubble tracker picks up the moving bubble at position x_0 at time t_0. $J_V(\bar{t})$ is the volume flow rate of water through the monolayer at time $\bar{t}$ and we have by analogy with equation (5),

(15)

$$x(t) - x_0 = \frac{1}{F}\int_{t_0}^{t} J_V(\bar{t})\, d\bar{t}$$

J_V, the total flow rate, has a contribution $J_{v\infty}$ that persists at infinite time due to junctions that do not seal. It is this value that has heretofore been extracted from convective transport experiments and reported. The balance, $J_V - J_{v\infty}$, seals by protein accumulation in the cell junction. To relate the build-up of protein to the flow of water through the junction, we return to the basic model of flow through a slit from equation (4), and, substituting J_V for L_P :

(16)

$$J_V(t) - J_{V\infty} = \alpha\ f_O(t)$$

Where α is

(17)

$$\alpha = \left(\frac{\Delta P - \sigma\Delta\pi}{\mu}\right)\left(\frac{12H}{L_{tj}w^3} + \frac{h}{K_p}\right)^{-1},$$

a constant derived from the geometry of the cleft, the transmural pressure—assumed to be constant over the course of the experiment, the effective viscosity of the fluid, and correction factors for the glycocalyx as determined by previous studies (Adamson and Michel 1993) and detailed in the next section in Table (2.2). It follows that

(18)

$$x(t) - x_0 = \frac{1}{F}\int_0^t \left(\alpha\ f_O(t) + J_{V\infty}\ \right)dt$$

In order to use our non-dimensional expression for the unsealed fraction we have to nondimensionalize equation (18) where $\bar{x} = x/R$, $\bar{J}_V = J_V R/D$, and $\bar{\alpha} = \alpha\ R/D$, then,

(19)

$$\bar{x}(t) - \bar{x}_0 = \frac{1}{F}\left[\bar{\alpha}\left(\frac{A_\infty}{B_0 + A_\infty}\right)\left(\bar{t} - \int_0^{\bar{t}} \beta(\bar{t}')\ d\bar{t}'\right) + \bar{J}_{V\infty}\bar{t}\ \right]$$

Reduction of parameters

To reduce the number of parameters, we take advantage of the fact that the total amount of sealing protein is

(20)

$$A_T = B_0 + A_\infty$$

Let $\gamma = B_0/A_\infty$ be defined as the ratio of the amount of available sealing protein in the junction to that inside the cell at t = 0. γ^{-1} is an important measure of the sealing effect. If $\gamma^{-1} >> 1$, then the sealing effect will be dramatic; if $\gamma^{-1} << 1$, then the sealing effect will be small. The quantity

(21)

$$\frac{1}{1+\gamma}$$

is the dynamic sealing length per unit length of sealed junction strand, a measure of how much sealing is accomplished during the course of an experiment. We call this the sealing potential.

One can express the total fraction of sealed junction per cell in terms of $\beta(\bar{t})$ and γ, from equation (14)

(22)

$$f_O(\bar{t}) = \left(\frac{1-\beta(\bar{t})}{1+\gamma} \right)$$

which allows us to rewrite equation (19) as

(23)

$$\bar{x}(t) - \bar{x}_0 = \frac{1}{F}\left[\frac{\bar{\alpha}}{1+\gamma} \left(\bar{t} - \int_0^{\bar{t}} \beta(\bar{t}')\, d\bar{t}' \right) + \bar{J}_{V\infty}\bar{t} \right]$$

Model parameters

Table (2.2) lists known physical and experimental parameters that were used to calculate α. The transmural pressure is the same for all experiments except where noted. With these numbers, our transport model predicts an unconstrained flow (as if none of the junction is sealed, i.e. for $f_O = 1$) of 22.0×10^{-6}cm/s. Given the typical value for the percent sealed gap *in vivo* of approximately 90%, that corresponds to a $J_{V\infty}$ of 2.2×10^{-6}cm/s, which is about half that of experimental observations. We observed poor agreement of theory with experimental results for values of w less than 25nm. As such, we used w = 25 nm to develop all solution fits. This best fit parameter gives a range of flow from 54.0×10^{-6}cm/s to 5.4×10^{-6}cm/s, which is in close agreement with experiment.

	Parameter	Source	Value
R	*Cell radius*	*BAEC in vivo (data not shown)*	15 μm
ΔP	*Transmural pressure*	*Known from experiment*	9.80 × 10-3 dynes/cm2 (10 cm H_20)
Ltj	*Length of tight junction per unit area*	*Calculated from model*	2/R
K_d	*Darcy permeability of the glycocalyx*	*(Sugihara-Seki 2005)*	6.10 nm^2
H	*Depth of tight junction*	*(Adamson, Lenz et al. 2004)*	411 nm
h	*Thickness of glycocalyx*	*(Zhang, Adamson et al. 2006)*	150 nm
w	*Width of adherens junction*	*(Adamson, Lenz et al. 2004) for rat mesentery*	18 nm
w^*	*Width of adherens junction*	*Predicted by curve fitting of the model*	25 nm
w_c	*Width of tight junction*	*(Tarbell, 2003)*	3 nm
μ	*Viscosity of water at 37°C*	*(Massey)*	7.544 × 10-3 dynes·s/cm2

Table 2.2) Structural parameters of the intercellular junction from literature and experiment.

Time dependent changes in pressure due to osmotic forces opposing filtration

Although our assumption is that the pressure differential is constant over the time course of the experiment, it has been shown that this is not strictly true. The Michel-Weinbaum model of a revised Starling principle (Hu and Weinbaum 1999) predicts that the development of a large difference in protein (albumin) concentration between the lumen and the sub-glycocalyx region could cause a significant osmotic force opposing the transmural flow, and this difference in the permeability of the glycocalyx to water and solutes will result in a time-dependent change in osmotic pressure. Taking into account the Michel-Weinbaum model, $\Delta\pi$ in equation (17) should then become time-dependent. Although the development of the protein gradient is time dependent, a simple order-of-

magnitude analysis (see appendix) shows that the time scale of the development of opposing osmotic forces is on the order of 5 to 50 seconds, very short relative to the time scale of the sealing effect, which is on the order of 20 minutes. This result was independently verified by experimental results (Levick and McDonald 1994) which showed that these same osmotic forces reach steady state in intact mesentery within 2 minutes.

Solution of the model equations

The solutions to equations (9), (12), and (19) in terms of Bessel functions of the first kind are presented here. See Appendix for the details of this solution. The solution to equation (9) is

(24)

$$\overline{C}\left(\bar{r},\bar{t}\right)=\sum_{n=1}^{\infty}\frac{2}{\lambda_n}e^{-\lambda_n{}^2\bar{t}}\,\frac{J_0\left(\lambda_n\bar{r}\right)}{J_1\left(\lambda_n\right)}$$

where λ_n is the nth eigenvalue of the Bessel function J_0, such that

(25)

$$J_0\left(\lambda_n\right)=0$$

The solution of β(t) in equation (12), the integral of the spatial derivative at the cell border, is then

(26)

$$\beta\left(\bar{t}\right)=\sum_{n=1}^{\infty}\frac{4}{\lambda_n^2}\left(1-e^{-\lambda_n{}^2\,\bar{t}}\right)$$

The integral of equation (26) is

(27)

$$\int_0^{\bar{t}} \beta(\bar{t}')\, d\bar{t}' = \sum_{n=1}^{\infty} \frac{4}{\lambda_n^4} \left\{ \lambda_n^2\, \bar{t} \; - \; \left(1 \; - \; e^{-\lambda_n^2\, \bar{t}} \right) \right\},$$

allowing the solution of equation (19):

(28)

$$\bar{x}(t) - \bar{x}_0 = \frac{1}{F} \left[\frac{\bar{\alpha}}{1+\gamma} \left(\bar{t} - \sum_{n=1}^{\infty} \frac{4}{\lambda_n^4} \left\{ \lambda_n^2\, \bar{t} \; - \; \left(1 \; - \; e^{-\lambda_n^2\, \bar{t}} \right) \right\} \right) + \bar{J}_{V\infty} \bar{t} \; \right].$$

Finally in dimensional form for data fitting; and, assuming $\bar{x}_0 = 0$,

(29)

$$x\,(t) = \frac{1}{F} \left[\left\{ \frac{\alpha}{1+\gamma} + J_{V\infty} \right\} \, t - \frac{\alpha}{1+\gamma} \sum_{n=1}^{\infty} \frac{4}{\lambda_n^4} \left\{ \lambda_n^2\, t \; - \; \frac{R^2}{D} \left(1 \; - \; e^{-\lambda_n^2\, t\, D/R^2} \right) \right\} \right].$$

Algorithm development

The model was implemented using MATLAB®. The built-in function *fmincon,* a steepest-descent approach to the optimization of a constrained nonlinear multivariable function, was applied. The quantity to be minimized was the weighted residual sum of squares of position data vs. model prediction. The fitting parameters were D, γ, and $J_{V\infty}$. A full description of *fmincon* is found in Constrained Optimization in Standard Algorithms of the MATLAB® Optimization Toolbox technical reference (© 1984-2008-The MathWorks, Inc.). The first 100 zeros of the Bessel function of the first type were determined using Halley's method (von Winckel 2005).

Validation of the model

Data Fitting

Figure (2.7) shows an example of a model curve (smooth line) overlaid upon typical experimental data (points). The data curve shows a uniform noise signal throughout. Note the close agreement between model curves and data: the curvature of the early portion of the data is determined by optimization of diffusivity and sealing potential, the linear slope at the end of the data is determined by optimizing $J_{V\infty}$. Standard error is on the order of 10^{-6} on dependent variable of order 10^{-1}.

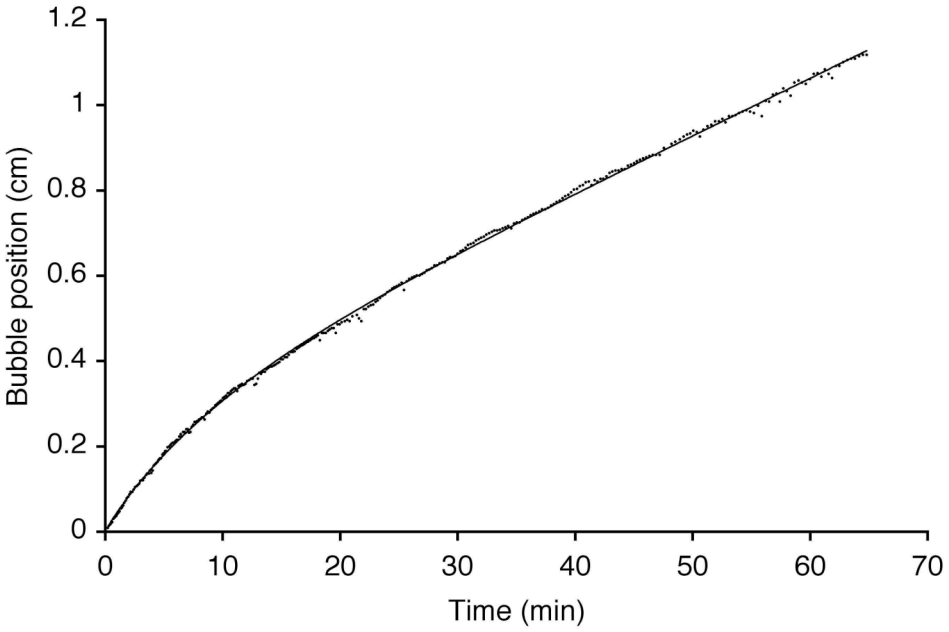

Figure 2.7) Raw data of bubble position vs. time with fitted curve overlaid upon it. Sum of squares error is on the order of 10^{-6} cm^2.

Data conditioning

A precise determination of the bubble position at the point of application of pressure is required for an optimum model fit. However, this point is often not known to sufficient precision, due to experimental uncertainty in the length of time to bubble recapture: there is a time lag between the true point of the application of pressure, and the point at which accurate data regarding bubble position can be obtained. The difficulty in tracking the bubble position at early time points where flow is high, is a condition of the experimental apparatus, has been noted before, and has led to the development of improved bubble-tracking methods (Hubert, McJames *et al.* 2006). The presence of early noise may result in an erroneous calculation of diffusivity, even when $t = 0$ and $x(t = 0)$ are known exactly. To avoid the error associated with this uncertainty, two data conditioning parameters were added to be determined by least squares fitting: the optimum starting point, x_0 and t_0. The optimum starting point should be the first point from which the bubble position best reflects the biological progress of the sealing effect, and not apparatus artifact.

To identify the point at which early noise disappears, the residual sum of squares of the curve-fitting program was calculated for a series of starting points before and after the known experimental time of pressure application, and plotted as a function of the starting point, as shown in Figure (2.8) A (open circles). The optimum point for t = 0 was determined to be the first point after the early noise, by noting a step drop in the SSE. A

numerical step function (Figure (2.8) line) was fitted to error data to find the drop point. The drop in SSE was also coincident with a stabilization of diffusivity as shown in Figure (2.8) B (open circles). Note that both curves are quite flat in a non-trivial region beyond the step. This indicates that the value of D is not sensitive to small errors in locating x_0 and t_0 just after the step drop. See appendix for details.

Comparison with numerical method

In addition to the analytical solution, a numerical method was devised based upon a finite difference scheme. The solution to equation (9) was approximated by a Runge-Kutta method with a mesh size of 100 points in r, and 1000 in t. The integration of equations (12) and (19) was approximated by Simpson's method. As expected, results were identical to the analytical solution to 4 significant figures. The sum of squares error (SSE), was identical to four significant figures as well. Computation of the function $\beta(\bar{t})$ was approximately 10 times longer than the analytical method.

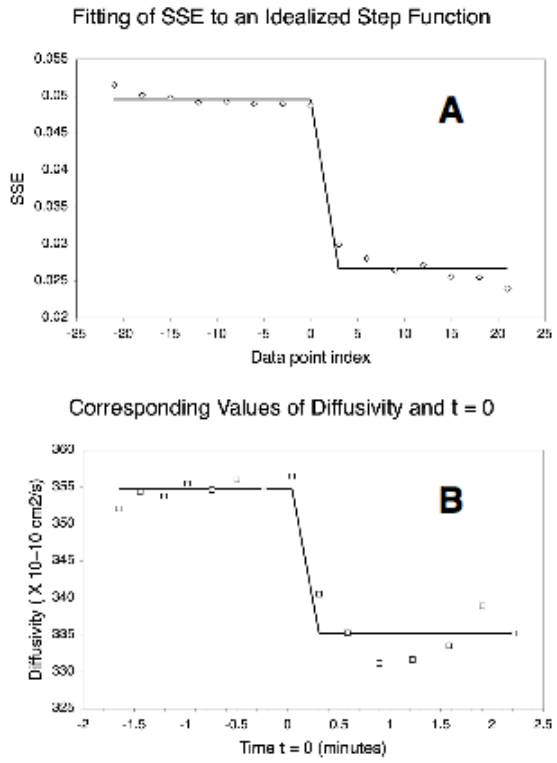

Figure 2.8) Optimization of *t = 0* for comparison against the model curve. A) Residual sum of squares (RSS) (open points) drops sharply after the early high noise region of data acquisition. Fitting data to a numerical step function (line) locates the first data point beyond the noisy region. B) For the data index adjustment calculated in A, the corresponding diffusivity and time adjustment to t = 0 are plotted. The drop in diffusivity is always strongly correlated to the drop in SSE.

Results and discussion

Fitted parameters for 7 experiments are shown in Table (2.3). Bovine aortic endothelial cells (BAEC) plated on fibronectin coated polycarbonate filters and tested as described above.

Sample number	*Diffusivity* ($\times 10^{-8}$ $cm^2 \cdot s^{-1}$)	Jv_∞ ($\times 10^{-6}$ $cm \cdot s^{-11}$)	*Sealing potential* $(1 + \gamma)^{-1}$
1	.4195[a]	8.519[b]	0.1050
2	.5089[a]	2.851	0.2597
3	2.261	3.674	0.2139
4	2.984[a]	5.518[b]	0.1534
5	2.521	6.084[b]	0.1412
6	2.498	6.080[b]	0.1413
7	2.240	1.380	0.4202
Mean	1.855	5.141	0.2049
Std dev	0.9956	1.888	0.1001
95% confidence interval	± 0.6901	± 1.308	± 0.06938

[a] *Outliers greater or less than 1.5 times the interquartile range in diffusivity.*
[b] *Outliers with Lp less than* 5×10^{-7} $cm \cdot s^{-1}$.

Table 2.3) Fitted parameters for 7 experiments. BAEC cultured to confluence plus one day on polycarbonate filters and subjected to transmural flow in the pressure flow apparatus described in (Sill *et al.* 1995).

Comparison to previous results

Since this is the first model to describe sealing from first principles, we compare our model to the steady state volume flow rate from previous results. Table (2.4) presents a comparison of experimental hydraulic conductivity to previously published work.

Current work	*Cell type*	*Lp*
Theoretical prediction (10% tight junction break)		5.4×10^{-7} *cm/s*
Experiment (average for normal cells)	BAEC	5.3×10^{-7} *cm/s*
Previous work		
(Cancel, Fitting et al. 2007)	BAEC	5.4×10^{-7} *cm/s*
(DeMaio, Tarbell et al. 2004)	BAEC	8×10^{-7} *cm/s*
(Dull, Jo et al. 1991)	BAEC	5×10^{-7} *cm/s*
(Turner 1992)	BAEC	36.7×10^{-7} *cm/s*

Table 2.4) Comparison of fitted values of *Lp* to previous studies of BAEC *in vivo* transport. Model predictions of *Lp* compared to experimental values and *Lp* from published sources. Where experimental results were reported as $J_{V\infty}$, values were converted to *Lp* by equation (1)

Our results are also in general agreement with diffusion velocities found by experiment. Movement of protein in the cell is reported in a variety of ways, diffusivity, speed of translocation, and speed of elongation. To compare our results for diffusivity to published results for various types of protein in the cell, we converted reported measurements to diffusivity. Table (2.5) shows the range of values from free diffusion, on the order of 10^{-7}cm/s, to diffusion of membrane bound proteins, on the order of 10^{10}cm/s.

Current Predictions	*Diffusivity*
Model results	*2.50×10^{-8} cm^2/s*
Free diffusion in media	
(Zhang 2006)	*9.29×10^{-7} cm^2/s (albumin in lumen)*
Speed of microtubule elongation	
(Walker 1991)	*6.25×10^{-7} cm^2/s (microtubules in vivo)*
Speed of cell migration	
(Pickering 1997)	*$13.5 \pm 3.6 \times 10^{-8}$ cm/sec (fibroblast)*
(Yao 2007)	*6.9×10^{-8} cm/sec (BAEC)*
(Osborne 2005)	*$3.75 \pm 1.6 \times 10^{-8}$ cm^2/s (BAEC under shear)*
Free diffusion in the cytoplasm	
(McGrath et al.1998)	*$5.8 \pm 1.2 \times 10^{-8}$ cm^2/s (actin)*
(Waharte, Brown et al. 2005)	*15×10^{-8} cm^2/s (actin)*
(Waharte, Brown et al. 2005)	*4×10^{-8} cm^2/s (myosin-1)*
Diffusion by motor protein transport	
(Kalchishkova and Bohm 2008)	*1.94×10^{-9} cm^2/s (no load)*
(Shtridelman, Cahyuti et al. 2008)	*1.67×10^{-9} cm^2/s (under load)*
Free diffusion in the plasma membrane	
(Wang et al.1999)	*2.16×10^{-10} cm^2/s*

Table 2.5) Comparison of fitted values of diffusivity against diffusivity of various protein systems in the cell. Speed of cell migration is presumed to be proportional to actin cytoskeletal elongation. Where published results are reported as velocity (cell migration, motor protein transport), or rate of elongation (microtubules), they have been converted to diffusivity according to the relationship $\langle x^2 \rangle / t = 4*D$, where $\langle x^2 \rangle$ is the mean square displacement (distance), t is time, D is diffusivity, and 4 is a constant of proportionality for 2-dimensional diffusion.

The assumption of the model is that sealing is a result of diffusion of sealing protein. Therefore, the diffusivity found by fitting the data should be the same for all cells of similar type and culture conditions. We show that diffusivity has a low standard error within cell treatments, and between experimental runs. It is not easy to tell by eye whether two curves have a similar shape when they vary in amplitude and time scale. The diffusion model gives two additional parameters which can be used in conjunction with $J_{V\infty}$. Table (2.5) shows that the diffusivity extracted by our model is in the middle of the physiologically relevant range, about the same speed as free diffusion of actin in the cytoplasm, or of the elongation rate of actin filaments.

The two problems that plagues this type of experiment are that of heteroscedacity (variability in data does not always decrease with increasing number of observations), and skew, since the lower boundary for $J_{V\infty}$ is zero, and the standard error is often of the same order as the experimental variable. This reduces to the problem of how to identify when an influential point is an outlier due to some unknown experimental artifact, or when it is a valid representation of a biological effect. Suttorp *et al.* 1998, and Dull *et al.* 2001 have used a threshold criterion to eliminate samples with a hydraulic conductivity above a pre-determined limit. The undesirable aspect of this approach makes it difficult to look for defective hydraulic conductivity. If an experimental treatment causes hyperpermeability, the experimentalist must choose an arbitrary threshold to identify what upper limit of hyperpermeability will be acceptable.

In Table (2.6) we compare the effect of two different methods of evaluating outliers among the seven data sets presented in Table (2.3). Applying the statistical rule of excluding as outliers those samples that are 1.5 greater or lesser than the interquartile range, we see that samples 1, 2, are low, and 4 is a high outlier for diffusivity. Applying the thresholding rule for outliers, that monolayers with a Lp higher than 5.0×10^{-7} cm· s^{-1} , we see that samples 1, 4, 5, and 6 are outliers in Jv_{∞}. Removing diffusivity outliers from the data set reduces the standard deviation for Jv_{∞} and diffusivity by 48% and 73% respectively, while increasing their means by 3.7% and 37% respectively. Removing outliers by thresholding has almost no effect on the standard deviation for diffusivity but lowers that of Jv_{∞} by 38% . The thresholding method lowers the mean for diffusivity by 10% and the mean for Jv_{∞} by 49%.

	Diffusivity ($\times 10^{-8}$ $cm^2 \cdot s^{-1}$)	Jv_∞($\times 10^{-6}$ $cm \cdot s^{-11}$)	*Sealing potential* $(1+\gamma)^{-1}$
Entire data set (7 experiments)			
Mean	1.855	5.141	0.2049
Std dev	0.9956	1.888	0.1001
95% confidence interval	± 0.6901	± 1.308	± 0.06938
After removal of outliers by $J_{V\infty}$ threshold < 5.0 × 10^{-7} $cm \cdot s^{-1}$			
Mean	1.667	2.635	0.2747
Std. dev	1.005	1.162	0.09993
95% confidence interval	± 1.138	± 1.315	± 0.09793
After removal of outliers in diffusivity			
Mean	2.541	5.334	0.2243
Std. dev	0.2677	.9884	0.1148
95% confidence interval	± 0.2347	± 0.8664	± 0.1006

Table 2.6) Comparison of methods of identifying outliers. Data are mean, standard deviation, and 95% confidence interval of fitted parameters for the 7 experiments in Table (2.3). Outliers in diffusivity were those that lie farther than 1.5 times the interquartile distance above or below the mean. Outliers in $J_{V\infty}$ were identified as those with $J_{V\infty}$ greater than 5.0 × 10^{-6} cm• s^{-1} After removal of outliers in diffusivity the 95% confidence interval of the true value of the mean was reduced by 33.7% for $J_{V\infty}$ and 66.0% for diffusivity. Removal of outliers by thresholding $J_{V\infty}$ increased the 95% confidence interval for diffusivity by 64.8%, with a small increase in the 95% confidence interval for $J_{V\infty}$. The mean and standard deviation of the sealing potential increased by both methods, but were not statistically different from one method to the other (p > 0.14).

Differences in diffusivity are apparent when Jv(t) is plotted against time as in Figure (2.9) or dimensionless flux is plotted against dimensionless time as in Figure (2.10). Whether the samples are comparable as part of a biologically similar group, or should be excluded, can only be determined by additional experimental considerations, but it can be seen that these parameters offer a physically relevant way to distinguish if like treatments are behaving alike.

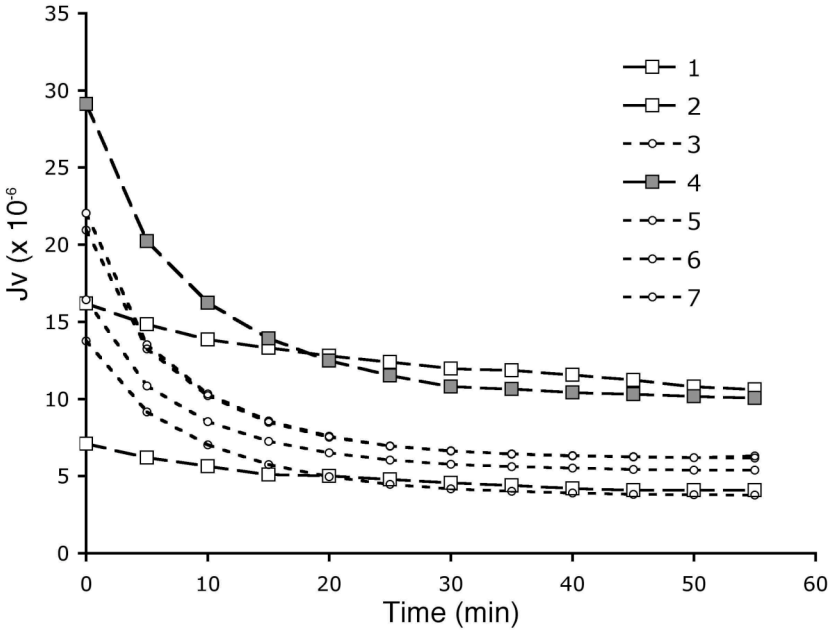

Figure 2.9) Experimental flow rate vs. time curves for 7 experiments. BAEC monolayers cultured in normal 5 mM glucose. Low outliers in diffusivity are shown with white boxes. High outlier in diffusivity is shown with shaded boxes. Other samples are with open circles.

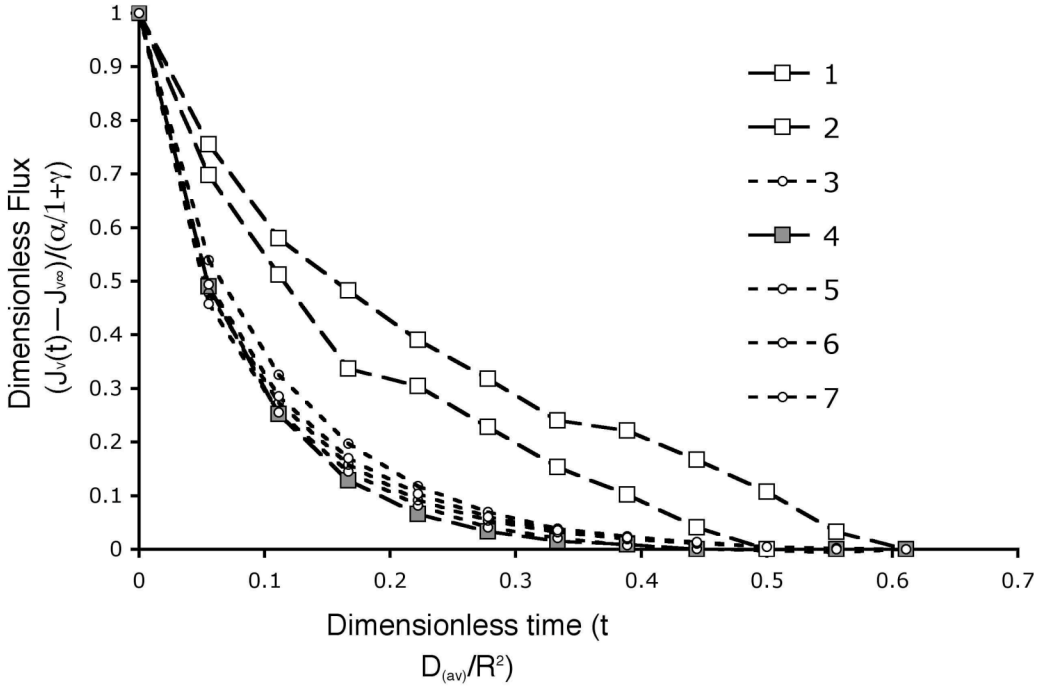

Figure 2.10) Dimensionless J_V vs. time curves. Dimensionless flux is found by subtracting $J_{V\infty}$ then normalizing by $\alpha/(1+\gamma)$. Dimensionless time is $t\langle D\rangle/R^2$, where $\langle D\rangle$ is the average diffusivity for the experimental set. Outliers in diffusivity are shown with square markers (white boxes, low outliers, gray boxes high outlier). Other series are shown with round markers.

Conclusions

Our modeling of the sealing effect is built on the hypothesis that attenuation of flow is a result of the diffusion of protein to the intercellular junction. We have presented here for the first time a biologically relevant model of the sealing effect. Using a simplified model of the mechanism of sealing, we have shown that two novel parameters, in addition to Jv_∞, may be extracted from data, and used to describe the integrity of the endothelium under trans-mural flow. The method also reduces sample variance of calculated Jv_∞, and computational error associated with the numerical approximation of the derivative. The fitted parameters are user independent, reducing the need for subjective tests on the part of the experimentalist. Model results accurately reproduce results of Jv_∞ from data.

Given that our mathematical model is drawn from a simple theory of intracellular mechanics, the extracted parameters may be directly related to physical elements of the cell or of the experimental environment. Diffusivity by motor protein transport depends upon the availability of motor proteins and the presence of intact cytoskeletal elements appropriate for transport. The sealing potential depends upon a sufficient concentration of available sealing proteins in the cytoplasm at the start of the experiment. Other physical parameters taken as constant, such as cell radius R, fluid viscosity μ, the protein reflection coefficient σ, and the osmotic pressure π, may be changed by conducting experiments with different cell types and media conditions. Media conditions may also be changed as a function of time, providing yet another avenue for investigation.

The diffusion model of sealing predicts that cells with pathological diffusivity will exhibit pathological sealing. What constitutes pathological diffusivity within the

cytoplasm is a field ripe for speculation. The activity of motor proteins in concert with microtubules (MT) can now be manipulated with some precision (Drake and Pack 2008), allowing quantitative investigation of the role of this system in maintaining appropriate monolayer sealing. Wu *et al.* report that altering of MT stability by nocodozole (depolymerization) and taxol (hyperstabilization) both cause an increase in endothelial permeability(Wu, Chen *et al.* 2007). However, whether this effect is from inhibition of the diffusion of protein, or from gross morphological disorder cannot be determined from their data: the observed state of the cytoskeleton. Characterization of the diffusivity of junctional proteins would provide an important extension and validation for this work.

It remains to validate the assumptions that the fitted parameters are in fact independent measures of endothelial function. In future experiments, we will test the predicted behavior of our model in two limiting cases. Recent studies by our group have shown that a fraction of trans-mural water flow is through the aquaporin-1 (AQP-1) membrane water channel, a route that is not associated with the tight junction. We will investigate whether chemical or genetic reduction of flow through AQP-1 reduces $J_{V\infty}$ without changing diffusivity or the sealing potential. In a second test, we will conduct experiments to see if fixation of the plasma membrane changes diffusivity and sealing potential without changing Jv_{∞}.

Chapter 3. Validation of the Transport Model

Chapter abstract

To test the validity of the diffusion model of sealing, we perform an analysis on experimental results in which monolayers had been prepared in a way that would independently reduce or eliminate the effect of individual parameters. An analysis was made of experiments in which bovine aortic endothelial cells (BAEC) were grown on transwell filters for use in a pressure-flow apparatus and exposed to one of three different treatments. 1) To test if aquaporin-1 (AQP-1) plays a role in transendothelial water flux, we either blocked AQP-1 with mercuric chloride ($HgCl_2$), or downregulated it with small interfering ribonucleic acid (siRNA). 2) To test if the sealing potential as extracted from data by our model reflects the movement of proteins from the interior of the cell into the junction complex to form membrane bound transcellular structures across the gap between cells, we lightly fixed the plasma membrane by a 10 min exposure to 1% paraformaldehyde. 3) To test if the diffusivity extracted from data by our model reflects a diffusive process, we fixed the cells in 2% glutaraldehyde for 30 to crosslink intracellular proteins *in situ*. For preparation 1), confocal microscopy and western blot analysis was used to detect the presence of AQP1, and to confirm the knockdown by siRNA. Control and experimental monolayers were subjected to convective flow tests, in which a pressure of 10 cm of water was applied across the membrane, and the time-position data was analyzed by the diffusion model of sealing. Experimental monolayers transfected with siRNA showed a downregulation of AQP1 of from 30 to 50%. Volume flow rate was significantly reduced both by $HgCl_2$ blocking (24.5%) and by siRNA

downregulation (62.4%), while the diffusivity and sealing potential were unchanged. Lightly fixed monolayers showed a marked drop in the sealing potential (79.3%), a slight drop in diffusivity (20.0%), and unchanged $J_{V\infty}$. Strongly fixed monolayers showed an 83% drop in diffusivity, unchanged sealing potential, and an 80% drop in $J_{V\infty}$. This provides an experimental validation that the fitted parameters of the diffusion model of sealing conform to the assumptions of our model, and represent meaningful independent measures of the integrity of cultured endothelial monolayers

Introduction: Model predictions

Isoforms of the trans-membrane water channel protein aquaporin (AQP) are found in occluding membranes. In addition to their role in maintaining the proper osmotic force across the plasma membrane, they have been shown to contribute to bulk flow of water through tissue. In the corneal endothelium, AQP are required for fluid transport that is vital to maintain the transparency of the cornea by proper hydration (Li, Kuang *et al.* 1999). In the kidney, AQP are necessary to facilitate solute recovery by reverse osmosis (Nielsen, Smith, Christensen, Knepper *et al.* 1993). AQP has also been found in endothelium (Nielsen, Smith, Christensen and Agre 1993), but its contribution to transport has heretofore remained uncharacterized. Water flow across the endothelium is an important vehicle for the delivery of nutrients to the extra-vascular tissue. However, hyperpermeability of the aortic endothelium has been implicated in the development of atherosclerotic plaque. Water principally crosses the endothelium through breaks in the intercellular junctions, as discussed previously. However, the presence of large concentrations of AQP1 in occluding membranes where they contribute to bulk flow

suggests that they may represent an alternate route for water transport across the endothelium. AQP-1 contains a domain to which anti-AQP-1 antibody (Alpha Diagnostics Intl, San Antonio, TX) will bind, on its c-terminus in the interior of the cell membrane. This binding domain is a sequence of 19 amino acids that shows 100% homology between mammalian species. Although the presence of aquaporin in bovine aorta can be surmised from its presence in other species, our group has recently reported the cross reactivity of cow AQP1 with commercially available AQP1 antibody, and characterized the contribution of AQP1 to the flow of water across the endothelium for the first time. AQP-1 allows the transport of water at a fixed rate per functional unit. Therefore, the contribution of AQP-1 to total flow should be independent of the sealing effect, or the translocation of occluding proteins from the interior of the cell to the tight junction. To test this hypothesis, that trans-cellular water flux through AQP-1 is independent of the sealing effect, we compared $J_{V\infty}$, D, and sealing potential in control monolayers with those in which water transport through AQP1 was blocked by incubation with mercuric chloride ($HgCl_2$) or knocked down by transfection with small interfering RNA (siRNA). Immunohistochemistry was used to localize AQP1 in these BAEC monolayers and to quantify the degree of siRNA knockdown.

The assumptions that underlie the analysis of the diffusivity and sealing potential relate to the mechanisms of chemical fixation. Biological tissues exposed to paraformaldehyde or glutaraldehyde form extensive crosslinks between proteins. The precise mechanism by which these crosslinks are formed is only partially known. One would guess, and what one, in fact, finds, it that the diffusion of proteins, both in the cell

membrane and in the cytoplasm, is observed to decrease with increasing time of exposure to, and increasing concentration of fixative. Possible mechanisms for this reduction of diffusion are 1) crosslinking of free proteins to make larger aggregates which will diffuse slower due to their larger size and solvent drag effects, 2) cytoskeletal crosslinking which may change the path of motor protein transport, and 3) covalent linking of proteins to the cytoskeleton (Kusumi and Suzuki 2005). To test our assumption that the sealing potential depends on the transport of proteins from the interior of the cell to the junctional interface, we expose cells to light fixation in 1% paraformaldehyde, for 10 minutes. We predict that by partially crosslinking membrane proteins, this treatment will reduce the number of occluding proteins that can insert and protrude through the membrane to build the junction, and will reduce their ability to organize a tight junction strand, but will still allow them diffuse from the interior of the cell to its periphery. We predict that this treatment will give normal $J_{V\infty}$, moderately reduced diffusivity, and a dramatically reduced sealing potential. To test our assumption that diffusivity reflects a process of diffusion, we expose cells to stronger fixation in 2% glutaraldehyde for 30 minutes. In this case, we again predict that Jv∞ will be normal, but a more extensive crosslinking of proteins to the cytoskeleton will reduce or eliminate diffusivity, and greatly reduce the sealing potential.

Methods and Materials

Cell culture

12-well filters (Corning 3460) were pre-treated with fibronectin, for 1 hour, then BAEC from passage 4 through 7 were plated at an initial concentration of 32K cells per cm^2. Cells were subsequently cultured in MEM with 10% FBS, penicillin 100 U/ml, streptomycin 2.5 µg/ml, and L-glutamine. Cells were maintained at 5% CO_2 and 37C in an incubator for 3 days until confluent. Immunohistochemistry was performed at confluence or 1 day post confluence. Transport experiments were performed 1 day post confluence.

siRNA

Seven different siRNA transfection experiments were prepared: 1) Control, with no siRNA and no Lipofectamine®2000 transfection vector (vector); 2) Assay negative control, with vector, but no siRNA; 3) siRNA negative control, with vector, and siCONTROL non targeting siRNA (NT-RNA); 4) Target A, with vector and primer design A; 5) Target B with vector and primer design B; 6) With vector and a combination of primers A and B, and 7) Vector negative control with a combination of Target A and NT-RNA but no Lipofectamine®2000. In addition, several wells of preparations 4 through 6 included NT-RNA for confirmation of transfection. Two duplex siRNA were designed using the web-based siDESIGN® Center (Dharmacon, Inc. Lafayette, CO), target 1 NNCCAGCGAGUUCAAGAAGAA—with primers sense: CCAGCGAGUUCAAGAAGAAUU, and antisense UUCUUCUUGAACUCGCUGGUU. And target

2, NNGCGGUCAGGUGGAGGAGUA—with primers sense GCGGUCAGGUGGAGGAGUAUU, and antisense UACUCCUCCACCUGACCGCUU. The sequence used as a non-targeting siRNA (NTRNA) was siGLO® red (D-001630-02-02, Thermo Fisher Scientific, Lafayette CO) tagged with a fluorescent marker, and has been shown by the manufacturer to have no effect on protein expression. siRNA transfections were performed using a modification of the method described in (Kou, SenBanerjee *et al.* 2005). In brief, 20 pmol siRNA per 1.5×10^4 cells was transfected using Lipofectamine®2000 (0.15%, v/v) following the protocol provided by the manufacturer when cells were approximately 80% confluent. Transfection media was removed 6 h post-transfection and replaced with pen-strep free MEM. Cells were analyzed 48 h following transfection. Optimization of siRNA was performed by treating similar monolayers with 0, 20, 40, or 80 pmol siRNA per 1.5×10^4 cells, with and without Lipofectamine®2000 then assaying relative protein content by western blot. Wells that were prepared for transport experiments were also analyzed for relative protein concentration by semi-quantitative immunofluorescence, and western blot as described below.

Immunohistochemistry for fluorescence microscopy (performed by Tieuvi Nguyen, Ph.D., a fellow researcher in our lab)

BAEC monolayers were fixed for 1 hour in 4% formaldehyde, washed three times in PBS, permeabilized with 0.075% saponin in PBS for 20 minutes, and washed three more times in PBS. The monolayers were then incubated in blocking solution (3% goat serum, 0.3% Triton X-100, 20 mM NaPO4, and 0.9 mM NaCl) for 30

minutes. The blocking solution was removed by aspiration, and the monolayers were exposed to rabbit anti-rat AQP1 antiserum (Alpha Diagnostics Intl, San Antonio, TX) diluted in 15% goat serum and 0.2% BSA in PBS. The primary antibody was diluted 1:500. Control filters were not incubated with the primary antibody. The incubation was done in a humid chamber at room temperature for 90 minutes. The cell layers were subsequently washed three times with PBS and two times with PBS plus 5% goat serum. They were then incubated with Alexa-488 conjugated goat anti-rabbit IgG (Molecular Probes, Carlsbad, CA) at a dilution of 1:200 (in PBS plus 1% goat serum) for 90 minutes. The samples were stored in a humid chamber in the dark. The monolayers were washed four times with PBS before imaging with a Nikon Eclipse TE2000-E microscope.

Immunohistochemistry for confocal imaging (conducted by J. Toussaint, a fellow Ph.D. candidate in our lab)

Experimental filters were permeabilized and incubated in blocking solution as above. The time of incubation in primary antibody was 18 hours, at a dilution of 1:500 (i.e.2mg/ml). For control experiments, PBS replaced the primary antibody. Filters were then washed in PBS three times and incubated in secondary antibody as above at a dilution of 1:50 in PBS for 90 minutes at room temperature. Samples were washed in PBS three times and mounted on slides with Vectashield® mounting media for fluorescence (Vector laboratories, Burlingame, CA). Coverslips were securely applied to the samples using clear nail polish. The samples were stored as above. Samples were

viewed and captured using a Leica TCS SP2 AOBS confocal microscope. Image analysis was done with the Leica confocal software TCS SP/NT version 2.5 1347d.

Western Blot (conducted by Y. Xue, a fellow Ph.D. candidate in our lab)

BAEC cells were lysed with ice-cold RIPA buffer containing protease inhibitor cocktail for 20 minutes, followed by sonication for 10 seconds. Protein concentration was determined using a variation of the Bradford assay, the Caymen protein determination kit (070040 Caymen Chemical Co., Ann Arbor, MI). Before loading, cell lysates were incubated with PNGase F enzyme at 37C for 1hour (New England Biolabs, Ipswich, MA). 20ug protein in a total volume of 50µl loading buffer was placed in each lane, for 5 minutes at room temperature and then separated on a 12% SDS-polyacrylamide gel by electrophoresis. The proteins were transferred to PVDF membranes and blocked with 5% milk for 1hour. Immunoblot was performed using rabbit anti-rat AQP1 polyclonal antibody at a 1:1000 dilution (11-A, Alpha Diagnositics, San Antonio, TX) overnight and horseradish-conjugated donkey anti-rabbit secondary antibody at a dilution of 1:4000 for 1 hour. Immunoreactivity was visualized using enhanced chemoluminescent kit (Amersham, Arlington Heights, IL). Densitometry was determined using Quantity One software. The membrane was reprobed with b-actin antibody as a loading control.

Water Flux measurements

Measurement of water and solute flux. The pressure flow apparatus as described in the previous chapter was used to measure the flow of water across BAEC.

Fixation Experiments

Data from the paraformaldehyde fixation experiments was provided by L. Cancel, a Ph.D. candidate in the Wallace Coulter Lab, J. Tarbell, director. Cells were prepared as follows: culture media was removed, filters were washed 3 times with PBS, then immersed in freshly made 1% paraformaldehyde at room temperature for 10 minutes, then used in the pressure-flow apparatus as previously described. Glutaraldehyde fixation procedure, performed by Y. Xue, was exposure to 2% glutaraldehyde for 30 minutes, then used in the pressure-flow apparatus.

Results

Localization of AQP-1

Cross reactivity of AQP-1 antibody with bovine aquaporin

The images below are representative of experimental results. For the $HgCl_2$ blocking experiments, 12 filters of BAEC monolayers were prepared as above, 4 were selected at random for imaging, and 8 for paired transport experiments. Figure (3.1) shows the immunostaining of AQP1 (green) with Alexa-488 conjugated secondary antibody, and propidium iodide nuclear staining (red) to identify each endothelial cell's nucleus by transmission fluorescence microscopy. The immunoreactivity is strongest near the nucleus of the cells and fades near the cell's periphery, indicating that aquaporin may be more densely distributed in the apical and basal membranes of the cell, and less

dense near the intercellular cleft. Anti-AQP-1 staining can clearly be seen above the nucleus (arrows).

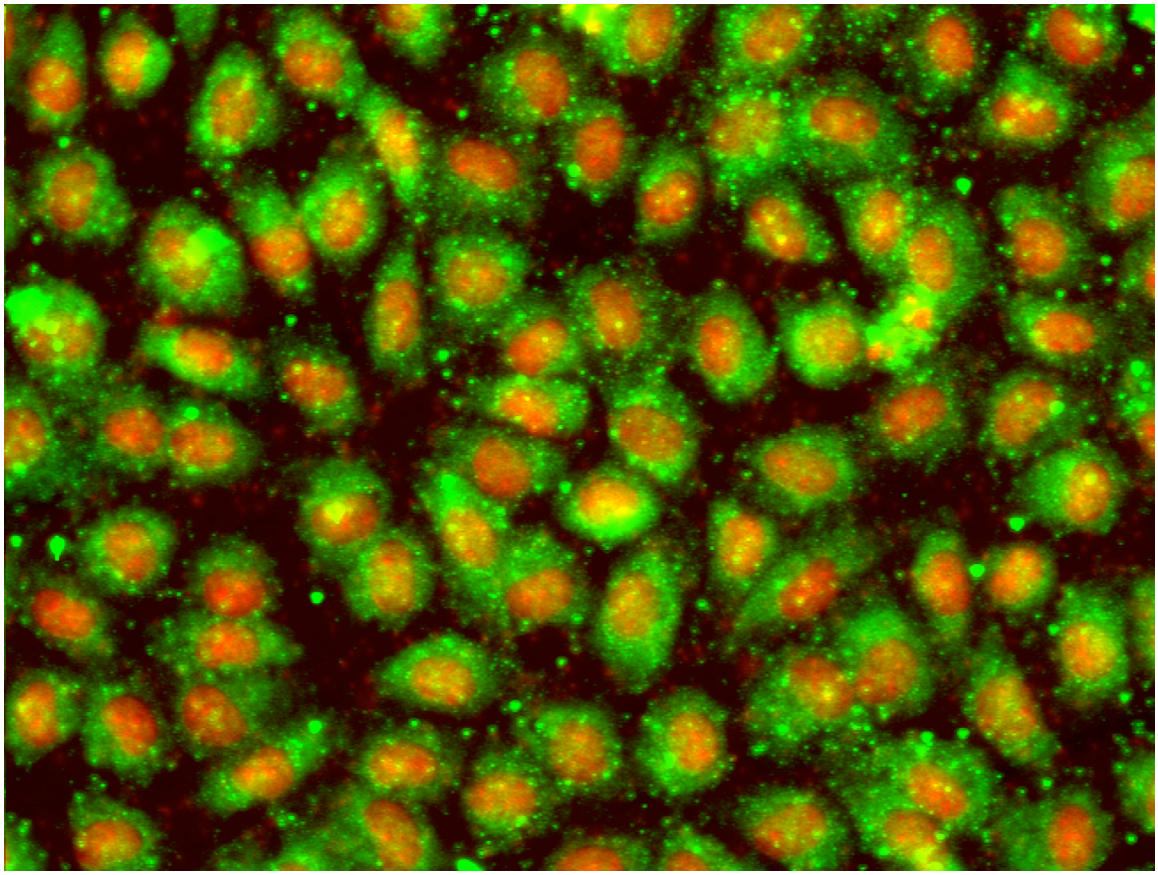

Figure 3.1) BAEC monolayer, showing AQP1 antibody and propidium iodide nuclear stain. AQP1 shows higher concentration near the center of the cell. Note that AQP1 staining can be seen overlaid upon the nuclear stain. Since AQP1 is excluded from the interior of the nucleus (Figure 3), this demonstrates the presence of AQP1 in the apical membrane of the cell. (Magnification: 20×)

Western blot analysis of siRNA knockdown

Figure (3.2) shows the result of a western blot analysis. Target B AQP-1 siRNA decreased the amount of protein by 41.2% relative to vector control ($p < 0.001$ $n = 4$). Target A (data not shown) showed no decrease in AQP-1 expression.

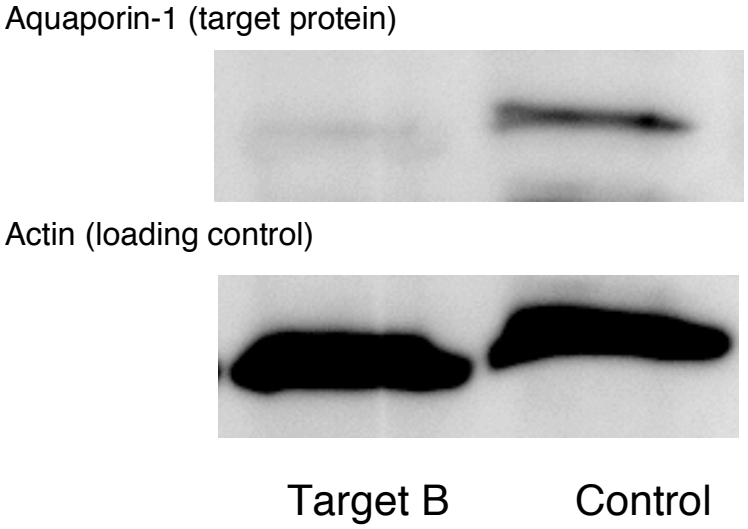

Figure 3.2) Result of western blot detection of aquaporin-1 knockdown by siRNA. Target B showed a 41.2% reduction in the amount of AQP-1 in cell lysates relative to control. Results were normalized to actin content. No difference was found between target A and target B.

Immunofluorescent detection of siRNA and AQP-1

In Figure (3.4) integrated images of optical slices for anti-AQP-1 staining (green, Figure (3.4A), and Rhodamine-tagged NTRNA (red, Figure (3.4B) are overlaid in Figure (3.4C). The integrated images, in contrast to Figure (3.3), do not span the height (in the *z*

direction) of the cell layer, but are restricted to the intracellular domain. Figure (3.4) reveals a co-localization of AQP-1 antibody with a tortuous internal structure surrounding the nucleus, fading away at the cell periphery as in Figure (3.1). The antibody is conspicuously absent from cell nuclei. The presence of red staining in the nuclear region, and the indistinct boundary of the nucleus, as shown in Figure (3.4B) is evidence of translocation of the exogenous NTRNA into the nucleus, since, as shown in Figure (3.4A) the plane of the image is directly through the *z* coordinate center of the nucleus.

For siRNA confocal imaging, 24 wells of BAEC cultured as above were prepared for siRNA permeability studies, 5 of which were selected at random for analysis by confocal microscopy, the remaining were used in the transport apparatus. Figure (3.3) shows a fluorescent image taken by confocal microscopy overlaid upon a transmission optical image of the same field of view. The transmission image of Figure (3.3) shows the typical cobblestone morphology of cultured BAEC. The fluorescent image of Figure (3.3) is the integration of optical sections spanning a *z* range (in the direction perpendicular to the plane of the image) of ± 3 μm from the *z* coordinate centre of the cell. The strong correlation of Rhodamine dye (red) with the cell body in the transmission image is evidence of penetration of the NTRNA into the cytoplasm. In some clusters or pairs (of perhaps recently mitotic) cells a much higher amount of NTRNA is seen in the cytoplasm, although in other cells uniform numbers of stained blobs can be seen throughout.

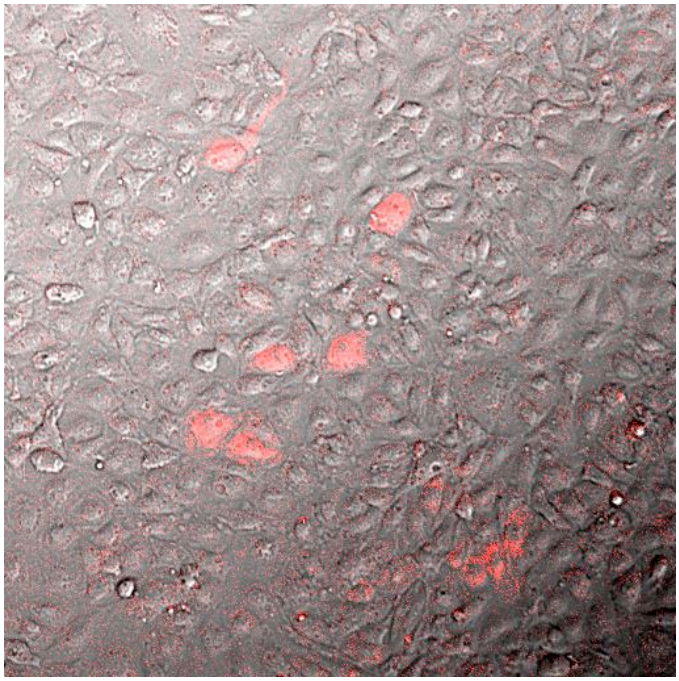

Figure 3.3) Transfection of non-targeting siRNA (NT-RNA) in cultured BAEC without transfection vector. Uneven transfection is revealed by the contrast in staining intensity between cells. Strong transfection is associated with mitotic cells (arrow). Absence of staining in intercellular clefts and presence of staining in the body of cells indicates NT-RNA penetration into the cell.

In post-transfection cells, the presence of AQP1 antibody is greatly reduced. Confocal images taken for the purpose of semi-quantitative analysis show no visible anti-AQP-1 staining—they are completely black—and for that reason are not shown here. Quantitative analysis of theses same seemingly empty images indicates a 50% reduction in the strength of the anti-AQP-1 fluorescent signal.

Figure 3.4) (following page) Confocal images of Alexa488-tagged AQP1 antibody and FITC-tagged NT-RNA. The focal plane of these images is through the interior of the cell, as shown by the exclusion of AQP1 anitbody from the interior of the nucleus. A) AQP1 has a higher concentration in the cytoplasmic structures around the nucleus than at the cell border. B) The presence of NT-RNA in the same focal plane and colocalized to the cell nucleus is evidence of transfection. C) shows an overlay of the two images A and B.

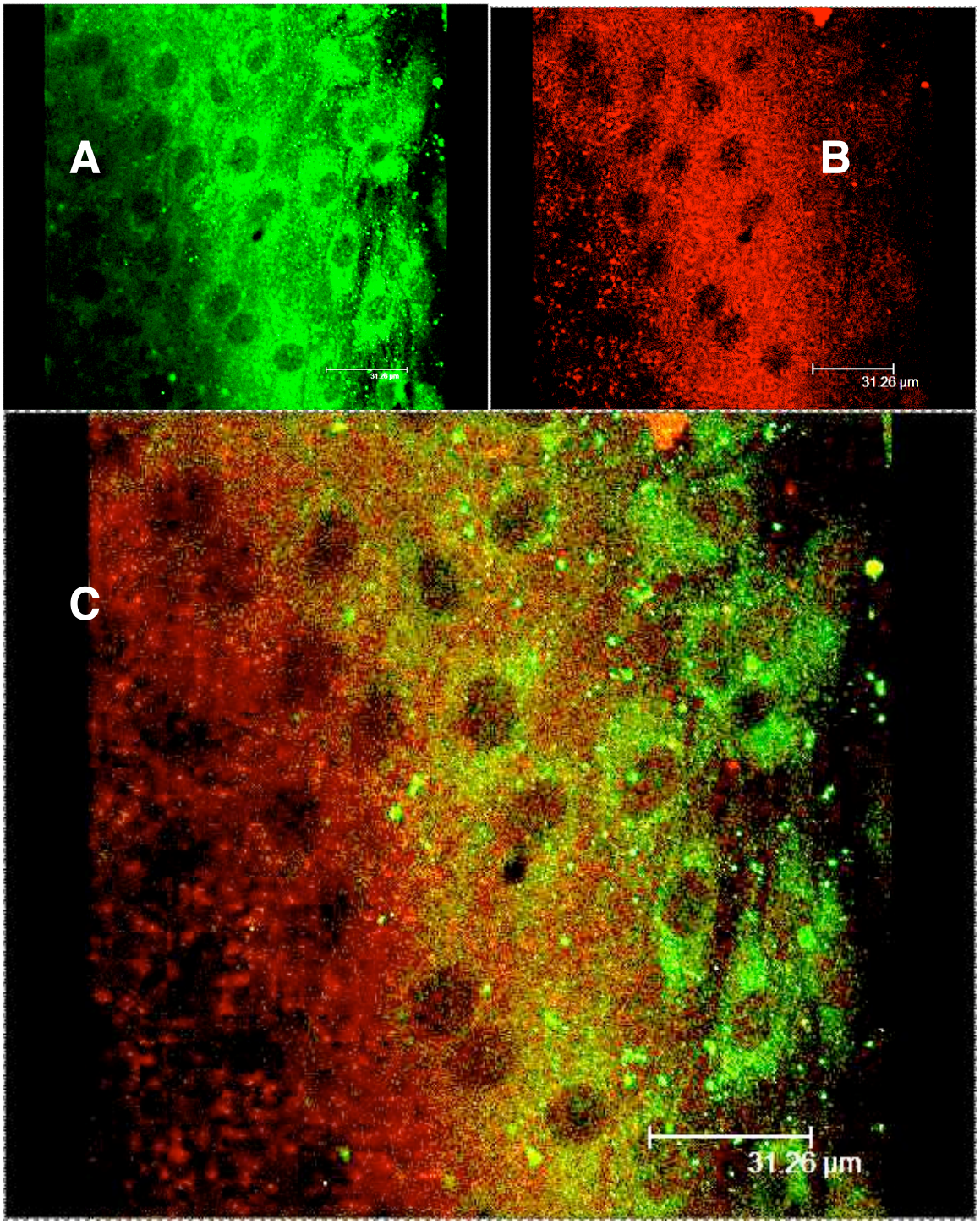
A
B
31.26 µm
C
31.26 µm

Transport

***In vivo* water flux measurements across BAEC monolayers with AQP1 blocking by $HgCl_2$**

The steady state water flow is the combined flow from four different sources, 1) flow through sealing tight junctions, 2) flow through leaky junctions around mitotic or apoptotic cells, 3) flow through holes or defects in the monolayer, and 4) transcellular flow through AQP-1. We expected J_V of BAEC monolayers incubated in $HgCl_2$ to be lower than control filters not exposed to $HgCl_2$. (Nguyen, thesis 2008) had already shown a reduction in *Lp* in rat aorta explants for similar treatment with $HgCl_2$ and with mercapto-ethanol. Although HgCl2 is known to block AQP-1, it also has a cytotoxic effect at high enough concentrations and exposure times. The optimal concentration of $HgCl_2$ to preserve of cell viability and yet significantly block AQP-1, was determined by (Nguyen, thesis 2008) to be 25μM. (Nguyen, thesis 2008) found approximately 80% blocking in whole vessel at 1mM $HgCl_2$. At 25μM, we expect to see a partial blocking of AQP-1 and a less than maximal reduction in J_V, with no change in diffusivity or sealing potential. Pairs of control and experimental filters were run in parallel. Experimental Jv was significantly lower than control ($p < 0.05$).

We exposed control filters (n = 6) to standard media on the luminal and abluminal membranes as described above, and experimental filters (n = 6) to a 25μM $HgCl_2$ solution on the luminal side for parallel experimental J_v measurements. Table (3.1) shows the results of 6 pairs of filters. The J_v of experimental filters was lower than

controls by an average of 24.5% ($p < 0.05$). After each experiment, filters were viewed using phase contrast light microscopy, which revealed that the monolayers remained intact throughout the experiment. Table (3.1) (results repeated in Figure (3.5)) shows that after partial blocking of AQP-1 by $HgCl_2$ there was a significant decrease in $J_{V\infty}$, but no significant change in sealing potential, or diffusivity.

***In vivo* water flux measurements across BAEC monolayers with AQP1 knockdown by siRNA.**

In contrast to the $HgCl_2$ experiments, knockdown from siRNA should offer a greater decrease in functional AQP-1 without cytotoxic effects of the experimental reagent. However, since the role of AQP-1 is vital to the osmotic regulation of intracellular pressure, it is possible that depletion of AQP-1 will kill the cells directly. Figure (3.5) presents values of $J_{V\infty}$ for six of our seven experimental treatments, excluding the vector negative (no Lipofectamine 2000) preparation which we did not subject to pressure-flow tests. Values were extracted by our transport model from data collected as previously described. Assay control monolayers, which had been treated only with the transfection vector Lipofectamine®2000 (n = 3), or the vector plus a non-reacting scrambled interfering RNA (n = 3) did not show a significant difference to control ($p > 0.3$). The $J_{V\infty}$ of all experimental filters was lower than controls by an average of 62.4 ± 1.7 % ($p < 0.001$). After each experiment, filters were viewed for integrity as above.

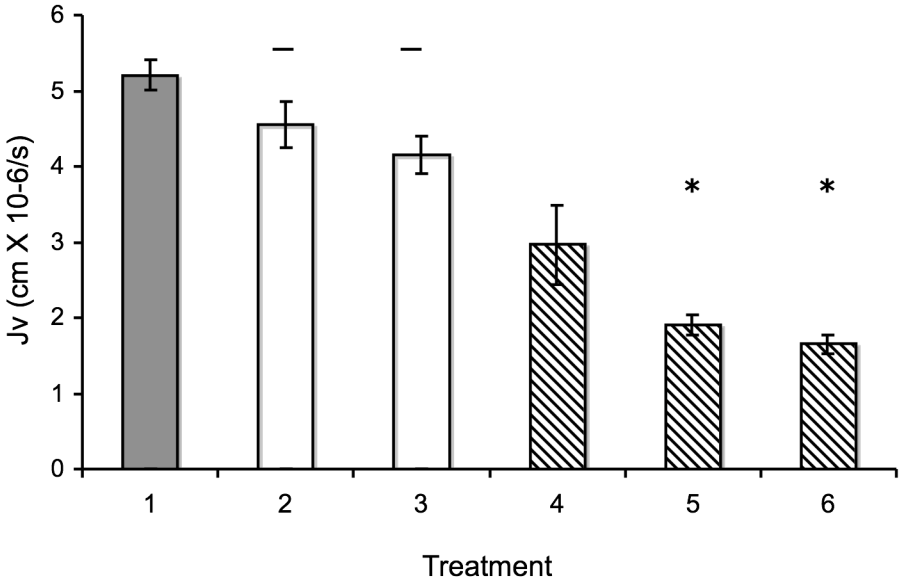

Figure 3.5) Steady-state water flux through BAEC monolayers is reduced after treatment with siRNA targeting aquaporin-1. Six treatments are compared: 1) Control, solid bar; 2) Negative control, with transfection vector, but no siRNA and 3) Negative control, with vector, and non targeting siRNA (NT-RNA) open bars; and 4) , 5), and 6) shaded bars, target A, B, and A plus B, respectively. Flux was significantly reduced in monolayers treated with target B and a combination of A and B (* $p < .01$ $n = 6$) vs. control ($n = 10$). No effect was found for monolayers treated with Lipofectamine®2000 alone or with NT-RNA ($n = 15$). No significant effect of target A can be reported for $n = 3$. Error bars are ± standard error of the mean

Table (3.1) presents the other model parameters extracted from these siRNA treatments. Diffusivity was indeed unaffected by blocking or knockdown of AQP-1. A slight, although not significant, reduction in the sealing potential that was observed in the siRNA knockdown ($p = 0.06$), may indicate some slight interaction between downregulation of AQP-1 and the proteins that make up the tight junction complex, or motor proteins.

25 μM $HgCl_2$ Inhibition of Jv	Control	Experiment	*p value*
J_v x 10^{-6} cm/s/mmHg	5.25 ± 0.45	3.96 ± 0.41	0.03 *
Diffusivity × 10^{-8} cm^2/s	2.723 ± 0.20	2.821 ± 0.36	0.41
Sealing Potential (mol protein / mol protein)	0.0724 ± 0.01	0.0838 ± 0.02	0.31
Number of observations	6	6	
SiRNA Inhibition of Jv			
J_v x 10^{-6} cm/s/mmHg	6.71 ± 1.14	2.52 ± 0.50	< 0.01 *
Diffusivity × 10^{-8} cm^2/s	3.193 ± 0.53	2.993 ± 0.55	0.40
Sealing Potential (mol protein / mol protein)	0.0674 ± 0.01	0.0462 ± 0.01	0.06
Number of observations	6	9	

Table 3.1) Effect of reduced water flux through aquaporin-1 by mercuric chloride blocking, or by siRNA knockdown.

Reduction of sealing potential by fixation of the plasma membrane

Table (3.2) presents the results of model parameters extracted from experiments on fixed monolayers. The sealing potential is the ratio of the amount of active protein—

that which is transported from the interior of the cell during the sealing process—to the total amount of junctional protein. Our results show that fixation did not change $J_{V\infty}$, but had a dramatic effect on sealing potential and diffusivity. Sealing potential was reduced by 79.3 ± 4.2% in paraformaldehye ($p < 0.001$), but unchanged in glutaraldehyde ($p = 0.18$). Diffusivity was reduced by 20% in paraformaldehyde ($p < 0.025$) and 82.5 ± 1.5 % ($p = 0.002$) in glutaraldehyde.

	Control	Paraformaldehye	p value
Jv x 10-6 cm/s/mmHg	5.32 ± 0.46	5.33 ± 0.96	0.50
Diffusivity × 10-8cm2/s	2.485 ± 0.157	1.989 ± 0.125	< 0.025
Sealing Potential (mol protein / mol protein)	0.0792 ± 0.0069	0.016 ± .0038	< 0.001
Number of observations	5	4	

	Control	Glutaraldehyde	p value
Jv x 10-6 cm/s/mmHg	5.82655 ± 1.64	1.187 ± 0.65	0.035 *
Diffusivity × 10-8cm2/s	2.778 ± 0.372	0.4849 ± 0.0446	0.002 *
Sealing Potential (mol protein / mol protein)	0.1571 ± 0.01	0.1096 ± 0.03	0.18
Number of observations	4	4	

Table 3.2) Effect of fixation on model parameters. Lightly fixed monolayers (paraformaldehyde) showed a 80% decrease in sealing potential, and a 24% drop in diffusivity, with unchanged $J_{V\infty}$. Strongly fixed monolayers showed an 83% drop in diffusivity, unchanged sealing potential, and an 80% drop in $J_{V\infty}$.

Discussion

Sealing effect is independent of steady-state water flow

In Table (3.1) and (3.2) we show that the rate of sealing in the sealing effect—the attenuation of flow by diffusion of occluding proteins to the cell border in response to increased transmural flow—does not happen to be coupled to the steady-state water flux across the monolayer. That is to say, our model fitted parameters show that D varies independently of $J_{V\infty}$ between different treatments, supporting our assumption that flow through a non-sealing pathway is independent of protein diffusivity. It has been previously thought that water flow was restricted to the tight junction, leaky junctions around dying or mitotic cells, or through holes in the monolayer, and that this steady state flow was entirely through these defects in the monolayer. Although transcellular transport through vesicles has been shown to exclude water (Cancel, Fitting *et al.* 2007), the $HgCl_2$ results of {Nguyen, 2008} shown in Table (3.1), and the current siRNA results indicate that a transcellular path through the apical and basal aquaporins may contribute significantly to total water flux. Although the extent of blocking of AQP-1 by HgCl2 is not known, siRNA knockdown of AQP-1 was quantified by immunofluorescence (~50% reduction, Toussaint, 2008 unpublished results) and by western blot (~29% reduction, Xue 2008 unpublished results), whereas flux was reduced by 62.4%. The observed decrease in $J_{V\infty}$ is greater than the calculated knockdown, a result that indicates further investigation is required to fully evaluate this phenomenon. We hypothesize that there are other factors, such as altered cell morphology in response to flow, that contribute to

the reduction of flow in these experiments, but resolution of the details of protein quantification and correlation to flow for these preliminary results are beyond the scope of the current investigation and we do not attempt it here. Although the results are in qualitative agreement (i.e. less AQP-1), an exact comparison of results will require extensive investigation into the differences introduced by these disparate sample preparation methods.

Downregulation of AQP-1 reduces water flow across the endothelium

Since AQP-1 is vital to the maintenance of osmotic pressure in the cell, it is likely that severe downregulation of this protein will prove toxic. In our experiment, although monolayers were confluent at 48 hours, they exhibited a slightly irregular morphology, with some cells (approximately 10 %, data not shown) appearing to grow slightly over neighboring cells. Complete disruption of the monolayer and massive cell death was observed 72 hours after transfection. The disruption of normal osmotic functioning is likely to have other effects on the cell as well. Inability to regulate internal water volume could lead either to cell swelling or shrinkage, which would have opposite effects on water flux through the monolayer. The reduction in the number of AQP-1 in the plasma membrane achieved in our experiment results in a macroscopic change of cell morphology (results not shown) but it is difficult to tell if it is the result of an osmotic imbalance. If shrinkage occurs, the cell aspect ratio of height to radius will decrease, making the cell flatter, which could allow the edges of the cell to form flaps or wrinkles that overlap the junction. This more flaccid membrane would also be more likely to be pressed upon the filter holes under the cell, and by obstructing the pores, reduce flow.

Swelling would presumably lead to a more spheroid shape, or possibly even lysis, and a widening of junctions and increase in flow would result. In the present study, since it was observed that $J_{V\infty}$ decreased, it seems that lysis was not significant. The fact that diffusivity remains constant under light fixation indicates that the basic mechanics of sealing are unchanged, and that the decrease of flow beyond that predicted by a strictly linear relationship between AQP-1 and $J_{V\infty}$ must come from a mechanical component, and is not related to the sealing effect.

Light fixation does not eliminate the sealing effect, but strong fixation does

One of the assumptions of the transport model is that protein diffusion is the limiting factor in the rate of junction sealing. In Table (3.2) we show that light fixation of monolayers showed a slight reduction in diffusivity, and a strong reduction in sealing potential. This means that the amount of sealable junction that dynamically seals during the experiment is less, but that it seals at almost the same rate as normal. An interesting discrepancy is presented by this data. If there is less dynamic sealing per sealable junction, for the same initial amount of open fraction, then $J_{V\infty}$ should be higher, not, as our results show, the same as control monolayers. The implication of this result is that either 1) the initial condition—how much junction is sealed before the start of the experiment—is not the same between treatments, or 2) the dynamic reorganization of the tight junction under flow involves both a rapid (< 5 minutes) initial unsealing of the junction, followed by the experimentally observed sealing effect. We speculate that fixation of membrane proteins by paraformaldehyde could conceivably lead to our result by either mechanism. Crosslinking of membrane proteins in adjacent cells could cause

an increased fraction of pre-sealed junction. The same crosslinking of tight junction proteins could prevent a dynamic unsealing and resealing if such a mechanism actually exists. A reorganizational mechanism, although speculative on our part, is not inconsistent with endothelial function, in particular that of the actin cytoskeleton, which is observed to depolymerize and repolymerize in response to flow (Osborn, Rabodzey *et al.* 2006; Yao, Rabodzey *et al.*). Although in the formulation of the model we suggested that the process modelled as diffusion might in fact be motor protein transport, we have noted that it is a lumped parameter, and may include other forms of transport. A more detailed study of the exact mechanics of protein transport and diffusion as it applies to the sealing effect is called for to resolve this issue.

We apply the same analysis to the results of the glutaraldehyde fixation experiments in Table (3.2). Model diffusivity is reduced by an order of magnitude in glutaraldehyde fixation, meaning that sealing protein is arriving at the junction much slower than in unfixed monolayers. But sealing potential is unchanged, which means that the fraction of sealable junction sealed during the experiment is near normal values. If the initial amount of open junction is the same, then $J_{V\infty}$ will be the same, but the attenuation of flow will be slower. If there is a transient disintegration of the tight junction under flow, then we would expect it to be prevented by glutaraldehyde fixation, and, in addition to a slow rate of sealing, the final value of $J_{V\infty}$ will be lower than for control experiments. The data in Table (3.3) supports the latter speculation, rather than the former. The reduced diffusivity suggests that protein translocation is required for junction formation and the speed at which it arrives governs the rate of sealing. The

reduced $J_{V\infty}$ in the presence of normal sealing potential suggests that a transient disruption of the tight junction at the initiation of sealing is prevented by strong fixation.

Chapter 4. Hyperglycemia and Barrier Function

Chapter abstract

To investigate the relationship between endothelial dysfunction and high blood glucose we cultured bovine aortic endothelial cells (BAEC) in confluent monolayers on polycarbonate filters in a series of increasing glucose concentrations from 5mM (normal) to 30mM (hyperglycemic). The hydraulic conductivity of water, and the convective and diffusive transport of low-density lipoprotein (LDL) through experimental monolayers in response to a 10-cmH_2O-transmural pressure gradient was measured using a pressure-flow apparatus. We developed a mathematical model of intracellular protein diffusion to extract parameters from this data to quantify the initial volume flow rate, the rate of attenuation of flow by the dynamic sealing of the monolayers, and the steady-state hydraulic conductivity. Analysis of these extracted parameters revealed that endothelial monolayers grown in high glucose media have a statistically higher permeability to water and solute compared to cells grown in normal glucose media. Steady state hydraulic conductivity increased by 57.9 ± 10.0 % at 30 mM glucose, and by 30.1 ± 12.3 % at the physiologically relevant level of 10 mM glucose, compared to normal. A similar trend was observed for the initial water flux for the same conditions. Permeability to LDL increased by 46.8 ± 14.1 % at 30 mM glucose, and 42.1 ± 8.1 % at 10 mM glucose. Further analysis revealed that the dynamic response of cells grown in high glucose was significantly slower at physiological levels of hyperglycemia. We conducted parallel investigations into the effect of the depletion of adenosine tri-phosphate (ATP), caused

either by 1) high glucose mediated activation of the DNA repair enzyme poly(ADP-ribose) polymerase (PARP), or 2) antimycin-A induced chemical impairment of the mitochondria. Our results support the hypothesis that increased steady-state hydraulic conductivity and LDL permeability are strongly linked to ATP depletion independent of mechanism.

Introduction: Diabetes and ATP depletion

Diabetes and PARP

The goal of this section is to determine the extent to which cell dysfunction can be correlated to high glucose induced ATP depletion. In diabetes, vascular complications principally manifest as the development of CVD the large arteries and hyperpermeability of the retinal microvasculature (Dvorak, Brown *et al.* 1995). As outlined in previous chapters, our current understanding of the cascade of events which lead to cell dysfunction starts with over activation of the mitochondria and subsequent production of ROS, leading to DNA damage, PARP activation, and the initiation of the molecular pathways of diabetic complications including increased polyol pathway flux, the activation of protein kinase C, and accelerated non-enzymatic formation of advanced glycation end products ((Brownlee 2005)King, 1996; Carter and Grant, 1997). Macroscopic dysfunction, such as reduced endothelium mediated vasodialation, and pathological thickening of the basement membrane, is another way to characterize endothelial dysfunction (Giugliano et al., 1996; Honing et al., 1998; Lyall et al., 1998; Cai and Harrison, 2000). (Soriano, Pacher *et al.* 2001) showed that upon activation of PARP there is a massive depletion of NAD+ and NADH in hyperglycemia, a resultant

depletion of ATP and other nucleotide phosphates, and impaired vasodialative response. On the hypothesis that the impaired vasodialative response of the endothelium was dependent on the NADH-dependent production of endothelial nitric-oxide synthase (eNOS), they blocked the activity of PARP and were able to show improved vascular function upon restoration of NADH and ATP. Aortic endothelial barrier function has also been shown to be compromised in diabetes by evidence of increased diffusive transport to 70 kD dextran (Mimura, Umeda *et al.* 1995) and LDL (Duan, Paka *et al.* 2005). Because the dominant mode of molecular transport across the endothelium is by convection and because of the significant changes in barrier function that result from the sealing effect, a study of convective transport is needed to more fully characterize the integrity of the endothelial barrier function in diabetes. In this chapter we present the results of a study of aortic endothelial barrier function to transmural water flux and dextran under pressure in high glucose cell culture. In addition, we extend the investigation of Soriano (2001) into hyperglycemia induced ATP depletion to correlate the convective transport dysfunction of the endothelial monolayers to ATP depletion and the effect of PARP blockade.

Decreased Barrier Function

Forty percent of the adenosine nucleotide pool in a living cell, either as ADP bound to f-actin, or as ATP bound to g-actin, is permanently committed to the maintenance of the dynamic state of the actin cytoskeleton (Carlier, 1992). Every molecule of actin in the cytoplasm is bound to an adenosine di- or tri-phosphate molecule. The periodic depolymerization of f-actin (and MT which rely on GTP in the

same way) makes the cytoskeleton a net ATP consumer. Since the occluding proteins of the tight junction are bound to the actin cytoskeleton, it follows that the maintenance of proper barrier function not only requires a minimum concentration of ATP, but also requires the consumption of ATP. The barrier function of the endothelium is measured in two ways, either by the transport of tracer solute by diffusion, or by water and solute in convection. Increased permeability by diffusion in diabetes has been established; increased transport of macromolecules in hyperglycemia was one of the earliest observed effects of laboratory models of diabetes, and is summarized in (Popov and Simionescu 2006). However, these results have a marked lack of relevance to the *in vivo* state. Preliminary results by several researchers have revealed that convective transport may also be increased in diabetes, but remain difficult to validate. Early work by Wilson (1990) reported that ATP depletion alone was not enough to account for observed increases in permeability to macromolecules (Wilson, Winter *et al.* 1990).

Contribution of this paper

The first major result of this research is to confirm evidence of a glucose mediated ATP-dependent increase in permeability of the endothelium to water and solutes. Secondly, we show that the sealing effect, in general, is not ATP-dependent for the same preparations. Thirdly, we show that restoration of ATP levels by blocking PARP is not successful in restoring barrier: an excess of ATP in a PARP depleted state reduces, rather than increases, barrier function independently of glucose concentration.

Experimental Design

Apoptosis, permeability, ATP, ROS, and PARP

We have investigated dysfunctional permeability using cultured BAEC monolayers in the pressure-flow apparatus described previously. We measured endothelial barrier function—hydraulic conductivity (Lp), and solute permeability (P_e)—and compared the diffusivity of intracellular junctional protein, and of the sealing potential, as described in the previous chapter. Barrier function is known to be dependent on ATP (Bacallao, Garfinkel *et al.* 1994; Mandel, Doctor *et al.* 1994), and also has been reported to be dependent on the number of apoptotic cells (Childs, Tharakan *et al.* 2007; Gules, Satoh *et al.* 2003) and the level of activated PARP (Szabo 2005). So we measured intracellular levels of ATP, PARP, and rates of apoptosis and correlated barrier dysfunction to abnormal levels of each. Cells were grown in a graded series of glucose concentrations, from normal (5mM) to high (30mM) to determine if cell dysfunction was a linear in glucose. Our experimental hypothesis, based on the unifying mechanism proposed by Brownlee, is that hyperglycemic cell dysfunction occurs only as a downstream result of ATP depletion by PARP activation. Our question is whether is it PARP activation which directly causes the dysfunction, or if sub-lethal ATP depletion is the culprit.

To measure the effect of ATP depletion, we blocked the mitochondrial electron transport chain by treatment of monolayers with antimycin-A. Antimycin-A is a Gram-negative antibiotic that binds to the mitochondrial membrane, and reduces intracellular ATP by inhibition of oxidative phosphorylation. Because the specific action

of antimycin-A is to disrupt the electron transport chain, a byproduct of this treatment is the production of superoxide radical, and subsequent activation of PARP. This treatment allows the parallel investigation of PARP related dysfunction and non-PARP mediated ATP depletion.

Our experimental strategy can best be explained by the figure below, which summarizes known pathways of cell dysfunction in hyperglycemia. The macroscopic conditions are shown in rectangular boxes I and II: hyperglycemia leads to cell dysfunction. Hyperglycemia is known to lead to the intermediate states shown in the circles in between: through pathway (10) to state A, activation of PARP; and by pathway (2) to state B, ATP depletion. In addition, PARP activation (B) is known to lead by pathway (3) to ATP depletion (B). Two measures of dysfunction, apoptosis, and an increase in diffusive permeability are known results of PARP activation and ATP depletion but it is unknown whether they occur through pathway (4), (5), or a combination of the two. Hydraulic conductivity has not previously been measured for these conditions but is by hypothesis also induced by pathway (4) or (5). The numbered arrows that connect the endpoints and the transitional states indicate the pathways we investigated. Our results showed a linear relationship between increasing media glucose concentration, PARP activation, and ATP depletion. In addition we showed that cell dysfunction increased linearly with ATP depletion, but that normal function could not be restored in high glucose by the addition of a PARP blocker. When PARP activity was reduced to levels below that found in cells exposed to normal glucose, even though ATP levels were increased above normal, no improvement of cell function was found.

Diagram of experimental design

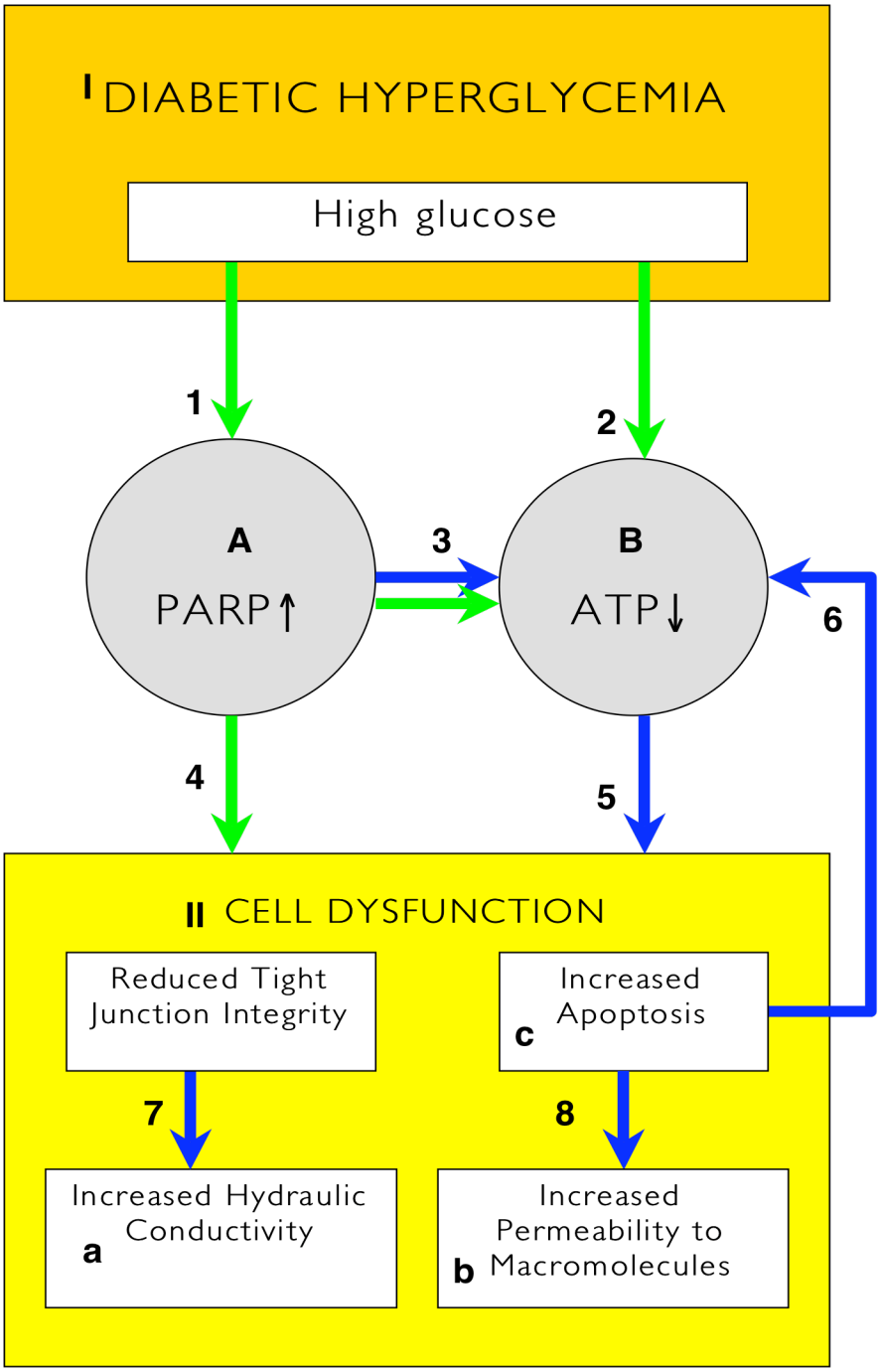

Figure 4.1) (Previous page) Schematic diagram of experimental design. The precondition I Diabetic Hyperglycemia has been determined to result in the end point condition II Cell Dysfunction. Pathways (1) and (2) cause the intermediate states (A) PARP upregulation, and (B) ATP depletion respectively. In addition, it is known that state (A) leads to state (B) by pathway (3) through the depletion of NAD+. Pathway (7) has been demonstrated for renal epithelial cells, and we will investigate it for BAEC in hyperglycemia using our transport model from Chapter 2). Pathway (8) has been investigated by (Huang et. al.), and pathway (6) by (REF), and will be further tested here in the high glucose precondition. The relative contributions of pathways (4) and (5) to condition II have not been fully quantified, by manipulation of states (A) and (B) will form the main focus of the current research.

Experimental Goals

To derive a baseline for our model, we measured five specific experimental outcomes in graded glucose (GG): ATP and PARP levels, apoptosis, hydraulic conductivity and convective diffusivity to solutes. In this control experiment, all 6 pathways are presumed to be active. Next, cells were cultured in normal glucose, blocking pathways 1 through 4, and were subjected to ATP depletion by chemical anoxia by exposure to antimycin-A (AA), activating pathways 4 and 5 in the absence of any effect of high glucose, and without activation of pathway 3. Application of a pan-caspase apoptosis inhibitor (CI) in graded glucose allowed us to record the functional state of cells with pathway 6 inactivated. And in a final series in graded glucose, the activity of PARP was reduced by the application of PJ34, a PARP inhibitor, allowing an analysis of the dependence no glucose activity, ATP levels, and PARP activation of pathways 3, 4 and 5.

Methods and Materials

Cell Culture Methods

Bovine Aortic Endothelial Cells (BAEC), (Vectec, cat. No.) from p4 to p7 were plated in Transwell® filters, with 0.4μm pores (Corning 3460) pre-treated with fibronectin for 1 hour. Seeding density was from 1/8 to 1/2 confluence (from 16 to 64 × 10^3 cells/cm2). Cell doubling time was determined to be approximately 36 hours, and independent of lot. Experimental preparations were cultured to confluence plus one day, (3 to 6 days) in MEM with Pen/Strep, L-glutamine, and 10% FBS, in four different media glucose concentrations, 5, 10, 20 and 30mM, in a cell culture incubator, 5% CO_2, balance air, at 37°C, in the dark. No correction for osmolarity was made in high glucose media. Media glucose content was measured with a blood glucose-monitoring device (One Touch Ultra Mini, Johnson & Johnson) and showed no change at as long as 15 days (although no experiments were conducted with day 15 cells). For continuity, these same filters were used for all of the following experiments and assays, even if permeability was not the experimental parameter. For the purpose of increasing the statistical sample, certain assays were repeated in a 96-well plate (Cat. No.), using the same cell culture protocol as above. For each experimental pathway investigated, age-matched cultures were prepared from the same cell lot, resulting in slightly different baseline values.

Apoptosis Assay

Three methods of measuring apoptosis were used, each measuring a different marker of apoptosis. For the annexin-V Apoptosis Detection Kit (Biovision K101-25), cells on filters were washed 3 times with PBS, then incubated with Annexin-FITC conjugate (100 μg/ml), for 5 minutes at room temperature. Detection was by fluorescence microscopy, and cells were counted and tabulated manually. Results were confirmed by 96-well assay using a plate reader. Terminal UDP Nick End Labelling (TUNEL) (Roche 11684817001) cells are fixed in 4% paraformaldehyde for 15 minutes, then permeabilized with methanol for 1 hour. Reagents were added according to the manufacturers instructions. Cells were counterstained with trypan blue for 45 seconds. Detection was by light microscopy (Nikon Eclipse TE2000-E). In the third method, trypan blue .04% was applied to experimental monolayers for 45 seconds, and then rinsed 3 times with PBS. Each assay was performed according to the manufacturers instructions for adherent cells with appropriate positive and negative controls.

Caspase Inhibitor

BAECs were seeded at 32K/cm^2, as described above, and cultured for 2 days to approximately half confluence. Caspase Inhibitor I, (CalBioChem 627610) a pan-caspase apoptosis inhibitor was then added to the luminal compartment of 8 experimental wells at 100μM. Cells were then cultured for an additional 2 days to confluence. Apoptosis assays were conducted as described in the previous section. Identical cell preparations were lysed for the ATP assay described below.

Protein Quantification

ATP concentration and PARP activity must both be normalized to protein content. A variation of the Bradford assay was used (Cayman cat. 0704002) according to the manufacturer's instructions as follows: cell lysates were placed in a 96 well plate at three serial dilutions. Coomasie dye was added to each well and absorption was detected at 595nm. Results were compared against a range of standards from 5 to 32 μg/ml. Dilutions in the range of 1:100 were used so that quantification could be made against the linear portion of the standard curve to avoid the saturating effect of detergent on the binding of the dye.

ATP Quantification

ATP was quantified by the luciferase/luciferin method (Molecular Probes cat. No. A22066). The reaction buffer was optimized to contain 1.0 μM luciferase, 0.5mM D-luciferin, and 1mM DTT, in the manufacturer's buffer. ATP standards were prepared from 1nM to 1μM. Lysates were prepared in 3 dilutions 1:2, 1:4, and 1:8. Concentration was calculated from the standard curve, and normalized to total protein content. Protein was quantified by the protocol above. ATP was quantified for graded glucose concentrations, both before and after permeability testing. Lysis was by the boiling water method of (Yang, Ho *et al.* 2002) as follows: media was removed from the filters and filter plates. Filter plates were placed over a boiling water bath just removed from the heating element. 1mL boiling deionised water was immediately added directly to the filters and incubated for 5 minutes. Filters were examined to determine that all cells had detached from the substrate.

PARP Quantification

For the PARP assay (Cat# 4671-096-K , Trevigen, Gaithersburg, MD), 50 µl of lysis buffer (by kit instructions) with 1.4mM protease inhibitor cocktail was added to each well, and incubated on ice for 15 minutes. Lysates were aliquotted and frozen at -80C for immediate use or use on the following day. Protein quantification was determined as above. Detection of PARP activity is defined per unit as follows: one unit of activated PARP is the amount required to incorporate 100 pmol of poly(ADP) from NAD into acid-insoluble form by binding to an immobilized histone substrate in 1 minute at 22°C The cell lysates were diluted in the kit buffer according to the manufacturers instructions so that the estimated activity fell in the range of standards, from .001 to 1 unit per 25µL. Then the PARP Cocktail, containing excess NAD+, is added to the cell lysates, standards, and negative control (without lysate or standard). Before detection, cells are washed 3× with PBS + 1% Triton-X 100, which is carefully removed. Cells are incubated for 20 minutes at room temperature with streptomycin conjugated to horseradish peroxidase (Strep-HRP), then washed as before. After incubation for 30 minutes in the dark with 50µL TACS-Sapphire®, absorption at 630 nm is monitored. After observable blue color appears, the reaction is stopped by the addition of 0.2 M HCl and absorption detected at 450nm.

PJ34 Protocol

PJ34 (Calbiochem, cat. No. 528150) was prepared according to manufacturers instructions, reconstituted in deionised water and stored in aliquots at -20 C. Two different concentrations 500 nM and 250 nM were added to experimental media at the

time of plating. Gross deformation in cell morphology and high rates of cell death at 500 nM precluded use of that concentration in our experiments.

Antimycin-A Protocol

BAECs were seeded at 32K/cm^2, as above and cultured for 4 days to confluence. On day 4 Antimycin-A was added to the luminal compartment of experimental wells for 20, 40, and 120 minutes respectively. Cells were then cultured for an additional 20 hours, and assayed for ATP content as above: lysis by boiling water method, lysates normalized for protein content by the Bradford assay, and ATP quantified by the luciferase/luciferin method. ATP levels were found to recover to those comparable to that seen in 10, 20, and 30mM glucose media culture, respectively.

Water and solute flux

BAEC cultured as above are placed in a pressure flow apparatus as described in Chapter 3). Bubble displacement is converted to *Jv* by the sealing model described in Chapter 2). Volume flow per unit area is calculated as a function of time, and the sealing protein diffusivity and sealing potential are extracted from the data.

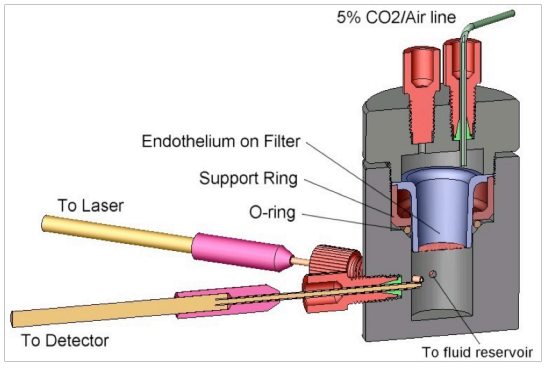

Figure 4.2) Diagram of pressure-flow chamber showing the fluorescent detection system, and a sectional view of the interior of the chamber.

A fluorescent detection system allows measurement of fluorescent-conjugated solutes. Fluorescence accumulation in the basolateral chamber is measured by recording the emission of the label after excitation by a 543.5 nm laser beam which is directed into the basolateral chamber through a system of 2 silica optical fibers as shown in Figure (2.4). The emission silica fiber is coupled to a model D48 photomultiplier from C&L Instruments (Hummelstown, PA). A Windows-based software program (FluorMeasure) and model PC-DAQ control card from C&L Instruments are used for data acquisition and control of the photomultiplier. After a calibration of known solute concentration to fluorescence intensity is made, the effective permeability P_e can be calculated by equation (30).

(30)

$$P_e = \frac{(\Delta C_b / \Delta t) \times V_b}{C_a \times A}$$

where $\Delta C_b/\Delta t$ is the average change in basolateral solute concentration over 5 min, V_b is the fluid volume of the basolateral chamber, and C_a is the apical concentration of the solute, and A is the area of the filter(Noll, Muhs *et al.* 1995; Wysolmerski and Lagunoff 1988). For experiments in the convection of water alone, cells are allowed to equilibriate with experimental media for 1 hour, then a pressure drop across the monolayer is applied by lowering the distal reservoir by 10cm. After 1 hour, the 10-cmH_2O pressure gradient is removed. For diffusion/convection experiments, before the start of the experiments, the filters were rinsed twice with experimental medium (1% BSA-PF) and 10 g/ml DiI-LDL. Fluorescence is recorded during the entire 2 hours of equilibration and convection,

and then for an additional 60 minutes after pressure is removed. To measure the volumetric flow rate per unit area (Jv/A), the bubble is tracked with a photometer, which follows the air-liquid interface as the bubble moves through the tube. The digitized signal is recorded as position and time. The entire apparatus is maintained at 37°C and the pH of the media at 7.4 by the influx of 5% CO_2 balance air into the apical chamber and distal reservoir.

Statistics

Values are reported as mean ± SEM. Significance was determined by analysis of variance (ANOVA) of the experimental variable against the four level factor glucose concentrations and the two level factor for treatment (control graded glucose vs. PJ34, antimycin-A, or caspase inhibitor). Where significance was indicated by ANOVA, analysis of covariance (ANCOVA) was used to determine if a significant correlation exists for a least-squares regression of the experimental variable against glucose concentration. In the case of $J_V(t)$, a Tukey-Kramer multiple comparisons test was performed on J_V at 5-minute intervals. The Tukey-Kramer test is a variation of the student's t test-to-test data samples in which the mean varies significantly in discrete ranges within the entire data set. The test allows the interval of comparison between samples to be specified by the user. It is useful in our case for the sealing data in that data from discrete time periods (i.e. early vs. late, sealing vs. steady) may be significant from the mean of some time periods, but not from the mean of other time periods, or from the mean of the entire data set. Significance was determined by $p < 0.05$. The

Pearson's correlation coefficient (*r)* between experimental treatments at each glucose level was also calculated. Where studentized ranges are significant, the p value is stated alone in parentheses. Where the correlation coefficient and linear regression were significant for the data series as a whole, the p value is given with *r* in parentheses. Since multiple series of experiments were performed, some experimental variations in baseline values are reported, but are not statistically different from each other by students t test. Where presentation of different values for the same experiment was not necessary for clarity of presentation within an experiment, values are presented as normalized against control.

Results

Baseline with all pathways functioning: Effect of hyperglycemia on ATP, PARP, apopotosis, and cell function

In Figure (4.3) the data from a relative quantification of mitochondrial superoxide production is presented, showing a linear increase with glucose concentration. The linear increase is significant ($p < 0.05$, $n > 9$ for each concentration).

Figure (4.4) shows that PARP activity increased in high glucose. PARP activation, as measured in nmol NAD+ per μg protein per minute, increased from 148.08 ± 16.78, at 5mM glucose to 260.5 ± 22.72 at 30mM glucose. The increase was linear in glucose ($r = 0.85$).

Figure (4.5) shows the effect of media glucose concentration on ATP levels. With increasing glucose, resting ATP levels dropped significantly from 15.6 ± 1.4

nmol/mg·protein at 5mM glucose to 7.1 ± 1.7 nmol/mg·protein at 30mM glucose ($p < 1 \times 10^{-5}$). The correlation coefficient between ATP and glucose concentration is -0.95.

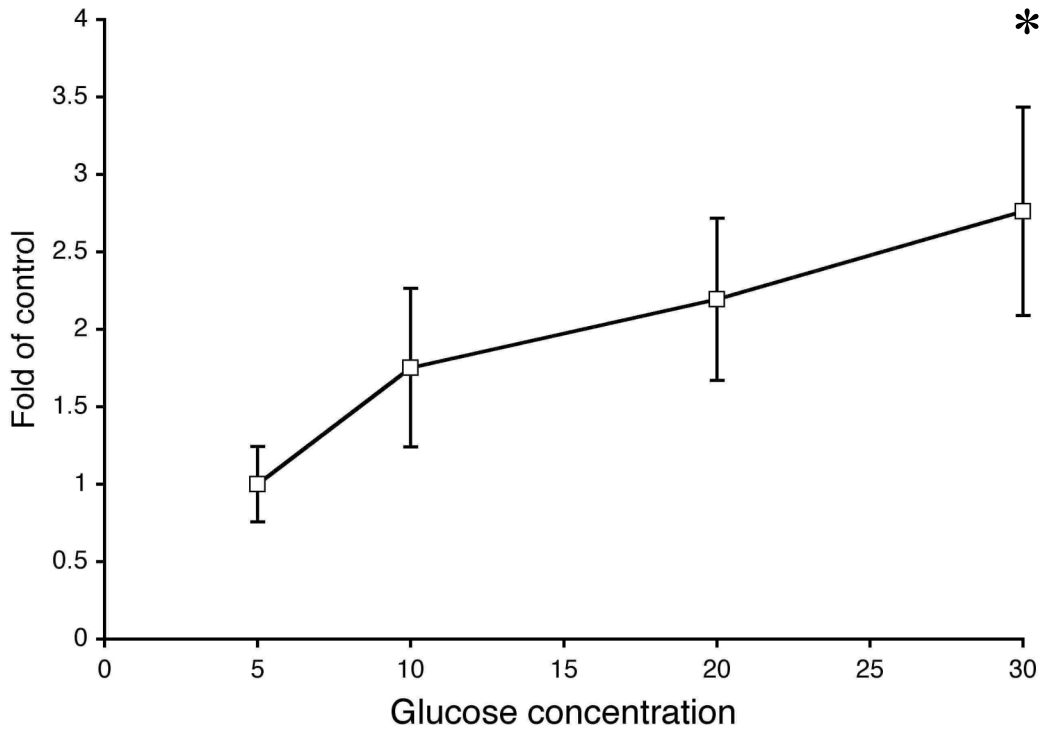

Figure 4.3) Mitochondrial superoxide production in graded glucose. BAEC were cultured for 4 days (confluence plus one day) on fibronectin coated polycarbonate filters in differential glucose media of 5, 10, 20, and 30 mM glucose. Superoxide production was measured by detection (at 580 nm) of MitoSOX®, a live cell permeant fluorogenic dye, that is highly selective for detection of superoxide. Arbitrary units of fluorescence are presented normalized to 5mM glucose results.

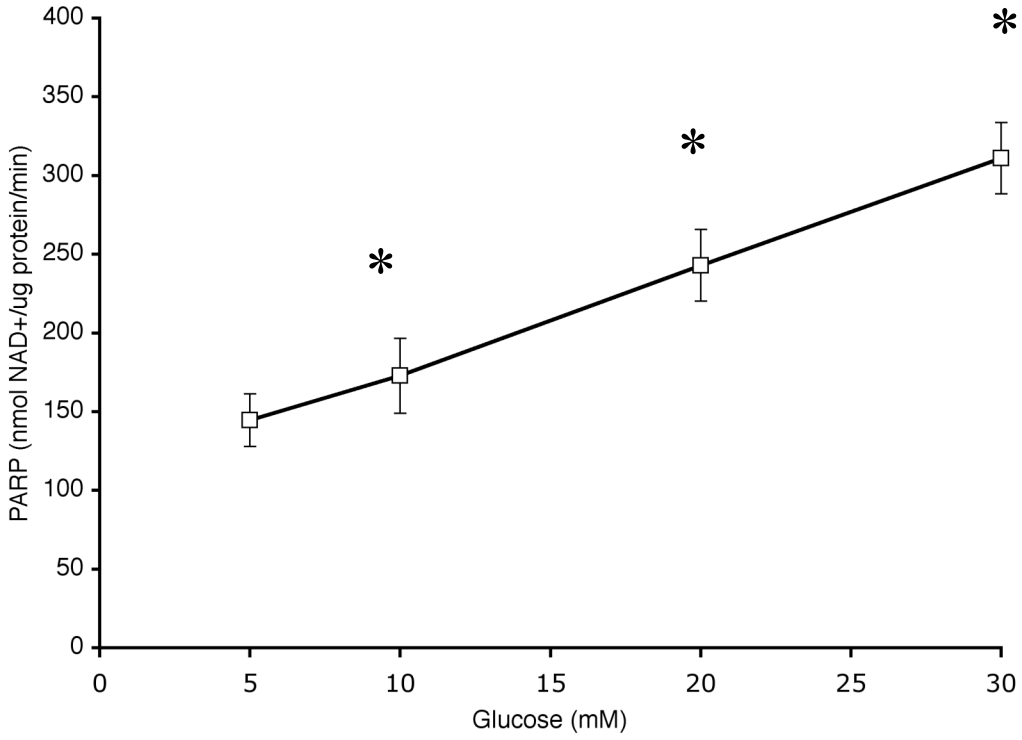

Figure 4.4) PARP as a function of glucose concentration. BAEC were cultured for 4 days (confluence plus one day) on fibronectin coated polycarbonate filters in differential glucose media of 5, 10, 20, and 30 mM glucose. PARP activity was detected by colorimetric assay (Trevigen). PARP activity is quantified by its ability to incorporate poly(ADP) from NAD into acid-insoluble form by binding to an immobilized histone substrate as a function of time. Units are expressed in nmol of NAD+ immobilized per µg protein per minute. PARP activity increased in 30mM glucose relative to 5mM glucose by 115.2 ± 15.3%. The increase in PARP with increasing glucose is significant by students t test at each hyperglycemic condition ($p < 0.001$). Linear regression of PARP activity as a function of increasing glucose is also highly significant ($r = 1.0$ $p < 0.001$).

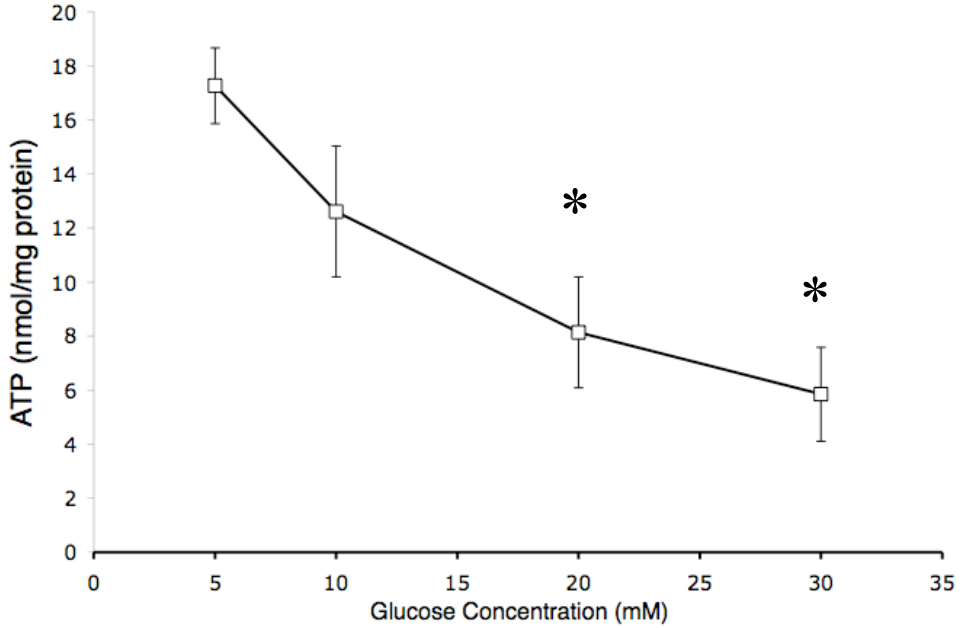

Figure 4.5) ATP as a function of glucose concentration. BAEC were grown for 3 to 4 days (confluence plus one day) on fibronectin coated polycarbonate filters in differential glucose media of 5, 10, 20, and 30 mM glucose. ATP was measured by the luciferase assay and quantified against ATP standards. ATP reduction in hyperglycemia is significant by students t test against normal glucose at 20mM (52.8%) and 30mM (66.1%) ($p < 0.001$). ATP concentration is highly negatively correlated with glucose concentration, and the linear regression of decreasing ATP with increasing glucose concentration is significant for the entire series ($r = -0.95$, $p < 0.001$). Results for $n > 6$ for each concentration.

Figure (4.6a) shows the sealing effect for GG monolayers. All high glucose samples had higher average values than normal glucose at every time point. Significant reduction in flow was seen for all glucose concentrations for each 5 minute interval for the first 30 minutes when compared against initial flow.

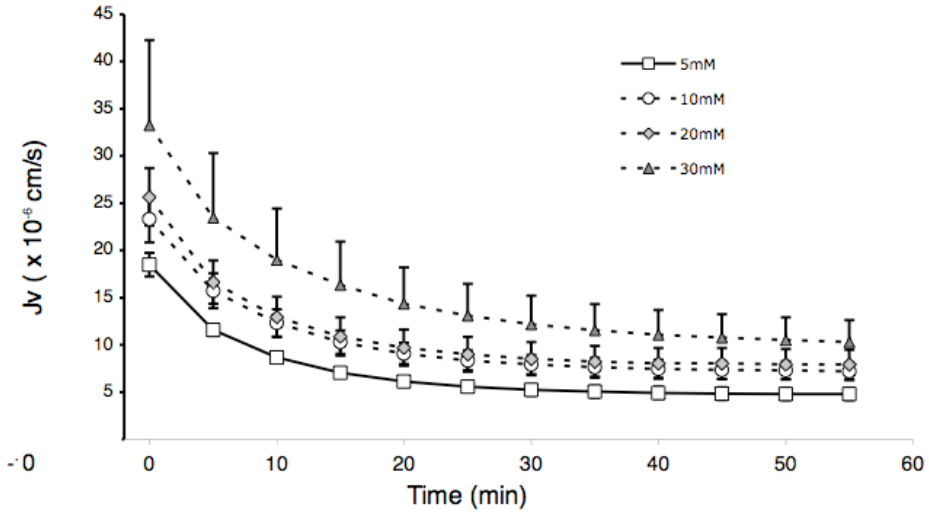

Figure 4.6 a) Volume flow rates ($J_V(t)$) in graded glucose. BAEC were grown for 3 to 4 days (confluence plus one day) on fibronectin coated polycarbonate filters in differential glucose media of 5, 10, 20, and 30 mM glucose. Filters were placed in a pressure-flow apparatus and subjected to a 10 cm H_2O transmural pressure gradient for 1 hour. Flow through the monolayer was monitored by the tracking of the position of a bubble in a glass tube downstream from the filter. Position-time data was converted to volume flow rate using the sealing transport model from Chapter 2). The sealing effect showed a reduced diffusivity at 10mM glucose only (p = 0.02). Sealing potential was not statistically significant between treatments.

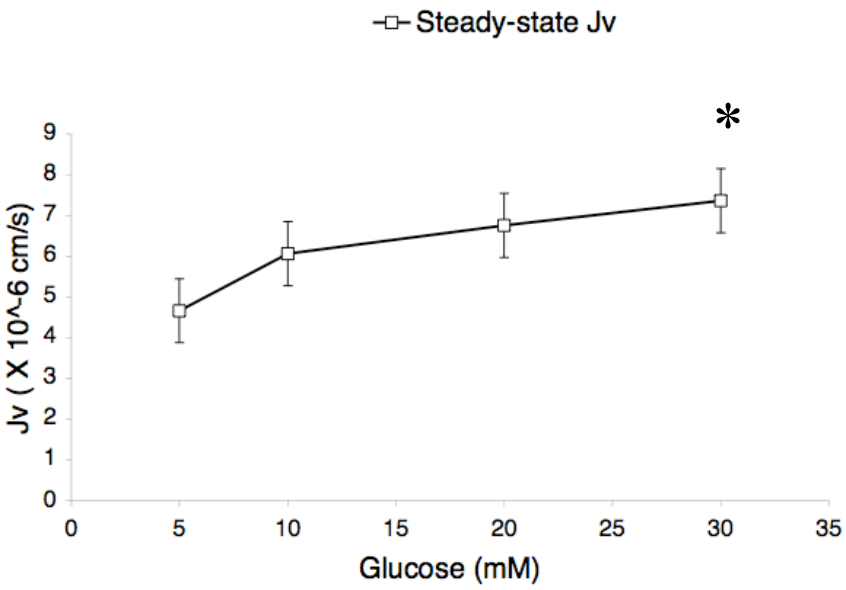

Figure 4.6 b) $J_{V\infty}$ vs. glucose values extracted from the experiments shown in a). $J_{V\infty}$ increased significantly (158.0 ± 12.8 % of control) at 30mM glucose. $J_{V\infty}$ was moderately correlated with increasing glucose, and linear regression of $J_{V\infty}$ *against* glucose concentration was highly significant (r = 0.47, p = 0.001).

$J_{V\infty}$ increased monotonically with increasing glucose concentration ($r = 0.4696$). The sealing potential and diffusivity were not significantly different in higher glucose, nor did they show a linear relationship to increasing glucose concentration. Results are shown in table (4.1).

Graded glucose (GG)	*Diffusivity ($\times 10^{-8}$ $cm^2 \cdot s^{-1}$)*	*Jv_∞ ($\times 10^{-6}$ $cm \cdot s^{-1}$)*	*Sealing potential $(1+\gamma)^{-1}$*
5mM Glucose	2.378 ± 0.183	4.6573 ± 0.7153	0.08854 ± 0.0419
10mM Glucose	1.766 ± 0.304 *	6.0573 ± 1.1862	0.07251 ± 0.0152
20mM Glucose	2.443 ± 0.255	6.7523 ± 1.0529	0.06671 ± 0.0133
30mM Glucose	2.260 ± 0.311	7.3553 ± 1.1081	0.1008 ± 0.0201
r	0.02382	0.4696	0.3080
Linear model p value	0.7621	0.001442 †	0.06296

** p value < 0.05 vs. control 5mM glucose by ANOVA*
† p value < 0.001 of linear regression

Table 4.1) Diffusivity, steady-state flux, and sealing potential in graded glucose. Fitted parameters for 20 experiments (n = 5 for each glucose concentration). Correlation coefficient *r* is of the dependent variable against glucose. P values are for a least squares fit of a linear regression model of the dependent variable against glucose. The only significant linear relationship is between $J_{V\infty}$ and glucose. ANOVA is of dependent variable against the four level factor experimental glucose treatment.

Figure (4.7) shows the results of ATP levels measured before and after transport experiments for 5mM and 30mM glucose, showing a drop in ATP of 29.1 ± 5.7% for normal, and 61.4 ± 2.3% for hyperglycemic cells (n = 12, $p < 0.001$).

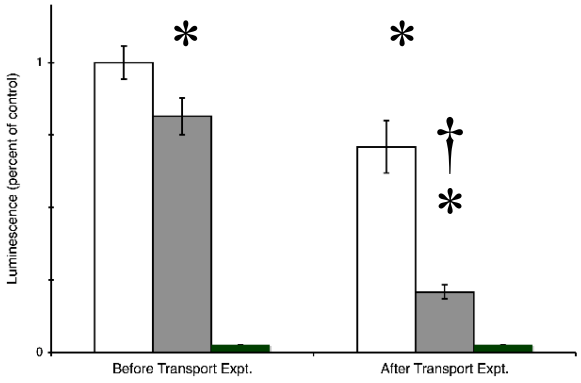

Figure 4.7) ATP depletion after transport experiment. BAEC, grown to confluence on polycarbonate filters in differential glucose media of 5, 10, 20, and 30 mM glucose. Filters were placed in a pressure-flow apparatus and subjected to a 10 cm H_2O transmural pressure gradient for 1 hour. ATP quantification was by the luciferase assay. * ($p < 0.05$ against 5 mM before sealing) †($p < 0.05$ against 30mM after sealing)

The number of apoptotic cells increased linearly with increasing glucose concentration as shown in Figure (4.8). The increase is significant at every point ($p < 0.001$, n = 12 for each concentration); standard error bars shown are smaller than the chart marker.

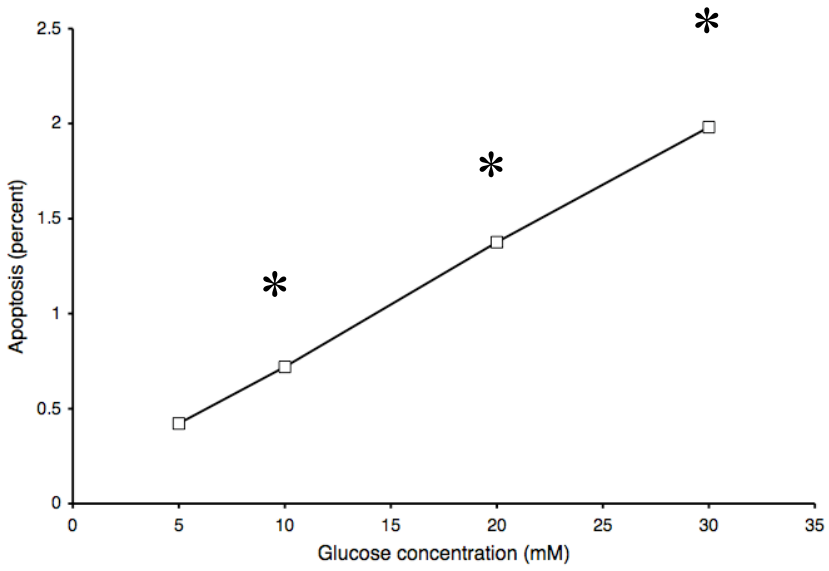

Figure 4.8) Apoptosis in graded glucose. BAEC, grown to confluence on polycarbonate filters in differential glucose media of 5, 10, 20, and 30 mM glucose. Apoptosis was measured by annexin conjugate, TUNEL assay and trypan blue exclusion, results are in close agreement. Increase is linear in glucose concentration ($p < 0.001$)

Permeability of the endothelium to solutes (70 kD dextran) also was increased, but not linearly in glucose concentration. Convective permeability to 70 kD dextran increased from $1.81 \times 10^{-6} \pm 0.7 \times 10^{-6}$ cm/s at 5mM glucose to $3.14 \times 10^{-6} \pm 0.5 \times 10^{-6}$ cm/s at 10mM glucose, but was not quite significantly different ($p = 0.8$). Convective permeability to dextran dropped sharply at 30mM to the order of 10^{-7} cm/s. (Data not shown.)

Figure (4.9) shows the increase in a) convective permeability, and b) diffusive permeability to LDL in graded glucose.

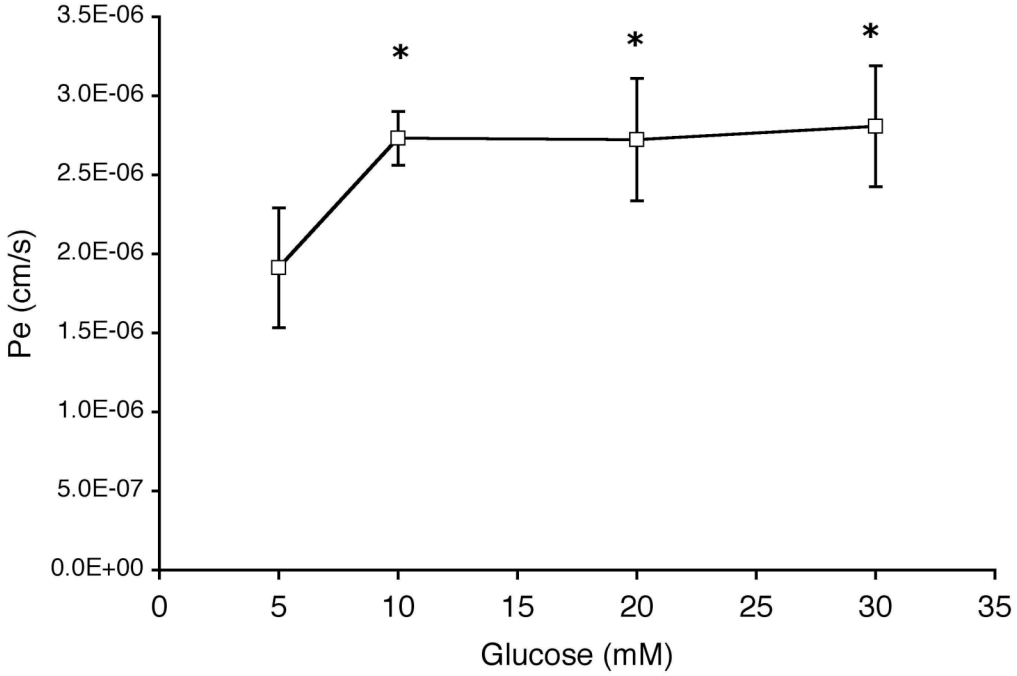

Figure 4.9) Transport of LDL in graded glucose. BAEC were grown for 4 days (confluence plus one day) on fibronectin coated polycarbonate filters in differential glucose media of 5, 10, 20, and 30 mM glucose. Filters were placed in the pressure-flow apparatus with 10µg/ml DiI-LDL added to the luminal compartment and allowed to equilibrate for 1 hour. Solute flux was calculated against fluorescence of a standard DiI-LDL of known concentration. a) After 1 hour, the filters were subjected to a 10 cm H_2O transmural pressure gradient for 1 hour. Fluorescence readings were taken during the entire process, and the rate of change converted to solute flux as described in the text. Convective permeability showed an increase with glucose from 2.36 ± 0.37 × 10^{-6} cm/s at 5 mM, to 6.01 ± 1.97 10^{-6} cm/s at 10mM glucose ($p = 0.03$). Convective permeability to LDL did not increase significantly beyond the level of 10 mM for 20 mM or 30 mM. Linear regression for the entire experimental sample against glucose was highly significant ($r = 0.97$ $p < 0.001$).

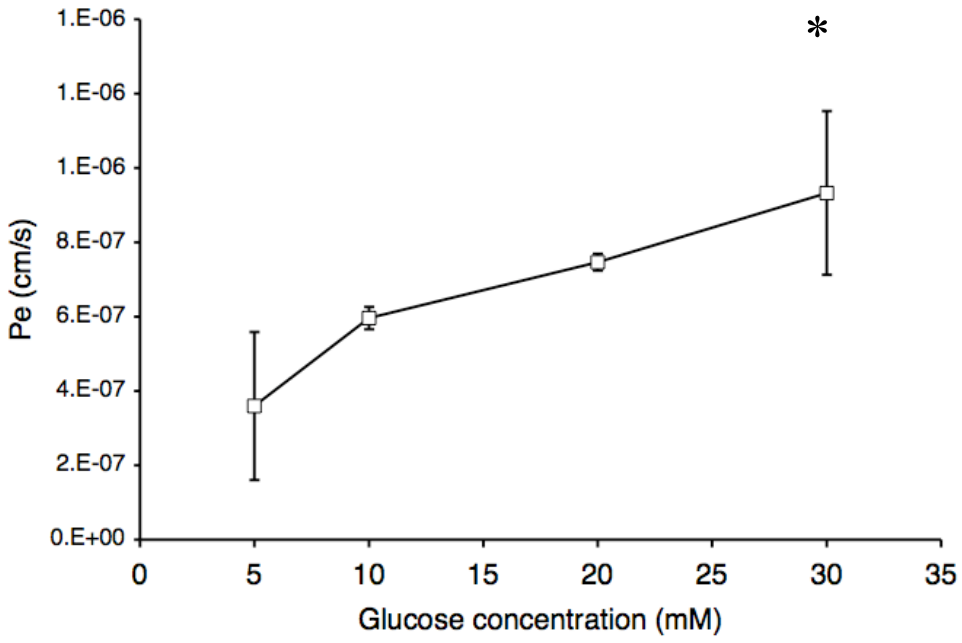

4.9b) After 1 hour, pressure was removed and diffusive flux was recorded for another hour after. Diffusive flux showed a linear increase with glucose, from 3.59 ± 0.30 × 10^{-7} cm/s at 5 mM, to 9.32 ± 2.20 10^{-7} cm/s at 30mM glucose ($p = 0.03$) and was significantly at 30mM glucose ($p = 0.01$). Linear regression of all data was significant ($r = 0.97$, $p = 0.001$).

Pathway 6: Depletion of ATP by apoptosis

It is possible that there is a feedback loop, shown by pathway 6 on the experimental design. The observed ATP depletion could be the result of excessive ATP consumption by the increasing number of apoptotic cells. To quantify the contribution of apoptotic ATP consumption to ATP depletion, we measured ATP depletion in the presence of a pan-caspase inhibitor, shown to be a potent blocker of apoptosis. In Figure (4.9) we see no difference in ATP levels for control or for glucose concentrations above 10mM. However, at 10mM, ATP levels showed a significant increase in the presence of the apoptosis inhibitor.

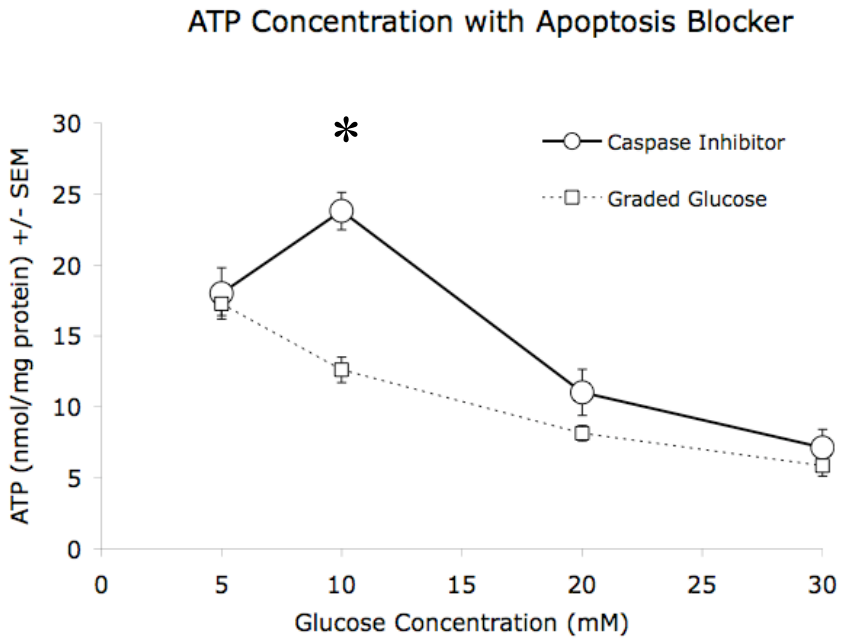

Figure 4.10) Effect of caspase inhibitor on ATP levels. BAEC were grown for 3 to 4 days (confluence plus one day) on fibronectin coated polycarbonate filters in differential glucose media of 5, 10, 20, and 30 mM glucose. Caspase inhibitor (3 µM) was added to the media 2 days before confluence. ATP quantification on confluence plus one day was by the luciferase assay. ATP levels at 10mM glucose were significantly higher than control ($p < 0.05$). CI experimental ATP levels at 5, 20, and 30mM glucose were not significantly different from GG experiments ($p > 0.10$)

Pathway 4: Effect of ATP depletion at normal levels of PARP activation

BAEC monolayers grown at 5mM glucose, with normal PARP activity, were exposed to antimycin-A for increasing time periods, and then allowed to recover for 24 hours, and ATP was measured as described above. Figure 4.11a) shows the results. Exposure for 0, 15, 30, and 60 minutes resulted in ATP levels equivalent to those found in 5, 10, 20, and 30mM glucose respectively. Data is presented as nmol(ATP)/μg protein and glucose equivalent.

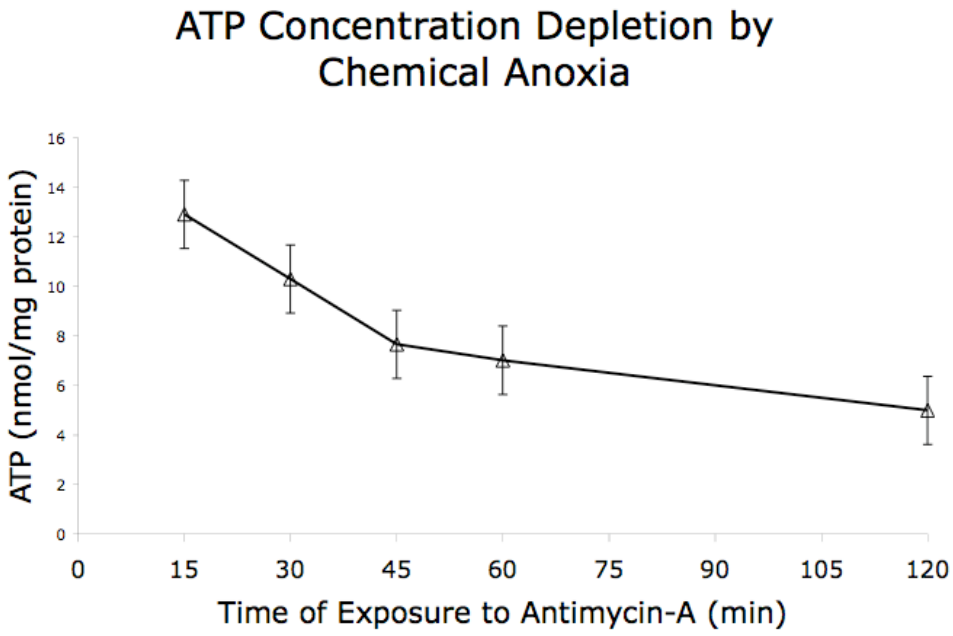

Figure 4.11 a) ATP depletion by antimycin-A. BAEC were grown for 3 days, to confluence, on fibronectin coated polycarbonate filters in differential glucose media of 5, 10, 20, and 30 mM glucose. Filters were exposed to antimycin-A (2µM) for 0, 20, 40, and 120 minutes, then the media was changed and monolayers allowed to recover for 24 hours. ATP quantification was by the luciferase assay. Significant depletion of ATP was seen at each time of exposure ($p < 0.05$). The known concentrations of ATP for 10, 20, and 30mM glucose were determined by linear interpolation to correspond to AA exposure times of 15, 30, and 45 minutes respectively.

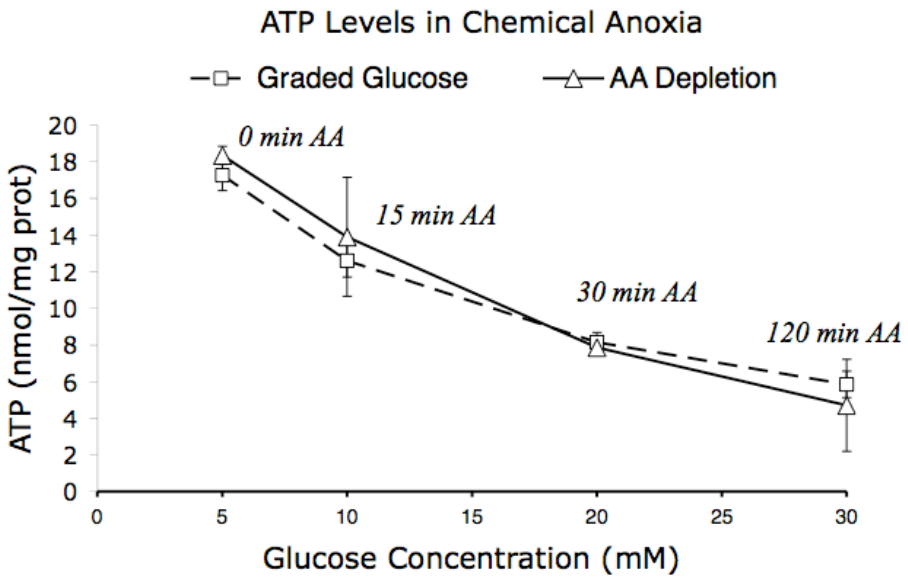

4.11 b) Samples prepared as above were exposed to AA for the calculated times. ATP levels were the same for AA ATP-equivalent treatments and the graded glucose concentration ($r = 1$, $p < 0.001$).

D, $J_{V\infty}$, and sealing potential were evaluated for AA depleted monolayers. $J_{V\infty}$ in AA is correlated with $J_{V\infty}$ in graded glucose. In Figure (4.11a), the sealing curves for each exposure time to antimycin-A are shown; although the sealing effect was reduced, the curves followed a trend of increased water flux for increased ATP depletion Figure (4.11b) shows that $J_{V\infty}$ increased with increasing exposure to antimycin-A. Table (4.2) shows that diffusivity was significantly reduced at every ATP depletion level relative to control. And sealing potential was slightly higher at higher effective glucose concentrations with AA.

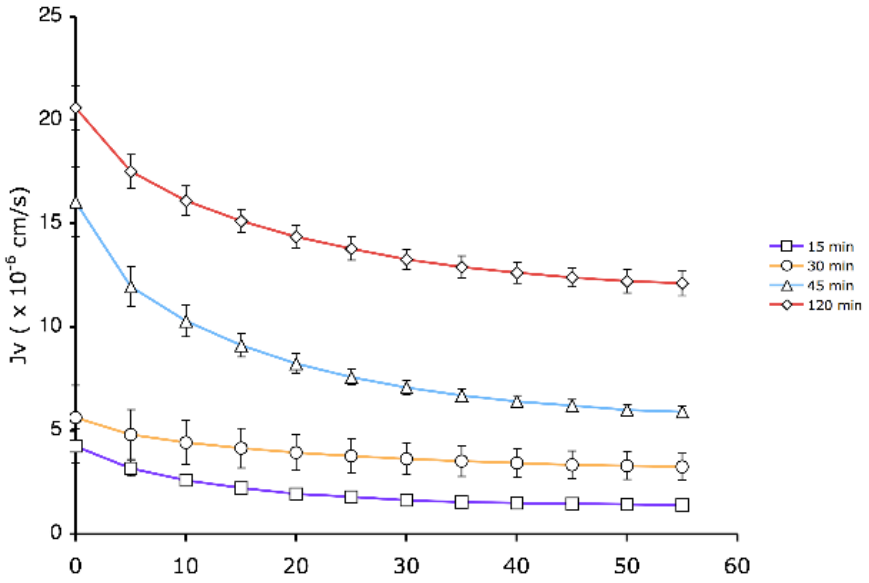

Figure 4.12 a) Sealing effect in antimycin-A (AA) ATP depleted monolayers. BAEC were grown for 3 days, to confluence, on fibronectin coated polycarbonate filters were exposed to antimycin-A (2µM) for 0 (no antimycin-A), 15, 30, and 120 minutes, then the media was changed and monolayers allowed to recover for 24 hours. Filters were placed in a pressure-flow apparatus and subjected to a 10 cm H_2O transmural pressure gradient for 1 hour. Flow through the monolayer was monitored by the tracking of the position of a bubble in a glass tube downstream from the filter. Position-time data was converted to volume flow rate using the sealing transport model from Chapter 2). The sealing effect showed a reduced diffusivity at for all AA exposure times ($p < 0.02$). Sealing potential was significantly higher for 30 (20mM ATP-equivalent) and 120 min (30mM ATP-equivalent) exposure times ($p < 0.05$).

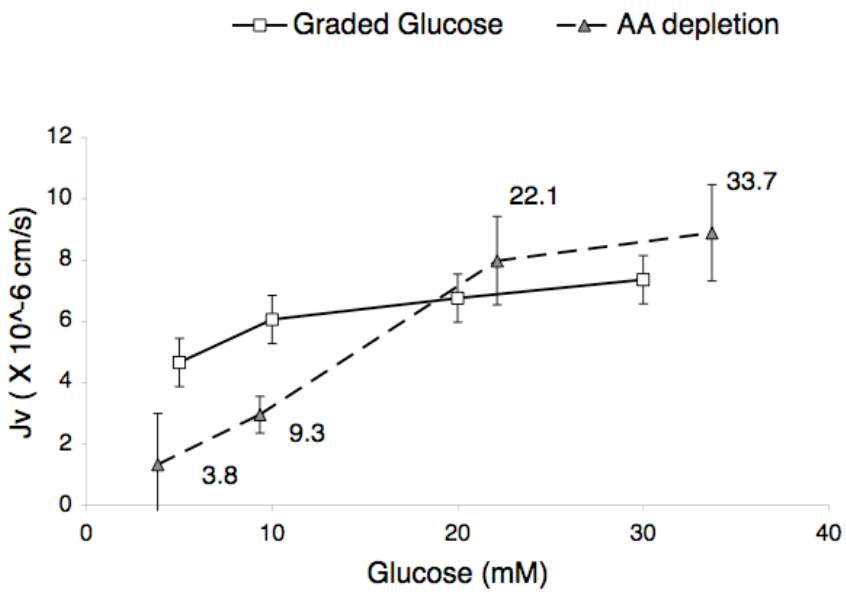

4.12b) $J_{V\infty}$ was not significantly different between AA treatments (shaded triangles) and GG (open squares). AA labels are the glucose concentration corresponding to the equivalent AA depletion (ATP-equivalent) level by linear interpolation. $J_{V\infty}$ for AA ATP-equivalents are similar to GG treatments (r = 0.52, p = 0.001) (n = 16).

(Glucose equiv.) ATP (nmol/μg)		*Diffusivity* ($\times 10^{-8}$ $cm^2 \cdot s^{-1}$)	$J_{V\infty}$ ($\times 10^{-6}$ $cm \cdot s^{-11}$)	*Sealing potential* $(1+\gamma)^{-1}$
(5mM)	18.35	1.8400 ± 0.0687	1.32255 ± 0.01665	0.09429 ± 0.0313
(10mM)	12.9	0.8280 ± 0.0910 *†	2.94975 ± 0.6012	0.07258 ± 0.0190
(20mM)	7.65	1.0536 ± 0.0881 *†	7.9758 ± 2.889	0.2775 ± 0.00899
(30mM)	4.99	1.2066 ± 0.1230 *†	8.8829 ± 3.146	0.3306 ± 0.03292
	r	0.5967	0.9354	-0.5480
	p value	0.006*	0.331	0.078

** p value < 0.01 for analysis of variance against control 5mM glucose*
† p value < 0.05 vs. 18.35 nmol/μg ATP

Table 4.2) Diffusivity, steady-state flux, and sealing potential in AA depletion. Fitted parameters for 20 experiments (n = 5 for each antimycin-A exposure time). Correlation coefficient *r* is of antimycin-A against equivalent glucose concentration. P values are for students t test against equivalent glucose concentration. Diffusivity is significantly reduced in antimycin-A depletion. $J_{V\infty}$ is highly correlated to equivalent glucose concentration.

Relative contribution of pathways 4 and 5: Independent ATP depletion and PARP activation in normal glucose.

To quantify the effect of PARP activation on cell dysfunction, cells grown in graded glucose were incubated with the potent PARP inhibitor PJ34. The effect was to reduce PARP activity by 37.1 ± 10.0 % at 5mM, 45.1 ± 10.1 % at 10mM, 44.1 ± 7.2 % at 20mM, and 41.4 ± 5.1 at 30mM, and to restore ATP levels (in nmol/μg protein) by 3.8 ± 1.1 at 5 mM, 8.0 ± 1.6 at 10 mM, 6.3 ± 1.4 at 20 mM and 5.9 ± 1.4 at 30 mM. Blocking of PARP activity was linear in dosage of PJ34 (data not shown). Table (4.3) shows the results for PARP activity and ATP levels for monolayers treated with 250nM PJ34

against control monolayers in graded glucose. PJ34 reduced the percentage of PARP by an average of 42% and increased ATP by an average of 6 nmol/μg protein.

Glucose Concentration	*PARP activity (control)* *(pmol/min/mg protein)*	*PARP activity (with PJ34)* *(pmol/min/mg protein)*	*Percent change*	*p value of change*
5mM	144.5 ± 16.8	93.17 ± 31.3	-35.5 ± 10.0	< 0.001*
10mM	172.8 ± 23.7	108.6 ± 37.5	-37.1 ± 10.1	0.046*
20mM	242.9 ± 22.7	150.0 ± 37.5	-38.3 ± 7.2	0.005*
30mM	311.0 ± 22.7	223.0 ± 37.5	-28.3 ± 5.1	< 0.001*
r to Glucose	1.0	1.0		
r to Control			1.0	

Glucose Concentration	*ATP level (control)* *(nmol/μg)*	*ATP level (with PJ34)* *(nmol/μg)*	*Percent change*	*p value*
5mM	17.26 ± 1.4003	21.07 ± 2.0499	+ 22.1 ± 0.1	0.05*
10mM	12.61 ± 2.4254	20.57 ± 2.2035	+ 63.2 ± 1.6	0.003*
20mM	8.136 ± 2.0499	14.47 ± 2.0499	+ 77.2 ± 1.4	0.002*
30mM	5.846 ± 1.734	11.76 ± 2.4825	+ 101.2 ± 1.4	0.002*
r to Glucose	-0.96	-0.98		
r to Control			1.0	

Table 4.3) PARP activity in graded glucose compared to PARP activity in the presence of PJ34 (n > 10 for each glucose concentration and treatment). Correlation coefficient *r* is of the dependent variable against glucose. P values are for students t test of PJ34 treated cultures against the equivalent glucose concentration without.

Although PJ34 muted the rise of PARP and the drop in ATP levels, it did not have a significant effect on $J_{V\infty}$ or sealing potential. A significant drop in diffusivity was found, both from control normal glucose monolayers, and also from parallel glucose concentrations, as can be seen from Tables (4.1) and (4.4). The trend of increasing permeability with increasing glucose was similar, but slightly higher in each case.

with PJ34	*Diffusivity (× 10-8cm· s-1)*	*Jv∞ (× 10-6 cm· s-1)*	*Sealing potential (1 + γ)-1*
5mM	*2.637 ± 0.23*	*3.8757 ± 1.3059*	*0.08673 ± 0.0222*
10mM	*1.339 ± 0.29* †	*7.0847 ± 1.8698*	*0.09272 ± 0.0356*
20mM	*1.575 ± 0.23** †*	*7.6804 ± 1.7027*	*0.09792 ± 0.0360*
30mM	*1.805 ± 0.31* †	*8.6978 ± 1.8213*	*0.10013 ± 0.0411*

** p value < 0.05 vs. control at equivalent glucose concentration by students t test*
*** p value < 0.001 vs. . control at equivalent glucose concentration by students t test*
† p value < 0.05 vs. control at 5mM glucose

Table 4.4) Model parameters in GG with PJ34.

No significant effect of PJ34 on $J_{V\infty}$ relative to control was found. $J_{V\infty}$ is plotted against graded glucose for control, and PJ34 treatments in Figure (4.13).

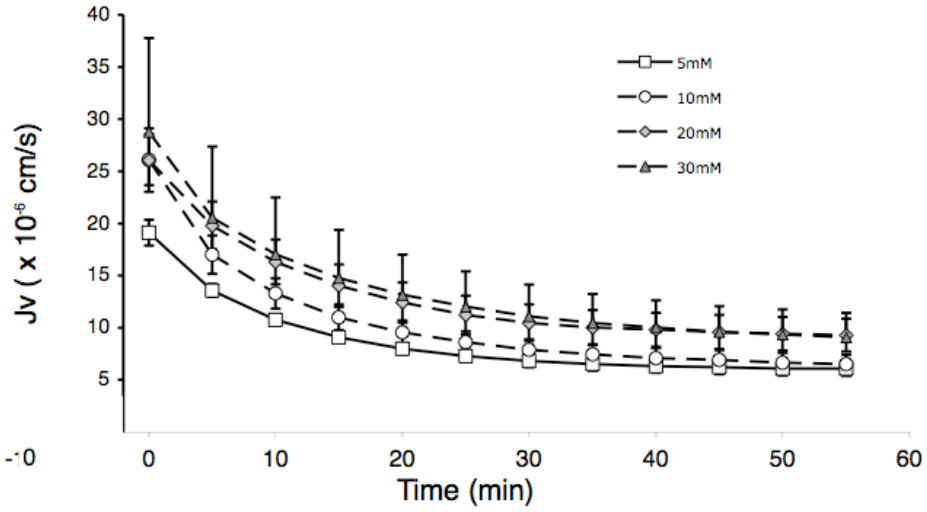

Figure 4.13 a) $J_V(t)$ for graded glucose with PJ34. BAEC were grown for 3 to 4 days (confluence plus one day) on fibronectin coated polycarbonate filters in differential glucose media of 5, 10, 20, and 30 mM glucose containing 250nM PJ34. Filters were placed in a pressure-flow apparatus and subjected to a 10 cm H_2O transmural pressure gradient for 1 hour. Flow through the monolayer was monitored by the tracking of the position of a bubble in a glass tube downstream from the filter. Position-time data was converted to volume flow rate using the sealing transport model from Chapter 2). The sealing effect showed a reduced diffusivity at 10mM, 20mM and 30mM glucose in the presence of PJ34 (p = 0.001). Sealing potential was not statistically significant between treatments.

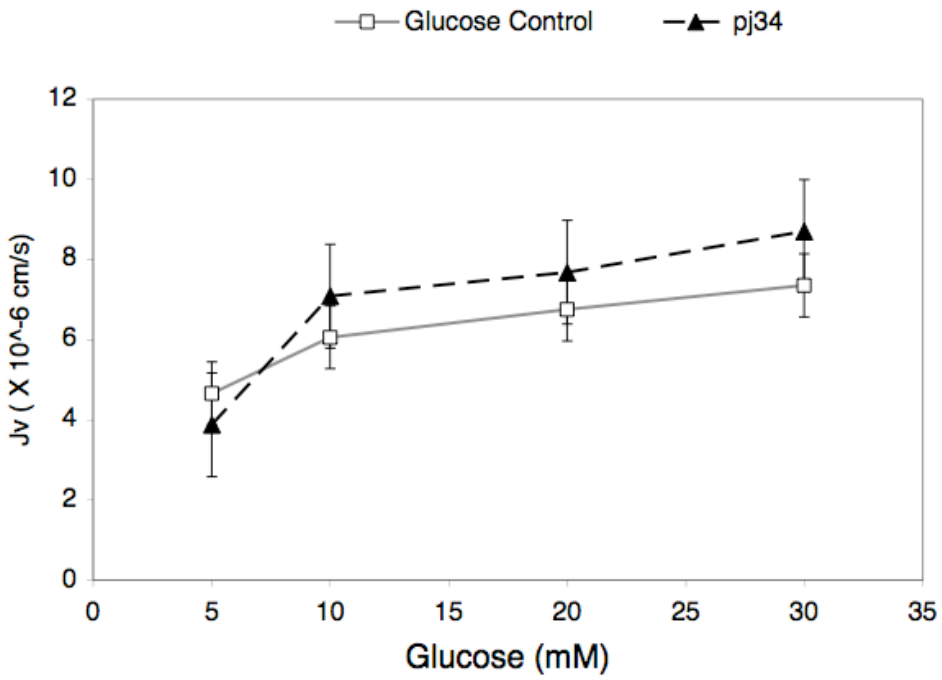

4.13b) $J_{V\infty}$ for graded glucose control (open squares) or graded glucose with PJ34 (shaded triangles). $J_{V\infty}$ at each concentration of glucose showed no statistical difference to $J_{V\infty}$ in graded glucose alone ($p > 0.20$). As in 30mM glucose without PJ34, $J_{V\infty}$ increased significantly (186.7 ± 22.8 % of control) at 30mM glucose with PJ34.

In Figure (4.15) we plot ATP against PARP, in graded glucose with and without PJ34, and show that reducing the percentage of PARP activity reduces the amount of ATP depletion. ATP levels were strictly correlated to PARP activity as shown. Results are plotted with error bars ± standard error of the mean in both ATP level and PARP activity, along with a least squares best fit of an exponential decay of ATP vs PARP. The correlation between treatments is highly significant ($r = 1$, $p < 0.001$).

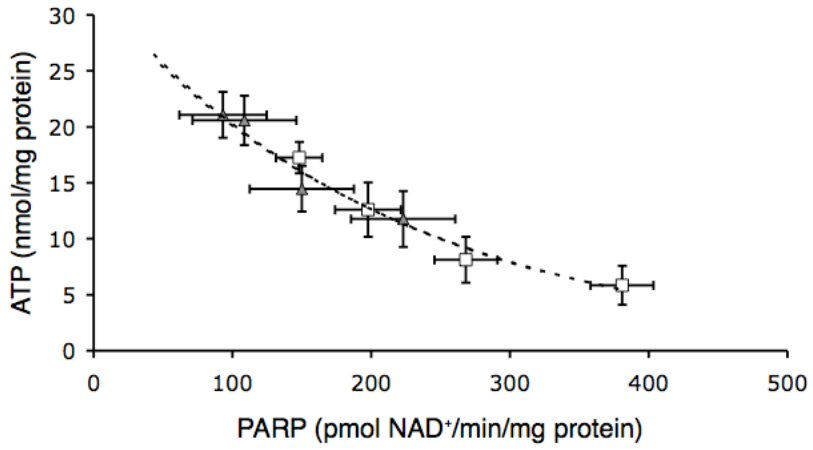

Figure 4.14) ATP level plotted against PARP activity. Data from experiment measuring ATP as a function of glucose and PARP as a function of glucose were plotted against each other. Error bars in each dimension are ± standard error of the mean of each variable.

Figure (4.15) plots $J_{V\infty}$ against ATP levels in each experimental preparation, graded glucose, PARP inhibition, and ATP depletion by antimycin-A. Each series shows an increase in $J_{V\infty}$ for lower levels of ATP.

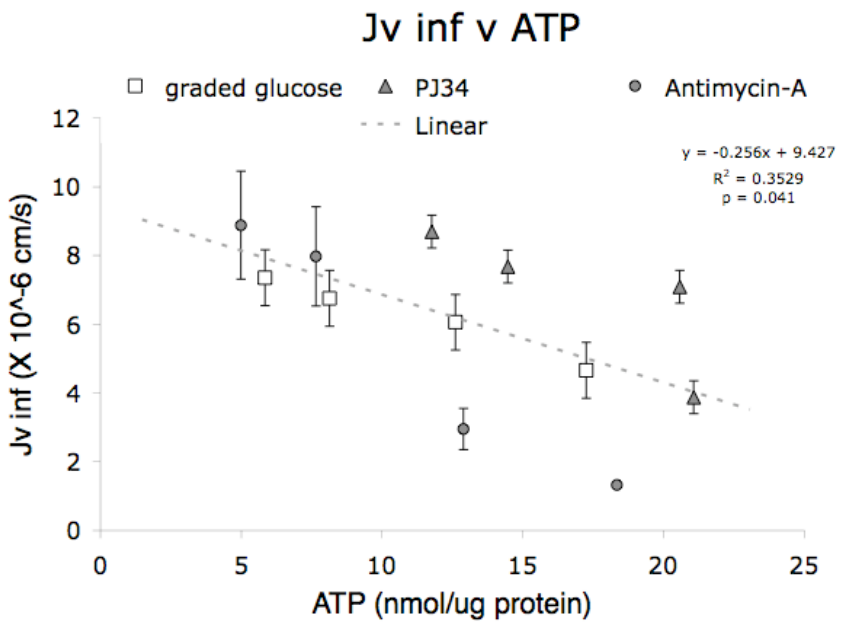

Figure 4.15) JV∞ for three different experimental preparations AA, GG, and PJ34. Data for BAEC cultured as above for each preparation are plotted as a function of ATP concentration.

Figure (4.16) shows the result of transport experiments in AA with LDL. The trend was for increasing permeability with decreasing ATP concentration.

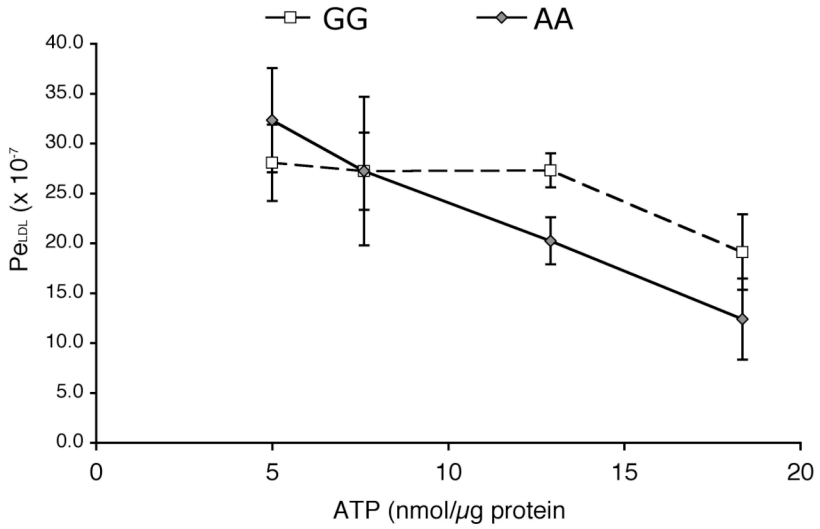

Figure 4.16) Transport of LDL in AA depletion (solid line, shaded diamonds) compared to GG (broken line, open squares). BAEC were grown for 3 days on fibronectin coated polycarbonate filters in 5mM glucose to confluence, then exposed to antimycin-A for 0 (no exposure), 15, 30, and 120 minutes. AA media was removed, and replaced with fresh media. Filters were allowed to recover for 24 hours, then were placed in the pressure-flow apparatus with 10μg/ml DiI-LDL added to the luminal compartment and allowed to equilibrate for 1 hour. Solute flux was calculated against fluorescence of a standard DiI-LDL of known concentration. a) After 1 hour, the filters were subjected to a 10 cm H_2O transmural pressure gradient for 1 hour. Fluorescence readings were taken during the entire process, and the rate of change converted to solute flux as described in the text. Convective permeability to LDL showed a linear increase with increasing ATP depletion, and was significantly different from GG at 10 mM equivalent ATP depletion.

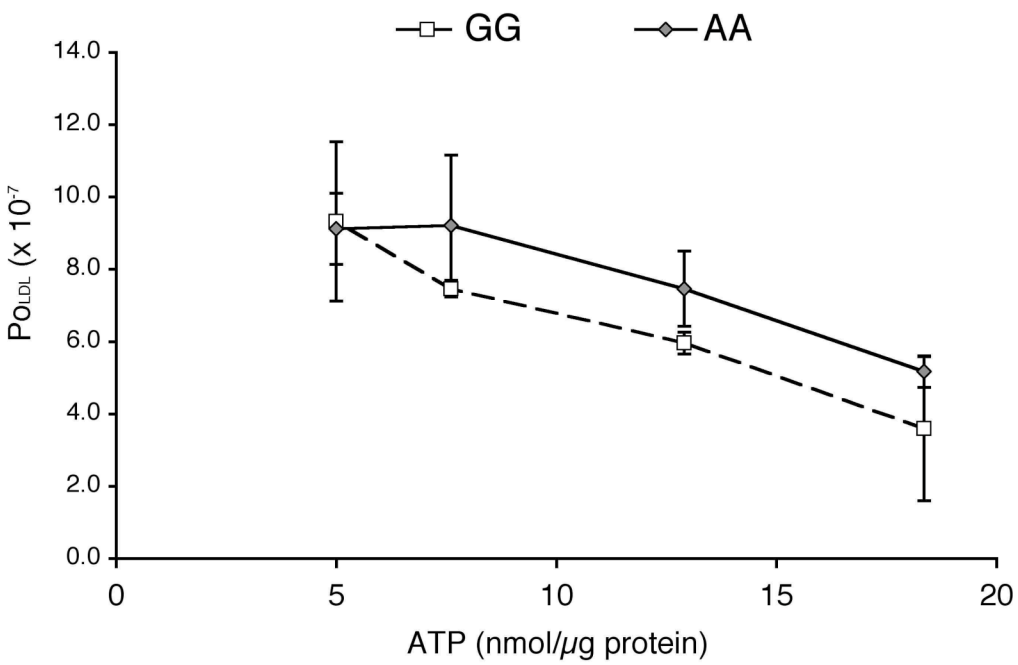

4.16 b) After 1 hour, pressure was removed and diffusive flux was recorded for another hour after. Diffusive flux showed no significant difference from GG equivalent, increasing from 3.1 ± 0.92 × 10^{-7} cm/s at control to 9.79 ± 0.92 × 10^{-7} cm/s at 30 mM ATP equivalent. Linear regression of all data was significant (*r* = -0.97, p = 0.001).

Discussion

Graded Glucose Experiments

Endothelial dysfunction in diabetes, in particular the adaptive response of the vasculature, has been the subject of much important research. Principally, the adaptive response has focused on whole vessel explants, animal models (Scalia, Gong *et al.* 2007) or the function of the endothelium as a regulator through the production of NO, VEGF, or other paracrine factors (Endemann and Schiffrin 2004; Mohan, Reddick *et al.* 2008). In these studies, it is the vasodialative response that has been the measure of vascular integrity (Liu and Gutterman 2002), and the dysfunction of the endothelium described in terms of differential regulation of protein production in response to high glucose conditions (Kanetsuna, Takahashi *et al.* 2007; Mohan, Reddick *et al.* 2008; Molnar, Yu *et al.* 2005). Diffusive permeability to solutes has been shown to increase in different cell culture models of diabetes (Duan, Paka *et al.* 2005; Ishii, Koya *et al.* 1998; Popov and Simionescu 2006), and is an indicator of the number of leaky junctions. But the dramatic reduction in convective flow during, and of diffusive permeability found after the sealing effect, implies that experimental monolayers that are not exposed to flow have an underdeveloped barrier function. Therefore we have subjected the conclusions of these investigations to further validation. In this study, we have shown a more critical role for the endothelium by demonstrating an increase in hydraulic conductivity of BAEC monolayers in high glucose cell culture. In Figures 4.6) a) and b) we have reconfirmed

the hypothesis of (DeMaio *et al.* 2004) that the role of the endothelium in preserving vascular function includes an active sealing response, and, more importantly, have demonstrated here that sealing is impaired—not at the supraphysiological range (≥ 20mM) that is typically used in cell culture experiments—but at the physiologically relevant level of 10mM glucose.

ATP depletion in hyperglycemia has been reported before. Our results as seen in Figure (4.5) are in qualitative agreement with previous studies. We found a decrease from 17.2 ± 1.4 nmol/μg protein at 5mM to 12.6 ± 2.4 nmol/μg protein at 10mM, a drop of 35.0 ± 5.7%. (Soriano et al. 2001) found that ATP decreased from 31.33 ± 1.29 at 5mM to 18.04 ± 5.35 nmol at 11 mM, a drop of 41.9 ± 4.0%. The higher value of ATP found by Soriano et al. may come from the fact that in their experiments, whole vessels were homogenized for the preparation of cell extracts, including smooth muscle cells and fibroblasts which have a larger number of mitochondria, therefore a greater ATP producing capacity. Soriano et al. also used a high performance liquid chromatography (HPLC) column, which requires a different method of tissue preparation, and may produce a different ATP to protein ratio than our method. (Lieberthal, Menza *et al.* 1998) also used firefly luciferase and found a normal resting value of 18nmol/mg protein in murine renal epithelium.

The increase in PARP with increasing glucose in Figure (4.4) is in agreement with (Du, Matsumura *et al.* 2003). They showed an increase from 147.5 ± 4.7 pmol/min/mg protein at 5mM to 254.9 ± 15.6 pmol/min/mg protein at 30 mM, an increase of 70%. Our results showed a higher increase in PARP activity (115%), from an identical value at

5mM of 148.078 ± 16.8 to 311.0 ± 22.7 at 30 mM. The series of graded glucose concentrations used in our experiments showed a strictly linear increase in PARP activity with increasing glucose, and gives a very high level of confidence to our findings, with a correlation coefficient of PARP activity with glucose concentration of 1 as shown in Table (4.3), and, for a linear regression of PARP activity against glucose concentration, a p value of less than 0.001 ($n > 40$).

In Figure (4.3) the increase of superoxide with increasing glucose is in agreement with previous results that span 5 decades of research in ROS. The increase in the interval from 5mM to 10mM (75%) is larger than that between any of the intervals between higher concentrations (although statistical significance by t-test is not found at 10mM ($p = 0.06$)), indicating that the increase in ROS saturates at high glucose. Since the physiologically relevant range of high glucose is from 10 mM to 15 mM, this may have an important significance in understanding the relationship between glucose, ROS, PARP activation, and ATP depletion. Superoxide is, of course, not the only ROS present in high glucose cells, and the result of Figure (4.3) is not conclusive. We include it here as supporting evidence of the mechanism of ATP depletion as outlined in our hypothesis. Increased ROS is known to cause DNA damage, and to activate PARP. And Figure (4.4) shows PARP activity was strongly negatively correlated to ATP levels ($r = -0.95$).

Together, the results of Figure (4.3), Figure (4.4), and Figure (4.5) corroborate existing theory and observation that hyperglycemia increases ROS, activates PARP, and depletes ATP, and demonstrate that this relationship exists in high glucose cell culture of BAEC.

Figure (4.8) shows that the number of apoptotic cells in at 20mM glucose high glucose increases to 3.2 times control levels (5 mM glucose) and (by linear interpolation) to 4.0 times control levels at 25 mM. Our results are in qualitative agreement with the increase in apoptosis for human umbilical vein endothelial cells (HUVEC), found at 20 mM glucose to be 2.5 times control (Ho, Liu *et al.* 2000), and for human aortic endothelial cells (HAEC) found, at 25 mM glucose, to be 1.77 times control (Duffy, Liew *et al.* 2006). Our slightly higher rate of apoptosis from high glucose in our experiments and those of published results is probably due to the fact that our study was carried out in a cell culture model. Although the rate of apoptosis in BAEC has not been reported previously, either *in vivo* or *in vivo*, there is no obvious reason why bovine aorta should have a higher rate of apoptosis than human. It is more likely that, by isolating the endothelial monolayer in a defined environment, we are inducing an additional cell culture specific increase in apoptosis as has been reported before (Hotter, Palacios *et al.* 2004).

We judge cell dysfunction by $J_{V\infty}$ and by large molecule permeability. Figure (4.5) shows that increased glucose increases monolayer $J_{V\infty}$. Secondly, Figure (4.9a) and (4.9b) show that P_e and P_o for LDL increases with increasing glucose. (Huang, Y., Jan *et al.* 1998) attribute macromolecular permeability to rare isolated leaky endothelial junctions, many of which (Huang, Y., Jan *et al.* 1998; Lin, Jan *et al.* 1990) have attributed to dying or missing cells. Thus it is important to compare the increasing rate of apoptosis in increasing glucose concentration shown in Figure (4.8), to the increased permeability shown in (4.9a) and (4.9b). The relationship between apoptosis and glucose

concentration is strictly linear. Figure (4.9b) shows that diffusive permeability to LDL increases with increasing glucose. In contrast, Figure (4.9a) shows that convective permeability increases at 10mM, and then has no significant increase at higher glucose, even though apoptosis continues to increase. We speculate that the mechanism for these disparate effects between convective and diffusive transport may have to do with the action of the glycocalyx. (Yao, Rabodzey *et al.* 2007) observed redistribution of the glycocalyx to the intercellular junction in shear flow. In Chapter 3), we noted that a gap width small enough to exclude single molecules of LDL (< 20 nm) showed poor convergence with data. The predicted gap width that allows convergence is 25 nm, large enough to admit LDL. Since LDL is not observed to flow through the intercellular cleft at the same rate of water flow, this prediction suggests the presence of a molecular sieve that can span the 25 nm gap. The fact that the steady increase of water convection with increasing glucose does not correlate to the initial increase and plateau of convective transport of LDL with increasing glucose, suggests a molecular sieve that becomes increasingly dominant in convection only after $J_{V\infty}$ reaches the level seen at 10 mM glucose. The fact that diffusive transport of LDL does correlate to water flux suggests that the effect of this molecular sieve is smaller without flow. The role of the glycocalyx as a molecular sieve has been investigated previously (Zhang, Adamson *et al.*) and if it is redistributed to the intercellular junction under transmural flow, the way it is in shear flow as reported by (Yao, Rabodzey *et al.* 2007), the glycocalyx might act as the convection activated sieve described here.

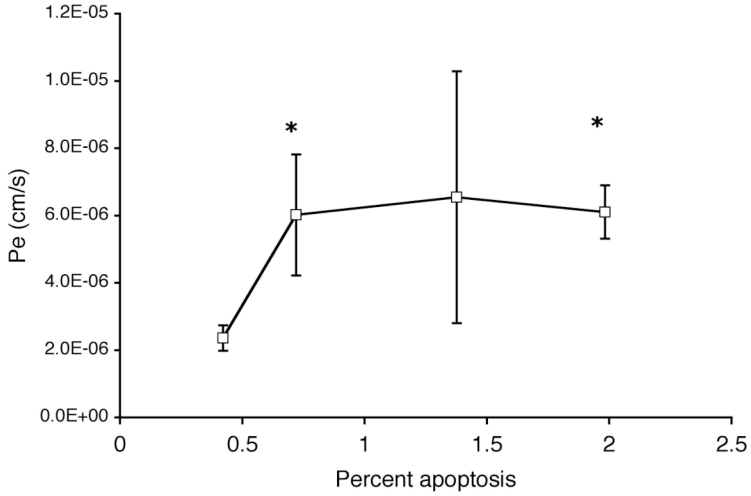

Figure 4.17a) LDL transport vs. apoptosis in graded glucose. Permeability is replotted as a function of apoptosis in graded glucose. a) Permeability results from Figure (4.9a) for convective transport of LDL are plotted against apoptosis results from Figure (4.8) (* $p < 0.05$ vs. 0.4 % apoptosis).

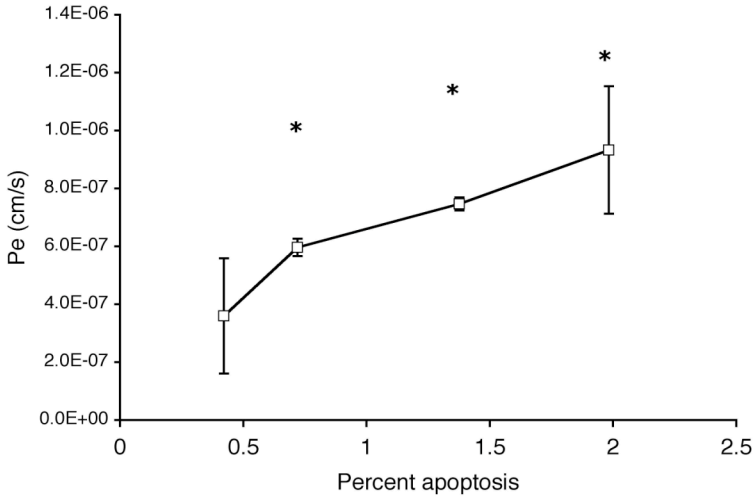

4.17b) Permeability results from Figure (4.9a) for diffusive transport of LDL are plotted against results from Figure (4.8) (* $p < 0.05$ 0.4 % apoptosis).

Steady state ATP levels represent a balance between ATP synthesis and consumption. The energy consuming properties of the cytoskeleton are well known, and energy depletion has been shown to disrupt tight junctions in renal epithelial cells (Bacallao, Garfinkel *et al.* 1994). In the previous chapter we presented evidence of junctional reorganization during the sealing effect, and for this reason we compared the ATP level in cells before and after being subjected to water flux experiments. Figure (4.7). shows that the result is as expected: a significant drop in ATP levels after sealing. However, the consumption of ATP is not equal for normoglycemic cells and hyperglycemic cells. Cells grown in 30 mM glucose use more than twice as much of their steady state ATP reserve (2.1:1) in sealing as do those grown in 5 mM glucose. Putting this in terms of known ATP values for each preparation, we note that normal cells reduce their ATP reserve by 5.0 nmol/μg protein, whereas hyperglycemic cells reduce their ATP reserve by only 3.6 nmol/μg protein.

In contrast to P_e and P_o, $J_{V\infty}$ dysfunction probably depends on loss of integrity of the tight junction due to ATP depletion. To gain some insight into this, we examine monolayers sealing in graded glucose. Monolayers at all tested glucose levels seal, showing a slight decrease in diffusivity at 10mM, which disappears at higher glucose concentrations. For high glucose treatments, $J_{V(t)}$ is statistically higher, by paired t test ($p < 0.01$), than control at every time point. $J_{V\infty}$ for 30 mM glucose is 68.2 ± 6.3% lower than initial J_V , whereas $J_{V\infty}$ for 5 mM glucose is 74.0 ± 3.5%, lower than its initial value. These percentages are statistically identical (error range is the standard error between the means of $J_{V(t=0)}$ and $J_{V\infty}$ within each glucose concentration $p = 0.10$). The amount of flow

that is attenuated also appears higher for high glucose, $22.9 \pm 7.5 \times 10^{-6}$ cm/s, compared to normal glucose, $13.6 \pm 1.5 \times 10^{-6}$ cm/s, but again not significantly so ($p = 0.12$).

The explanation for this counterintuitive result is found in the theory of (Atkinson 1977), that proposes the existence of a hierarchy of ATP-consuming processes. Experiments by (Buttgereit and Brand 1995), and (Wieser and Krumschnabel 2001), which validate this theory, established that if ATP supply is compromised, processes that are less essential for immediate cell survival (such as protein synthesis) are shut down, but those that are critical to survival (such as mitochondrial proton leak) continue to consume ATP. The results in Figure (4.5) and (4.6) show that the sealing effect, for the level of ATP depletion found at 30 mM glucose, falls into the latter category. In ATP compromised cells, non-vital ATP consuming processes that are operational in normal cells are shut down, while sealing proceeds unimpaired. This is consistent with sealing being a net ATP consumer, but not being dependent upon ATP concentration at the level of ATP depletion found in hyperglycemia.

Table (4.1) corroborates the assertion that increased glucose does not affect sealing, since diffusivity and sealing potential are unchanged at 30mM glucose. From our validation experiments in Chapter 3) in blocking and downregulating AQP-1, we argue that increased $J_{V\infty}$ with unchanged diffusivity and sealing potential is evidence of a either an increased frequency of breaks in the tight junction, or an increased number of cells with defective adherens junctions ($w > 25$nm, i.e. “leaky junctions”), or a combination of the two, and is not caused by impaired diffusion of protein to the cell border.

The level of ATP depletion that we found in high glucose conditions was not sufficient to cause widespread necrosis. Even in the highest glucose case ATP was depleted only to 34.8 % of normal: not enough to trigger necrosis (Lieberthal, Menza *et al.* 1998). On the other hand, ATP depletion was sufficient to increase the number of apoptotic cells, and this is borne out by the observed increase in apoptosis.

Mechanistic steps in Figure(4.1)

Let us now refer to the diagram in Figure (4.1). We begin with the results from the caspase inhibitor experiments.

Pathway 6: ATP depletion by increased apoptosis

Figure (4.10) shows that we found no evidence of a positive feedback effect of increased apoptosis on decreased ATP levels. Blocking apoptosis by caspase inhibitor reduced the number of apoptotic cells to 4.5 ± 0.02 %, which is not significantly different than normal levels of 4.2 ± 0.1 % (data not shown), but ATP levels were identical at each glucose concentration except for 10 mM. We now argue that the highly significant increase of 88.8 ± 23.2 % at 10mM is not a result of ATP recovery by blocking of apoptosis.

Apoptosis requires energy for an orderly shutdown of cell functioning: a minimum concentration of ATP must be maintained for a cell to properly enter an apoptotic state (Kerr, Wyllie *et al.* 1972; Lelli, Becks *et al.* 1998; Terminella, Tollefson *et al.* 2002), and remaining stores of ATP will be rapidly depleted by the cell as it progresses through the process of apoptosis. However, given that the highest rates of

apoptosis in our experiments are on the order of 2 per hundred cells, even instantaneous elimination of intracellular ATP in every apoptotic cell would only result in a drop of 2% at 30mM, more than an order of magnitude too small to explain the observed drop. This means that apoptosis is not a significant contributor to ATP depletion at high glucose. At 10mM glucose, ATP is reduced by 11.8% relative to control, and apoptotic cells account for less than 1% of the population. Since restoration of the full amount of ATP used in apoptosis at 10mM glucose is not enough to restore even normal ATP levels, it cannot account for the observed 88.8 % surplus of ATP shown at 10mM glucose in Figure (8). Further, it is not possible that the effect of applying a pan-caspase inhibitor in moderately high glucose is to stimulate the production of ATP beyond normal levels. The caspases have not been reported to participate in glycolysis, and since over-activation of the mitochondria has been identified as the cause of ROS induced ATP depletion, any caspase regulated steady-state hyperstimulation of mitochondrial oxidative phosphorylation would have the effect of reducing steady-state ATP, rather than raising it. Instead, the application of the caspase inhibitor may be interfering with the consumption of ATP in the cell, allowing a surplus to accumulate. Since pathway 6 does not significantly contribute to ATP depletion, the results shown in Figure (4.10) imply that there is a widespread sub-lethal ATP depletion in endothelial monolayers exposed to high glucose.

Pathways 4 vs. 5: Relative contribution of PARP activity and ATP depletion to cell dysfunction.

Pathways 4 and 5 both appear to lead to cell dysfunction. We now use the alternate method of ATP depletion of AA treatment to weigh the relative importance (or the existence) of these two pathways. The mechanism of ATP depletion is different in AA treated than in GG monolayers. Rather than activating PARP and depleting ATP by reducing intracellular NAD+, AA acts directly on the mitochondria by disrupting the electron transport chain. Although antimycin-A has been used by some researchers to upregulate ROS and increase apoptosis, our experimental protocol is designed to minimize these effects. For high dosage (> 50 nM) antimycin-A will, by dysregulating the redox balance, lead to a temporary 10-fold increase in ROS, which also increases apoptosis. However, this temporary increase in ROS returns to normal after a period of about 90 minutes {Han 2007}. Our experimental protocol involves a lower dosage and a 24 hour recovery period before experimental measurements are taken, during which time upregulated apoptosis and ROS return to near normal, and the predominant lasting effect is a graded partial metabolic impairment of the mitochondria to produce ATP {Park, 2007}{Pham 2004}. In this way we activate pathway 5 without activating pathway 4. If the results are similar to that found for equivalent glucose levels, this would suggest a negligible contribution of pathway 4 relative to pathway 5.

Figure (4.11) demonstrates that by treatment with antimycin-A we can mimic the levels of ATP depletion found in high glucose. ATP is depleted sharply for short AA exposure times (< 30 mins), but seems to saturate at high exposure times—as it does in

high glucose. As (Lelli, Becks *et al.* 1998) showed, depletion to levels below 25% will cause necrosis. Since we allowed cells to recover from AA treatment for 24 hours before experiment, necrotic cells are presumably eliminated from the population, and the remaining live cells are functioning at the lower limit of mitochondrial ATP production to support viability. The fact that our 30mM preparation, and the high AA treatment preparation lead to nearly the same level relative to normal (27% for AA and 34% for 30mM glucose, no statistical difference) and yet still seal, offers further support that sealing is a an essential function of the endothelium under convective conditions, in that even with ATP levels depleted nearly to the limit of viability, some ATP is still reserved for sealing.

Figure (4.12a) and Table (4.2) show that the energy that is expended on the sealing effect in AA depleted monolayers may be slightly less in than those at equivalent glucose concentrations. Table (4.2) shows that the difference in the average percent of attenuation (65.6 ± 0.75 %) between AA depleted and GG is consistent with the AA cells lower diffusivity ($p = 0.006$), and higher sealing potential ($p = 0.001$) for all treatments with a resting level of ATP below 70% of normal. The sealing effect is markedly impaired in AA depleted cells, with the amount of flow attenuated by sealable junction 8.6% less, and the sealing potential 3.5 times higher for highly depleted AA cells than for normal cells. It can be seen in Figure (4.12) that this defect in sealing of AA depleted monolayers results in $J_{V\infty}$ that is 1.043×10^{-6} cm/s larger at 34% of normal ATP than $J_{V\infty}$ of the equivalent GG treatment (30mM), although this amount is smaller than the associated standard error of the mean of $J_{V\infty}$ at 30mM glucose. In summary, although a

significant effect of ATP level in AA treatment has been found on diffusivity and sealing potential, the effect on transmural flow relative to high glucose treatments of equivalent ATP is not significant. We can predict, from assumptions of the transport model, that the amount of sealable junction per unit area of monolayer is smaller in AA treatment, and the junction strand is less completely formed at the beginning of sealing, but the effect on transmural water flow is too small to resolve using the current method. Even without statistical significance, we can infer, from the fact that $J_{V\infty}$ is slightly higher for AA depleted cells, that pathway 4 is relatively insignificant compared to pathway 5.

Although the effect on water flux is small, the difference in the effect of AA depletion vs. GG on monolayer permeability to LDL can be readily distinguished. Figure (4.13a) shows that convective transport of LDL in AA depleted monolayers was significantly lower than GG monolayers at 10mM equivalent ($p < 0.04$) and did not exhibit the marked step increase at ATP equivalent to 10mM glucose. The increase in LDL permeability was highly linear ($r = -0.97$ $p < 0.001$) and showed no sign of levelling off as in GG. Figure (4.13b) shows that diffusive permeability was statistically identical to GG treatments. P_o increased slightly less than 2-fold, from $5.17 \pm 0.40 \times 10^{-7}$ cm/s for control (no AA), to $9.12 \pm 0.98\ 10^{-7}$ cm/s at 34% of control (120 min AA treatment). In contrast to GG experiments, the increase in P_e was closely negatively correlated to the increase in apoptosis with ATP depletion, ($r = -0.97$, $p < 0.001$). This result infers that macromolecule transport in GG is not entirely controlled by pathway 4 at physiologically relevant glucose concentrations. Moderate activation of PARP, and slight reduction of

resting ATP appear to be exerting some control (or markers of some other mechanism that is) over cell dysfunction through pathway 5.

Pathways 1 vs. 2: Relative contribution of high glucose mediated activation of PARP or depletion of ATP

By blocking the activity of PARP we can turn off pathway 3, and compare ATP depletion (and all downstream processes from it) in GG independently of the effect of PARP. If there is little or no difference between treatments with similar ATP level with and without PARP, then we can conclude that pathway 1 is negligible relative to pathway 2.

For our experiment, we take advantage of the fact that the effect of PJ34 to block the activity of PARP and restore ATP is linear in dose, allowing us to reduce—but not eliminate—the effect of pathway 3, and to preserve the trend of increasing PARP activity and decreasing ATP levels with increasing glucose. Our experimental dose was optimized at 250 nM. Table (4.3) shows that this dose reduces PARP activity by approximately 40% at each glucose concentration and restored ATP levels by an average of 6 nmol/μg protein at each concentration of glucose. Figure (4.14) offers strong support of our assumption that ATP depletion in hyperglycemia is primarily a function of PARP activation alone, and not a direct result of glucose, showing that restoration of ATP can be fully explained by PARP activation ($p < 0.001$ for linear regression of ln(ATP) *vs.* PARP between treatments).

We had expected that titration of pathway 3 by PJ34 would restore $J_{V\infty}$ values at all glucose concentrations in proportion to its effect on PARP activity and ATP depletion. However, this expected restoration of barrier function with ATP was not found. Figure (4.13a and b) shows that $J_{v\infty}$ still increased with increasing glucose concentration, with no statistical change seen after the application of PARP inhibitor. Although results are not significantly different, a slight increase in steady state permeability to water flux was seen in PJ34 treated monolayers, giving little support to the hypothesis of restored endothelial function by administration of PJ34. And, similarly to AA depletion, as shown in Table (4.4), diffusivity was significantly lower than control monolayers at all glucose concentrations above 5mM.

An unforeseen side effect of the PJ34 treatment was pronounced cytotoxicity in the presence of LDL. Although monolayers appeared normal before the experiments, macromolecular transport was at the same rate as the convective flow of water for all treatments (data not shown). Visual inspection of filters following the experiment showed nearly complete disintegration of the monolayer.

The major figure of this chapter is Figure (4.18) which we rely on to test the hypothesis that monolayer dysfunction, to a first approximation, depends only on ATP depletion. It clearly demonstrates that for each experimental treatment, GG, AA, and PJ34, a decrease in ATP causes an increase in $J_{V\infty}$. Linear regression of all samples shows a negative linear dependence of $J_{V\infty}$ upon ATP ($r = -0.81$, $p = 0.041$). The 10 mM glucose PJ34 treated sample (at ATP 20.6, $J_{V\infty}$ 7.1) is an influential outlier (Cook's distance 0.47). Without this observation, the p value drops to 0.012. For both AA and

PJ34 treatments, there are collateral effects, possibly related to the mechanism of ATP depletion, but still preserve the trend of decreased barrier function with decreasing ATP concentration.

This result can be compared to the linear relationship between $J_{V\infty}$ and ATP by simultaneously solving the linear equations of ATP as a function of glucose, and $J_{V\infty}$ as a function of glucose. For glucose concentration, g, and ATP levels, a the first relationship, from least squares fitting of the data shown in Figure (4.3) can be expressed as

(31)

$$a = C_a\left(16.9 - 0.342 \cdot g\right)$$

where C_a is a unit conversion factor ($p < 0.001$). And $J_{V\infty}$ and glucose have the following relationship from linear regression of the data presented in Figure (4.6a),

(32)

$$J_{V\infty} = C_j\,(4.60695 + 0.09759g)$$

where C_j is a unit conversion factor ($p < 0.05$). Solving for g in terms of $J_{V\infty}$ and substituting into equation (1) gives the linear relationship

$$J_{V\infty} = C_{ja}\,(9.427 - 0.2865\ a)$$

where C_{ja} is a unit conversion factor. This result is close to that obtained by regression of all observations of all experimental treatments.

$$J_{V\infty EXP} = C_{ja}\,(9.427 - 0.256\ a)$$

Diagram of experimental design

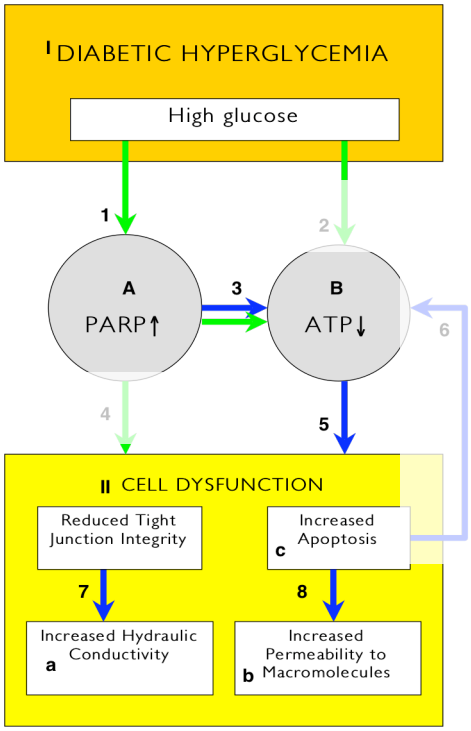

Figure 4.18) Schematic diagram of results of our experimental design. The precondition I Diabetic Hyperglycemia leads to the end point condition II Cell Dysfunction principally by pathways (1), (3), and (5). Pathway (6) was shown to have no effect on state (B). Pathway (2) was shown to have little control over the level of ATP depletion in hyperglycemia. State (A), PARP upregulation, was shown to have a dominant role, through pathway (3) to state (B) ATP depletion. In addition, pathway (4) did not lead to significantly worse dysfunction than pathway (5) alone.

Conclusions and future work

Figure (4.18) summarizes what we have learned about the mechanisms proposed in Figure (4.2). The lighter arrows indicate pathways that were shown to have a reduced influence on endothelial dysfunction, and the stronger arrows show those pathways which dominate. We have shown that transendothelial water flux appears to depend principally upon ATP concentration in hyperglycemia. Interestingly, we have shown that the sealing effect is not ATP dependent in GG experiments in general, but has a lower diffusivity at 10 mM, similar to both AA treatment and PJ34 treatment relative to control. This implies that, for cells exposed to high glucose, with physiologically functioning mitochondria and PARP, the increase in water flux with increasing glucose does not appear to be a function of the diffusivity of tight junction protein, or of the ability of the endothelium to form tight junctions during sealing, but rather is due to an increase in the area of non-sealing intercellular clefts per unit area of endothelium.

We devote the rest of this section to speculation about the meaning of our individual results. An increase in the number of large gaps due to incomplete formation of the adherens junction would be consistent with the observed increase in non-sealing flow. The magnitude of the increase in flow could also be accounted for if 30% of the total cleft width was approximately 30 nm wide.

The results of ATP dependence of $J_{V\infty}$ in PJ34 experiments are qualitatively similar to those of GG and AA, but differ in absolute amount. It is likely that the

On the other hand, the sealing response is markedly reduced in both AA and PJ34 treatments. The answer may be in the dynamic state of the cytoskeleton. When exposed

to shear stress, it is well known that endothelial cells will align with the direction of flow, and that the actin cytoskeleton reorganizes, forming stress fibers. (Osborn, Rabodzey *et al.* 2006) has shown that this reorganization is not merely a rearrangement of actin from one part of the cell to another, but involves a threefold increase in f-actin turnover, the cycle of depolymerization and repolymerization. Increased turnover of F-actin, as a net consumer of ATP, and as a buffer for as much as 40% of the adenosine nucleotide phosphate pool of the cell, could account for the observed ATP consumption during sealing.

We speculate that the dependence of sealing on ATP in our two experimental conditions may be explained by this same effect. In AA depletion, the inhibition of glycolysis cause ribosylation of GAPDH by PARP is unchecked; the ATP depletion is therefore a result of decrease in both oxidative phosphorylation and glycolysis. The rate of production of ATP by glycolysis is much faster (on the order of $s \times 10^{-3}$) than oxidative phosphorylation (on the order of $s \times 10^{1}$), but it accounts for less than 10% of total ATP production (Gibbs 1978). When the glycolytic pathway is blocked, the ATP demand of the cell is shifted to the mitochondria which will subsequently increase their rate of production about twofold (Harrison, van Wijhe *et al.* 2003). However, an increase in metabolic rate of AA-bound mitochondria will also result in a significantly larger production of superoxide radical. The result is a negative feedback loop in which the rate of ATP production is decreased by the rate of consumption (Nicholls and Budd 1998). The catastrophic result of this cascade, when coupled with the rapid actin turnover, could be ATP depletion below the apoptotic limit, resulting in a complete loss of function.

With all systems stopped, the mitochondrial system could slowly restore ATP to a functional level. The net effect would be that of a time delay in the organization of the actin cytoskeleton, and a delayed sealing effect. The sealing model could be used to examine the validity of this hypothesis. If ATP levels and rates of apoptosis are measured at intermediate time points in the sealing process, the rate of ATP consumption and its critical effects can be developed as a function of time. The comparison of this data with the results of the sealing model would determine if an energy mediated slowing of cytoskeletal polymerization was present.

The failure of PJ34 to restore normal barrier function, and the fact that PJ34 monolayers are leakier at equivalent ATP levels, could possibly be explained by the same interaction between glycolysis and oxidative phosphorylation. By partially preventing the ribosylation of GAPDH, PJ34 allows a limited improvement in the rate of glycolysis relative to control. But in the presence of a functional glycolytic pathway, the mitochondrial rate of ATP production is slow. Slow turnover of ADP to ATP may allow an increased ATP level for resting cells, but when challenged by the rapid turnover of f-actin to g-actin during convective flow, could result in rapid ATP depletion. If this were the case, then the apparent restoration of ATP level seen in PJ34 would be an inaccurate measure of the health of the endothelium, since it could be rapidly depleted.

We further speculate that this slowing of the rate of ATP production may also account for the decreased diffusivity seen at 10 mM glucose in GG experiments. At 10 mM increased glycolysis is enough to keep the mitochondrial rate of ATP production slow, but does not provide enough additional ATP to compensate for increased actin

cycling. At higher concentrations of glucose, decreased glycolytic activity from PARP ribosylation of GAPDH shifts the burden of ATP production to the mitochondria, which then increase the rate of production to meet the additional demands of cytoskeletal reorganization.

Another consideration is whether there is a requirement of ATP in the phosphorylation and subsequent binding of junctional proteins. If the formation of the junctional complex itself requires ATP, then the boundary conditions of the model will change at the cell border. Instead of instantaneous incorporation, we would have to consider a finite rate of incorporation. If this is the case, and the effect is large enough to be rate-limiting in junction formation, then the goodness of fit of data curves evaluate by this method should improve over the existing model. Additional experiments to validate these speculations should consider the goodness of fit of the sealing model to experimental curves as a parameter of comparison.

Chapter 5. Summary

Contributions of the current study

We have demonstrated that endothelial monolayers in culture show an increased hydraulic conductivity, and permeability to LDL. Using the mathematical model of the sealing effect developed in Chapter 2) we were able to resolve a very small increase with high statistical confidence. Using a series of graded glucose concentrations we also were able to detect endothelial dysfunction at physiologically relevant glucose concentrations, rather than the extremely high levels typically used in cell culture models of hyperglycemia.

In Chapter 2) we developed a mathematical model based on physically relevant mechanisms to extract meaningful parameters that describe the dynamic response of the endothelium to changes in transmural water flux. We showed that these new parameters can be used to evaluate the quality of experimental data, by lowering the error associated with data acquisition, and determining if experimental preparations are responding to experimental conditions in a similar fashion. By automating the model, we reduced the need for user judgement, and allow the experimentalist to subject all data sets to the same objective evaluation to determine the initial flow, the rate of sealing, and the steady state flow. More importantly we showed that these new parameters can be used in a predictive manner. By a best-fit analysis, and correlation with existing theory and experiment, we hypothesize that the intercellular cleft in BAEC is approximately 25 nm wide. The further significance of this conclusion is that it implies the presence of a molecular

sieve—presumably the glycocalyx, which has been suggested to function in that role—to regulate the transport of LDL through the monolayer. Without a molecular sieve, a 25 nm gap is presumably wide enough to allow significant LDL transport by convection. In addition, we predicted that the sealing effect results from the translocation of protein from the interior of the cell by a diffusive mechanism that is faster than motor protein transport on microtubules, but slower than free diffusion in the lumen.

In Chapter 3) we validated some of the assumptions, predictions and hypotheses which came from our analysis of the parameters extracted from data by the transport model. We assumed that sealing is a biologically active process that takes place only in the intercellular cleft. By blocking the transcelluar route of aquaporin-1, we demonstrated that, in fact, the sealing effect is independent of transcellular flow. We found evidence that intracellular transport is the dominant mechanism of the sealing effect. By fixing membrane proteins we were able to reduce the amount of sealing without affecting the rate at which sealing occurs, or the steady state water flux. In addition our results suggest a role for a mechanism of transient dynamic instability in the tight junction. By crosslinking intracellular proteins we found that not only did the rate of sealing drop dramatically, but more surprisingly, that the level of $J_{V\infty}$ was also dramatically lower. This result suggests that a transient unsealing that occurs at the beginning of the sealing effect in normal cells was prevented by strong fixation.

In Chapter 4) we applied the sealing model along with traditional lab techniques to attempt to gain some insight into the behavior of endothelial monolayers in high glucose. We found evidence to support the hypothesis that PARP upregulation causes

cell dysfunction by its regulation of ATP levels. Further, we showed that endothelial dysfunction shows a significant dependence on ATP levels. We demonstrated that convective permeability to water and solutes increases with increasing glucose. But we also found that there was little or no difference in ATP-depletion mediated hydraulic conductivity whether the ATP depletion was caused by PARP activity, or by another method. (Huang, Y., Jan *et al.*) and (Lin, Jan *et al.*) have provided strong evidence to that approximately two thirds of the leaky spots in the endothelium that allow increased macromolecular transport colocalize with apoptotic or mitotic cells. We found evidence that may suggest a widespread sub-lethal ATP may be responsible for some of the balance of those leaky spots. We found that ATP depletion was linearly correlated to apoptosis, but that the increase in macromolecular transport, although increased in high glucose, did not correlate to the increase in apoptosis. In contrast to hydraulic conductivity and diffusive permeability to LDL, we found that convective transport of LDL did depend on the method of ATP depletion. Whereas ATP depletion by chemical anoxia induced an increase in permeability proportional to apoptosis, in hyperglycemic ATP depletion, we found an initial increase in permeability to LDL followed by a plateau. Returning to one of our speculative results from Chapter 2) these results offer another indicator that a molecular sieve may be functioning in endothelial cell dysfunction. Sub-lethal ATP depletion could account for a widening of intercellular clefts without a concomitant increase in apoptosis, and the action of a molecular sieve such as the glycocalyx could function to control transport through the wider gaps.

Future work

Since we found evidence of endothelial dysfunction at lower levels than typically used in cell culture models, our results suggest that experimental investigation of diabetes by cell culture model do not need to concentrate on exaggerated end point conditions, but may find equally valid evidence of cell dysfunction at more physiologically relevant levels.

The evidence we developed in support of PARP mediated ATP depletion as a mechanistic link between diabetes and atherosclerosis suggest that further investigation is required. We found evidence that PARP downregulation in hyperglycemia might have a cytotoxic effect in the presence of LDL. In future work, a more complete study to resolve the different effects of PARP and ATP depletion independently from each other is required to fully understand the effect on endothelial dysfunction. Since the two systems are so intimately connected, measurements of such cross-effects as increased PARP activity or ROS levels by antimycin-A need to be collected and compared against the findings of the current study.

It also remains to further validate the physical meaning of our extracted parameters. A more precise determination of the nature of protein transport in the sealing effect will increase the predictive power of the model. Studies involving cytoskeletal reorganization will provide valuable new insight. With a more complete understanding of the molecular mechanisms behind sealing, the existence of a role for the glycocalyx in regulating transport through very wide junctions could be investigated. The existence of a very wide junction that is still selectively permeable might resolve the mystery of

impaired endothelial barrier function in what would seem to be normal healthy cells. The sub lethal ATP depletion found in our experiments, and the evidence of cell dysfunction at moderately high glucose and moderate ATP depletion, combined the opportunity provided by our transport model in the extraction of new parameters of endothelial integrity show promise of the development of new methods of analysis and new experimental design.

The dynamic response of the vascular system has long been recognized as an indicator of cardiovascular health. The sealing model now allows investigators to refine smaller differences in endothelial response than they could previously, which may lead to new fields of study.

Chapter 6. Appendices

Solution to the Diffusion Equation

We seek the distribution of protein C(r,t) in a thin, circularly symmetric cell over the interval $0 < r < 1$. The protein does not interact with the apical or basal surfaces of the cell. The concentration of protein is bounded at the center, and at a fixed concentration of 0 at the periphery.

The homogeneous dimensionless diffusion equation (repeated from equation (9)) is

(33)

$$\frac{\partial \overline{C}}{\partial \bar{t}} = \frac{\partial^2 \overline{C}}{\partial \bar{r}^2} + \frac{1}{\bar{r}} \frac{\partial \overline{C}}{\partial \bar{r}}$$

with boundary and initial conditions

(34)

$$\overline{C}(\bar{r},0) = 1 \qquad \left|\overline{C}(0,\bar{t}) < \infty\right| \qquad \overline{C}(R,\bar{t}) = 0$$

Ordinary differential equations in time *T(t)*, and space *R(r)*, by the method of separation of variables are

(35)

$$\frac{\partial T(\bar{t})}{\partial \bar{t}} + \lambda^2 T(\bar{t}) = 0$$

and

(36)

$$\frac{\partial^2 R(\bar{r})}{\partial \bar{r}^2} + \frac{1}{\bar{r}} \frac{\partial R(\bar{r})}{\partial \bar{r}} + \lambda^2 R(\bar{r}) = 0$$

Boundary conditions for the spatial equation are

(37)

$$\left|R(0)\right| < \infty \qquad \text{and} \qquad R(1) = 0$$

The solution is in terms of Bessel functions of order 0:

(38)

$$R(\bar{r}) = A\, J_0(\lambda\, \bar{r}) + B\, Y_0(\lambda\, \bar{r})$$

Applying the boundary conditions, we see that

(39)

$$R(1, \bar{t}) = 0 \qquad \text{and} \qquad B = 0$$

The eigenvalues are the roots of the eigenvalue equation

(40)

$$J_0(\lambda_n) = 0$$

Where λ_n is the *n*th root of J_0 . There is no zero eigenvalue. The normalized eigenfunctions are

(41)

$$R_n(\bar{r}) = \frac{J_0(\lambda_n \bar{r})\ \sqrt{2}}{J_1(\lambda_n)}$$

The time dependent solution is

(42)

$$T_n(\bar{t}) = T_{n0} e^{-\lambda_n^2 \bar{t}}$$

So that the eigenfunction expansion written as an infinite sum

(43)

$$C(\bar{r},\bar{t}) = \sum_{n=1}^{\infty} \frac{T_{n0} e^{-\lambda_n{}^2 \bar{t}} J_0(\lambda_n \bar{r})\sqrt{2}}{J_1(\lambda_n)}$$

Evaluation of the Fourier coefficients for the uniform initial condition

(44)

$$T_{n0} = \int_0^1 \frac{J_0(\lambda_n \bar{r})\sqrt{2}}{J_1(\lambda_n)} \bar{r} d\bar{r} = \frac{\sqrt{2}}{\lambda_n}$$

The series solution is

(45)

$$C(\bar{r},\bar{t}) = \sum_{n=1}^{\infty} \frac{2 e^{-\lambda_n{}^2 \bar{t}} J_0(\lambda_n \bar{r})}{\lambda_n J_1(\lambda_n)}$$

The spatial derivative at $\bar{r} = 1$

(46)

$$\left.\frac{\partial \overline{C}(\bar{r},\bar{t})}{\partial \bar{r}}\right|_{\bar{r}=1} = \sum_{n=1}^{\infty} \left[\frac{2 e^{-\lambda_n{}^2 \bar{t}}}{\lambda_n} \cdot \frac{\lambda_n \left[\cancelto{0}{J_0(\lambda_n \bar{r})} - J_1(\lambda_n) \right]}{J_1(\lambda_n)} \right] = -2 \sum_{n=1}^{\infty} e^{-\lambda_n{}^2 \bar{t}}$$

which can then be substituted into equation (12).

The limit as *t* goes to infinity of the time derivative of the dimensional bubble equation (equation (27)) is

$$\lim_{t \to \infty} \frac{d\, x(t)}{dt} = \frac{1}{F} \left[J_{V\infty} + \frac{\alpha}{1+\gamma} \left\{ 1 - \sum_{n=1}^{\infty} \frac{4}{\lambda_n^4} \left(\lambda_n^2 - \lambda_n^2 e^{-\lambda_n^2 \, tD/R^2} \right) \right\} \right]$$

since the sum $\sum_{n=1}^{\infty} \frac{4}{\lambda_n^2} = 1$, is identically $J_{V\infty}$. The value of the derivative at *t = 0* is

$$\frac{d\,x(0)}{dt} = \frac{1}{F}\left[J_{V\infty} + \frac{\alpha}{1+\gamma}\left\{1 - \sum_{n=1}^{\infty}\frac{4}{\lambda_n^4}\left(\lambda_n^2 - \lambda_n^2\right)\right\}\right] = \frac{1}{F}\left[J_{V\infty} + \frac{\alpha}{1+\gamma}\right]$$

Effect of Data Truncation

The effect of truncation of data from the early portion of the curve on the fitted parameters of the model was investigated. Since the analytical diffusion equation should converge to a unique solution, this model should develop a unique curve and the fitted diffusion coefficient should generate a curve that will match the data set along any subset of the data. However, since the curvature is decaying, and the noise signal (after the initial noisy period) is constant, eventually the curvature of the data will be smaller than the magnitude of the noise, and an accurate estimate of the diffusion coefficient will not be possible. For a data set with a dramatic curve diffusivity will be highly reproducible. For a relatively flat line, with little curvature multiple values of diffusivity may give similarly good fit. Therefore, if a correction for early instability by discarding early data points causes data loss from the portion of the data with the highest curvature, the remaining data may be too flat (i.e. D is too small) for a reliable fit. It is possible that the error introduced will render the fitted parameters of no value. To test the effect of early noise on the reproducibility of model results, a sensitivity analysis was performed. Several data series were selected (n = 8) and the early portion of the data was truncated at 2, 4, 10, 20 and 40 minutes. Averages of normalized parameter results were compared at each truncation point. A students' t-test was performed against the model prediction of parameters for the entire data set as control.

Sum of Squares Weighting Function

Consider the residual sum of the squares defined as

(47)

$$RSS = \sum_{i=1}^{N} \left[x_i(t_i) - m(\hat{p}, t_i) \right]^2$$

where x_I is the data point at time t_i , $m(p,t_i)$ is the model point at time t_i for parameter set p, and N is the total number of data points. The minimization of this function will give the best approximation for the parameter set if all errors are uncorrelated and have equal uncertainty. However, as noted above, the signal to noise ratio declines as the steady-state value of Jv goes to zero, thus the measurement error associated with data collection will change over time. A classic approach in this case is to use a weighted residuals sum of squares (WRSS); to divide at each time point by the measurement error variance, V_i , as follows:

(48)

$$WRSS = \sum_{i=1}^{N} \frac{\left[x_i(t_i) - m(\hat{p}, t_i) \right]^2}{V_i}$$

thereby reducing the effect of data with large measurement error. To avoid a sharp drop in the error function , a measurement error variance estimate of 1/1+e^(20/t)

(49)

$$V_i = \frac{1}{\left(1 + e^{20/(t+t_0)}\right)}$$

Optimization of t = 0

The optimum t = 0 is determined as follows. For each data set, an initial value for t = 0, known from the experimental record, is given to the curve-fitting algorithm. After

approximately 500 iterations, the method of steepest descent will return a best-fit, based on minimization of the sum of squares error (SSE). A second algorithm then marches through consecutive t_0 points, from 5 minutes before the application of pressure, to 5 minutes after (see sensitivity analysis above). At beginning points before or during the unstable noisy portion, the SSE is constant. At the first point after the early noise, the SSE drops dramatically, typically by a factor of 5 to 10. As the optimization program continues to march through the range specified the SSE will decrease, but only slightly, typically by less than a factor of 0.1. The result of this marching routine is an array of values of SSE as a function of t_0 with a sharp step at the optimal point for data truncation. A least-squares fitting algorithm using the method of steepest descent was used to minimize the expression:

(50)

$$g = \sum_{i=-N/2}^{+N/2} \left\{ e - \left(f\left(t_0 + t_i\right) + d\left[1 - S_H\left(e - f\left(t_0 + t_i\right)\right)\right]\right)\right\}^2$$

by fitting values of e and d. S_H is the Heaviside step function, equal to 1 when its argument is greater than zero, 0 when the argument is less than zero, and although undefined when its argument is zero, for practical purposes, was given the value 0 at that zero. The function $f\left(t_0 + t_i\right)$ is the SSE returned by the curve-fitting subroutine with initial data point adjusted to $t_0' = t_0 + t_i$, where t_i is the value of the time point at index $1 - i$ in the specified start-point range $-N/2$ to $+N/2$. The fitted parameter e is the value that best matches the portion of the array before the step drop, and d is the value that best matches the size of the drop. At array values indexed before the drop point, the argument

multiplying *d* is zero, and after the drop, it is 1. The optimal start point will be at the index following the last index which returns zero for the argument of *d*.

Calculation of Osmotic Forces from 1-D model
Time dependent changes in pressure due to osmotic forces opposing filtration

To take into account the Michel-Weinbaum model, equation (7) becomes

(51)

$$J_V(t) - J_{V\infty} = \alpha'\left(\Delta P - \sigma\Delta\pi(t)\right)\ f_O(t)$$

Although the endothelium in the *in vivo* case is subjected to a higher hydrostatic pressure, due to the structure of the microvessel wall, where the hydraulic resistance of the sub-endothelial tissue is in series with that of the endothelium, the pressure in the *in vivo* case corresponds to a pressure of approximately $60\ \mathrm{cmH_2O}$ (Tedgui and Lever), the very high end of the range of pressures evaluated by Zhang. L_p is in agreement between the two experiments, on the order of $1\times10^{-7}\ cm/s\cdot\mathrm{cmH_2O}$. For an initial concentration in the junction of C_J and in the lumen of C_L we want to know the time until the junction concentration reaches its steady state value C_{Jss}. At experimental pressure, we can make the assumption that the primary method of albumin transport is by convection—very fast relative to diffusion—and that the final concentration in the junction will be at the convective limit $C_{J\ SS} = C_L(1-\sigma_{EGL})$, where σ_{EGL} is the reflection coefficient of albumin at the glycocalyx. Also, the solute flux can be expressed in terms of water flux, concentration and reflection coefficient as

(52)

$$\frac{J_S}{A} = \frac{J_V}{A}(1-\sigma)C$$

Although the 1-D model assumes different transport properties in different regions of the junction, we deduce by the mean value theorem that there exists an average rate of change of concentration in the entire junction that will yield the same final concentration. We write in terms of concentration per unit area of endothelium:

(53)

$$\left(C_{J\ SS} - C_{J\ 0}\right)H = \int_0^t \left(\frac{J_S(t')}{A}_{IN} - \frac{J_S(t')}{A}_{OUT} \right) dt'$$

where H is the height of the junction. Since C_J after convection begins is always less than C_L we can set an upper limit on the clearance time by substituting C_L into the expression for solute flux out of the junction for the simplified form

(54)

$$\left(C_{J\ SS} - C_{J\ 0}\right)H = C_L \int_0^t \left(\frac{J_V(t')}{A}(\sigma_{TJ} - \sigma_{EGL}) \right) dt'$$

by the mean value theorem

(55)

$$C_L(\sigma_{EGL})H = C_L \left\langle \frac{J_V(t)}{A}(\sigma_{EGL} - \sigma_{TJ}) \right\rangle \Delta t$$

Which means that the time scale to reach steady state is

(56)

$$\Delta t = \left\langle \frac{A}{J_V(t)} \right\rangle \frac{H \cdot \sigma_{EGL}}{\sigma_{EGL} - \sigma_{TJ}}$$

(57)

$$\Delta t = \left\langle 1 \times 10^{6} \frac{s}{cm} \right\rangle \frac{4.11 \times 10^{-5} cm \cdot 0.95}{0.95 - 0.197} = 52 s$$

Substituting known parameters from the 1-D model, and our experimental extreme values for Jv gives an upper bound for the time to steady state, which we find to be from 5 to 50 seconds, much shorter than the time of the sealing effect (20 to 120 mins). Therefore we can treat the change in osmotic pressure as constant for this model.

Chapter 7. References

Adamson, R. H., J. F. Lenz, X. Zhang, G. N. Adamson, S. Weinbaum and F. E. Curry (2004). Oncotic pressures opposing filtration across non-fenestrated rat microvessels. J Physiol 557(Pt 3): 889-907.

Adamson, R. H. and C. C. Michel (1993). Pathways through the intercellular clefts of frog mesenteric capillaries. J Physiol 466: 303-27.

Ammann, H., J. Noel, Y. Boulanger and P. Vinay (1990). Relationship between intracellular ATP and the sodium pump activity in dog renal tubules. Can J Physiol Pharmacol 68(1): 57-67.

Anderson, J. M., C. M. Van Itallie, M. D. Peterson, B. R. Stevenson, E. A. Carew and M. S. Mooseker (1989). ZO-1 mRNA and protein expression during tight junction assembly in Caco-2 cells. J Cell Biol 109(3): 1047-56.

Asnaghi, V., C. Gerhardinger, T. Hoehn, A. Adeboje and M. Lorenzi (2003). A role for the polyol pathway in the early neuroretinal apoptosis and glial changes induced by diabetes in the rat. Diabetes 52(2): 506-11.

Atkinson, D. E. (1977). Cellular energy metabolism and its regulation. New York, Academic Press.

Bacallao, R., A. Garfinkel, S. Monke, G. Zampighi and L. J. Mandel (1994). ATP depletion: a novel method to study junctional properties in epithelial tissues. I. Rearrangement of the actin cytoskeleton. J Cell Sci 107 (Pt 12): 3301-13.

Baetscher, M. and K. Brune (1983). An *in vivo* system for measuring endothelial permeability under hydrostatic pressure. Exp Cell Res 148(2): 541-7.

Beauvieux, M. C., P. Couzigou, H. Gin, P. Canioni and J. L. Gallis (2004). Some processes of energy saving and expenditure occurring during ethanol perfusion in the isolated liver of fed rats; a Nuclear Magnetic Resonance study. BMC Physiol 4: 3.

Boulares, A. H., A. G. Yakovlev, V. Ivanova, B. A. Stoica, G. Wang, S. Iyer and M. Smulson (1999). Role of poly(ADP-ribose) polymerase (PARP) cleavage in apoptosis. Caspase 3-resistant PARP mutant increases rates of apoptosis in transfected cells. J Biol Chem 274(33): 22932-40.

Brownlee, M. (1995). Advanced protein glycosylation in diabetes and aging. Annu Rev Med 46: 223-34.

Brownlee, M. (2005). The pathobiology of diabetic complications: a unifying mechanism. Diabetes 54(6): 1615-25.

Buttgereit, F. and M. D. Brand (1995). A hierarchy of ATP-consuming processes in mammalian cells. Biochem J 312 (Pt 1): 163-7.

Cancel, L. M., A. Fitting and J. M. Tarbell (2007). In vitro study of LDL transport under pressurized (convective) conditions. Am J Physiol Heart Circ Physiol 293(1): H126-32.

Caplan, B. A., R. G. Gerrity and C. J. Schwartz (1974). Endothelial cell morphology in focal areas of *in vivo* Evans blue uptake in the young pig aorta. I. Quantitative light microscopic findings. Exp Mol Pathol 21(1): 102-17.

Carlier, M. F. (1992). Nucleotide hydrolysis regulates the dynamics of actin filaments and microtubules. Philos Trans R Soc Lond B Biol Sci 336(1276): 93-7.

Childs, E. W., B. Tharakan, F. A. Hunter, J. H. Tinsley and X. Cao (2007). Apoptotic signaling induces hyperpermeability following hemorrhagic shock. Am J Physiol Heart Circ Physiol 292(6): H3179-89.

Chuang, P. T., H. J. Cheng, S. J. Lin, K. M. Jan, M. M. Lee and S. Chien (1990). Macromolecular transport across arterial and venous endothelium in rats. Studies with Evans blue-albumin and horseradish peroxidase. Arteriosclerosis 10(2): 188-97.

DeMaio, L., J. M. Tarbell, R. C. Scaduto, Jr., T. W. Gardner and D. A. Antonetti (2004). A transmural pressure gradient induces mechanical and biological adaptive responses in endothelial cells. Am J Physiol Heart Circ Physiol 286(2): H731-41.

Dennerll, T. J., H. C. Joshi, V. L. Steel, R. E. Buxbaum and S. R. Heidemann (1988). Tension and compression in the cytoskeleton of PC-12 neurites. II: Quantitative measurements. J Cell Biol 107(2): 665-74.

Drake, D. M. and D. W. Pack (2008). Biochemical investigation of active intracellular transport of polymeric gene-delivery vectors. J Pharm Sci 97(4): 1399-413.

Du, X., T. Matsumura, D. Edelstein, L. Rossetti, Z. Zsengeller, C. Szabo and M. Brownlee (2003). Inhibition of GAPDH activity by poly(ADP-ribose) polymerase activates three major pathways of hyperglycemic damage in endothelial cells. J Clin Invest 112(7): 1049-57.

Duan, W., L. Paka and S. Pillarisetti (2005). Distinct effects of glucose and glucosamine on vascular endothelial and smooth muscle cells: Evidence for a protective role for glucosamine in atherosclerosis %U http://www.cardiab.com/content/4/1/16. Cardiovascular Diabetology 4(1 %M doi:10.1186/1475-2840-4-16): 16.

Duffy, A., A. Liew, J. O'Sullivan, G. Avalos, A. Samali and T. O'Brien (2006). Distinct effects of high-glucose conditions on endothelial cells of macrovascular and microvascular origins. Endothelium 13(1): 9-16.

Dull, R. O., H. Jo, H. Sill, T. M. Hollis and J. M. Tarbell (1991). The effect of varying albumin concentration and hydrostatic pressure on hydraulic conductivity and albumin permeability of cultured endothelial monolayers. Microvasc Res 41(3): 390-407.

Dvorak, H. F., L. F. Brown, M. Detmar and A. M. Dvorak (1995). Vascular permeability factor/vascular endothelial growth factor, microvascular hyperpermeability, and angiogenesis. Am J Pathol 146(5): 1029-39.

Endemann, D. H. and E. L. Schiffrin (2004). Endothelial dysfunction. J Am Soc Nephrol 15(8): 1983-92.

Feigenbaum, A., C. Bergeron, R. Richardson, J. Wherrett, B. Robinson and R. Weksberg (1994). Premature atherosclerosis with photomyoclonic epilepsy, deafness, diabetes mellitus, nephropathy, and neurodegenerative disorder in two brothers: a new syndrome? Am J Med Genet 49(1): 118-24.

Fisher, M. (2004). Diabetes and atherogenesis. Heart 90(3): 336-40.

Gabbay, K. H. (1975). Hyperglycemia, polyol metabolism, and complications of diabetes mellitus. Annu Rev Med 26: 521-36.

Gerrity, R. G., M. Richardson, J. B. Somer, F. P. Bell and C. J. Schwartz (1977). Endothelial cell morphology in areas of *in vivo* Evans blue uptake in the aorta of young pigs. II. Ultrastructure of the intima in areas of differing permeability to proteins. Am J Pathol 89(2): 313-34.

Giardino, I., D. Edelstein and M. Brownlee (1994). Nonenzymatic glycosylation in vitro and in bovine endothelial cells alters basic fibroblast growth factor activity. A model for intracellular glycosylation in diabetes. J Clin Invest 94(1): 110-7.

Gibbs, C. L. (1978). Cardiac energetics. Physiol Rev 58(1): 174-254.

Golenhofen, N., R. B. Doctor, R. Bacallao and L. J. Mandel (1995). Actin and villin compartmentation during ATP depletion and recovery in renal cultured cells. Kidney Int 48(6): 1837-45.

Gules, I., M. Satoh, A. Nanda and J. H. Zhang (2003). Apoptosis, blood-brain barrier, and subarachnoid hemorrhage. Acta Neurochir Suppl 86: 483-7.

Harrison, G. J., M. H. van Wijhe, B. de Groot, F. J. Dijk, L. A. Gustafson and J. H. van Beek (2003). Glycolytic buffering affects cardiac bioenergetic signaling and contractile reserve similar to creatine kinase. Am J Physiol Heart Circ Physiol 285(2): H883-90.

Hart, C. M., S. P. Andreoli, C. E. Patterson and J. G. Garcia (1993). Oleic acid supplementation reduces oxidant-mediated dysfunction of cultured porcine pulmonary artery endothelial cells. J Cell Physiol 156(1): 24-34.

Ho, F. M., S. H. Liu, C. S. Liau, P. J. Huang and S. Y. Lin-Shiau (2000). High glucose-induced apoptosis in human endothelial cells is mediated by sequential activations of c-Jun NH(2)-terminal kinase and caspase-3. Circulation 101(22): 2618-24.

Holman, R. G. and R. V. Maier (1990). Oxidant-induced endothelial leak correlates with decreased cellular energy levels. Am Rev Respir Dis 141(1): 134-40.

Hotter, G., L. Palacios and A. Sola (2004). Low O2 and high CO2 in LLC-PK1 cells culture mimics renal ischemia-induced apoptosis. Lab Invest 84(2): 213-20.

Hu, X., R. H. Adamson, B. Liu, F. E. Curry and S. Weinbaum (2000). Starling forces that oppose filtration after tissue oncotic pressure is increased. Am J Physiol Heart Circ Physiol 279(4): H1724-36.

Hu, X. and S. Weinbaum (1999). A new view of Starling's hypothesis at the microstructural level. Microvasc Res 58(3): 281-304.

Huang, A. L., K. M. Jan and S. Chien (1992). Role of intercellular junctions in the passage of horseradish peroxidase across aortic endothelium. Lab Invest 67(2): 201-9.

Huang, Y., K. M. Jan, D. Rumschitzki and S. Weinbaum (1998). Structural changes in rat aortic intima due to transmural pressure. J Biomech Eng 120(4): 476-83.

Hubert, C. G., S. W. McJames, I. Mecham and R. O. Dull (2006). Digital imaging system and virtual instrument platform for measuring hydraulic conductivity of vascular endothelial monolayers. Microvasc Res 71(2): 135-40.

Hunt, J. V., R. T. Dean and S. P. Wolff (1988). Hydroxyl radical production and autoxidative glycosylation. Glucose autoxidation as the cause of protein damage in the experimental glycation model of diabetes mellitus and ageing. Biochem J 256(1): 205-12.

Ishii, H., D. Koya and G. L. King (1998). Protein kinase C activation and its role in the development of vascular complications in diabetes mellitus. J Mol Med 76(1): 21-31.

Kalchishkova, N. and K. J. Bohm (2008). The role of Kinesin neck linker and neck in velocity regulation. J Mol Biol 382(1): 127-35.

Kanetsuna, Y., K. Takahashi, M. Nagata, M. A. Gannon, M. D. Breyer, R. C. Harris and T. Takahashi (2007). Deficiency of endothelial nitric-oxide synthase confers susceptibility to diabetic nephropathy in nephropathy-resistant inbred mice. Am J Pathol 170(5): 1473-84.

Kast, A. and S. P. Hauser (1992). [M. von Ardenne's multi-step cancer therapy and variations--universally applicable in oncology? Documentation No.23]. Schweiz Rundsch Med Prax 81(4): 74-7.

Kerr, J. F., A. H. Wyllie and A. R. Currie (1972). Apoptosis: a basic biological phenomenon with wide-ranging implications in tissue kinetics. Br J Cancer 26(4): 239-57.

Kim, M. H., N. R. Harris and J. M. Tarbell (2005). Regulation of hydraulic conductivity in response to sustained changes in pressure. Am J Physiol Heart Circ Physiol 289(6): H2551-8.

Kiss, L. and C. Szabo (2005). The pathogenesis of diabetic complications: the role of DNA injury and poly(ADP-ribose) polymerase activation in peroxynitrite-mediated cytotoxicity. Mem Inst Oswaldo Cruz 100 Suppl 1: 29-37.

Kolm-Litty, V., U. Sauer, A. Nerlich, R. Lehmann and E. D. Schieicher (1998). High glucose induced transforming growth factor beta1 production is mediated by the hexosamine pathway in porcine glomerular mesangial cells. J Clin Invest 101: 160 - 169.

Kou, R., S. SenBanerjee, M. K. Jain and T. Michel (2005). Differential regulation of vascular endothelial growth factor receptors (VEGFR) revealed by RNA interference: interactions of VEGFR-1 and VEGFR-2 in endothelial cell signaling. Biochemistry 44(45): 15064-73.

Kusumi, A. and K. Suzuki (2005). Toward understanding the dynamics of membrane-raft-based molecular interactions. Biochim Biophys Acta 1746(3): 234-51.

Landis, E. M. (1927). MICRO-INJECTION STUDIES OF CAPILLARY PERMEABILITY: II. The Relation Between Capillary Pressure and the Rate at Which Fluid Passes Through the Walls of Single Capillaries. Am J Physiol 82(2): 217-238.

Lee, T. Y. and A. I. Gotlieb (2003). Microfilaments and microtubules maintain endothelial integrity. Microsc Res Tech 60(1): 115-27.

Lelli, J. L., Jr., L. L. Becks, M. I. Dabrowska and D. B. Hinshaw (1998). ATP converts necrosis to apoptosis in oxidant-injured endothelial cells. Free Radic Biol Med 25(6): 694-702.

Levick, J. R. and J. N. McDonald (1994). Viscous and Osmotically Mediated Changes in Fluid Movement across Synovium in Response to Intraarticular Albumin. Microvascular Research 47(1): 68-89.

Li, J., K. Kuang, S. Nielsen and J. Fischbarg (1999). Molecular identification and immunolocalization of the water channel protein aquaporin 1 in CBCECs. Invest Ophthalmol Vis Sci 40(6): 1288-92.

Lieberthal, W., S. A. Menza and J. S. Levine (1998). Graded ATP depletion can cause necrosis or apoptosis of cultured mouse proximal tubular cells. Am J Physiol 274(2 Pt 2): F315-27.

Lin, S. J., K. M. Jan and S. Chien (1990). Role of dying endothelial cells in transendothelial macromolecular transport. Arteriosclerosis 10(5): 703-9.

Liu, Y. and D. D. Gutterman (2002). The coronary circulation in diabetes: influence of reactive oxygen species on K+ channel-mediated vasodilation. Vascul Pharmacol 38(1): 43-9.

Mandel, L. J., R. B. Doctor and R. Bacallao (1994). ATP depletion: a novel method to study junctional properties in epithelial tissues. II. Internalization of Na+,K(+)-ATPase and E-cadherin. J Cell Sci 107 (Pt 12): 3315-24.

Martin, D. S., J. R. Bertino and J. A. Koutcher (2000). ATP depletion + pyrimidine depletion can markedly enhance cancer therapy: fresh insight for a new approach. Cancer Res 60(24): 6776-83.

Martin, D. S. and G. K. Schwartz (1997). Chemotherapeutically induced DNA damage, ATP depletion, and the apoptotic biochemical cascade. Oncol Res 9(1): 1-5.

Massey, B. S. (1971). Mechanics of fluids. London, Van Nostrand Reinhold (UK).

Mehta, D. and A. B. Malik (2006). Signaling mechanisms regulating endothelial permeability. Physiol Rev 86(1): 279-367.

Meyer, T. N., C. Schwesinger, J. M. Ye, B. M. Denker and S. K. Nigam (2001). Reassembly of the tight junction after oxidative stress depends on tyrosine kinase activity. Journal of Biological Chemistry 276(25): 22048.

Michel, C. C. and F. E. Curry (1999). Microvascular permeability. Physiol Rev 79(3): 703-61.

Michel, C. C., J. C. Mason, F. E. Curry, J. E. Tooke and P. J. Hunter (1974). A development of the Landis technique for measuring the filtration coefficient of

individual capillaries in the frog mesentery. Q J Exp Physiol Cogn Med Sci 59(4): 283-309.

Mimura, K., F. Umeda, T. Yamashita, K. Kobayashi, T. Hashimoto and H. Nawata (1995). Effects of glucose and an aldose reductase inhibitor on albumin permeation through a layer of cultured bovine vascular endothelial cells. Horm Metab Res 27(10): 442-6.

Mohan, S., R. L. Reddick, N. Musi, D. A. Horn, B. Yan, T. J. Prihoda, M. Natarajan and S. L. Abboud-Werner (2008). Diabetic eNOS knockout mice develop distinct macro- and microvascular complications. Lab Invest 88(5): 515-28.

Molnar, J., S. Yu, N. Mzhavia, C. Pau, I. Chereshnev and H. M. Dansky (2005). Diabetes induces endothelial dysfunction but does not increase neointimal formation in high-fat diet fed C57BL/6J mice. Circ Res 96(11): 1178-84.

Najemnik, C., H. Sinzinger and H. Kritz (1999). Endothelial dysfunction, atherosclerosis and diabetes. Acta Med Austriaca 26(5): 148-53.

National Institute of Diabetes and Digestive and Kidney Diseases, N. I. o. H. (01/07/2005). National Diabetes Statistics, National Diabetes Information Clearinghouse

1 Information Way

Bethesda, MD 20892–3560

Phone: 1–800–860–8747

Fax: 703–738–4929.

Nerlich, A. G., H. G. Hagedorn, M. Boheim and E. D. Schleicher (1998). Patients with diabetes-induced microangiopathy show a reduced frequency of carcinomas. In Vivo 12(6): 667-70.

Nicholls, D. G. and S. L. Budd (1998). Mitochondria and neuronal glutamate excitotoxicity. Biochim Biophys Acta 1366(1-2): 97-112.

Nielsen, S., B. L. Smith, E. I. Christensen and P. Agre (1993). Distribution of the aquaporin CHIP in secretory and resorptive epithelia and capillary endothelia. Proc Natl Acad Sci U S A 90(15): 7275-9.

Nielsen, S., B. L. Smith, E. I. Christensen, M. A. Knepper and P. Agre (1993). CHIP28 water channels are localized in constitutively water-permeable segments of the nephron. J Cell Biol 120(2): 371-83.

Nishikawa, T., D. Edelstein, X. L. Du, S. Yamagishi, T. Matsumura, Y. Kaneda, M. A. Yorek, D. Beebe, P. J. Oates, H. P. Hammes, I. Giardino and M. Brownlee (2000). Normalizing mitochondrial superoxide production blocks three pathways of hyperglycaemic damage. Nature 404(6779): 787-90.

Noll, T., A. Muhs, M. Besselmann, H. Watanabe and H. M. Piper (1995). Initiation of Hyperpermeability in Energy-Depleted Coronary Endothelial Monolayers. American Journal of Physiology-Heart and Circulatory Physiology 37(4): H1462.

Okuda, T. and T. Yamamoto (1983). The ultrastructural basis of the permeability of arterial endothelium to horseradish peroxidase. Freeze-fracture and tracer studies of rat thoracic aorta and basilar artery. Cell Tissue Res 231(1): 117-28.

Osborn, E. A., A. Rabodzey, C. F. Dewey, Jr. and J. H. Hartwig (2006). Endothelial actin cytoskeleton remodeling during mechanostimulation with fluid shear stress. Am J Physiol Cell Physiol 290(2): C444-52.

Pacher, P. and C. Szabo (2005). Role of Poly(ADP-Ribose) Polymerase-1 Activation in the Pathogenesis of Diabetic Complications: Endothelial Dysfunction, as a Common Underlying Theme. Antioxid Redox Signal 7(11-12): 1568-80.

Pettitt, A. R., A. R. Clarke, J. C. Cawley and S. D. Griffiths (1999). Purine analogues kill resting lymphocytes by p53-dependent and -independent mechanisms. Br J Haematol 105(4): 986-8.

Popov, D. and M. Simionescu (2006). Cellular mechanisms and signalling pathways activated by high glucose and AGE-albumin in the aortic endothelium. Arch Physiol Biochem 112(4-5): 265-73.

Renkin, E. M., C. C. Michel and S. R. Geiger (1984). Microcirculation Charles Michel ; executive editor, Stephen R. Geiger. Bethesda, Md., American Physiological Society.

Rosamond, W., K. Flegal, K. Furie, A. Go, K. Greenlund, N. Haase, S. M. Hailpern, M. Ho, V. Howard, B. Kissela, S. Kittner, D. Lloyd-Jones, M. McDermott, J. Meigs, C. Moy, G. Nichol, C. O'Donnell, V. Roger, P. Sorlie, J. Steinberger, T. Thom, M. Wilson and Y. Hong (2008). Heart disease and stroke statistics--2008 update: a report from the American Heart Association Statistics Committee and Stroke Statistics Subcommittee. Circulation 117(4): e25-146.

Russell, J. W., D. Golovoy, A. M. Vincent, P. Mahendru, J. A. Olzmann, A. Mentzer and E. L. Feldman (2002). High glucose-induced oxidative stress and mitochondrial dysfunction in neurons. Faseb J 16(13): 1738-48.

Scalia, R., Y. Gong, B. Berzins, L. J. Zhao and K. Sharma (2007). Hyperglycemia is a major determinant of albumin permeability in diabetic microcirculation: the role of mu-calpain. Diabetes 56(7): 1842-9.

Sharma, S. D., B. N. Pandey, K. P. Mishra and S. Sivakami (2002). Amadori product and age formation during nonenzymatic glycosylation of bovine serum albumin in vitro. J Biochem Mol Biol Biophys 6(4): 233.

Sheetz, M. J. and G. L. King (2002). Molecular understanding of hyperglycemia's adverse effects for diabetic complications. Jama 288(20): 2579-88.

Sheline, C. T., H. Wang, A. L. Cai, V. L. Dawson and D. W. Choi (2003). Involvement of poly ADP ribosyl polymerase-1 in acute but not chronic zinc toxicity. Eur J Neurosci 18(6): 1402-9.

Shtridelman, Y., T. Cahyuti, B. Townsend, D. Dewitt and J. C. Macosko (2008). Force-Velocity Curves of Motor Proteins Cooperating In Vivo. Cell Biochem Biophys.

Sill, H. W., Y. S. Chang, J. R. Artman, J. A. Frangos, T. M. Hollis and J. M. Tarbell (1995). Shear stress increases hydraulic conductivity of cultured endothelial monolayers. Am J Physiol 268(2 Pt 2): H535-43.

Smaje, L., B. W. Zweifach and M. Intaglietta (1970). Micropressures and capillary filtration coefficients in single vessels of the cremaster muscle of the rat. Microvasc Res 2(1): 96-110.

Soriano, F. G., P. Pacher, J. Mabley, L. Liaudet and C. Szabo (2001). Rapid reversal of the diabetic endothelial dysfunction by pharmacological inhibition of poly(ADP-ribose) polymerase. Circ Res 89(8): 684-91.

Stemerman, M. B., E. M. Morrel, K. R. Burke, C. K. Colton, K. A. Smith and R. S. Lees (1986). Local variation in arterial wall permeability to low density lipoprotein in normal rabbit aorta. Arteriosclerosis 6(1): 64-9.

Sugihara-Seki, M. and B. Fu (2005). Blood flow and permeability in microvessels. Fluid Dynamics Research 37((2005)): 82-132.

Sussman, I., M. P. Carson, V. Schultz, X. P. Wu, A. L. McCall, N. B. Ruderman and K. Tornheim (1988). Chronic exposure to high glucose decreases myo-inositol in cultured cerebral microvascular pericytes but not in endothelium. Diabetologia 31(10): 771-5.

Suttorp, N., T. Hessz, W. Seeger, A. Wilke, R. Koob, F. Lutz and D. Drenckhahn (1988). Bacterial exotoxins and endothelial permeability for water and albumin in vitro. Am J Physiol 255(3 Pt 1): C368-76.

Suzuki, S., Y. Hinokio, K. Komatu, M. Ohtomo, M. Onoda, S. Hirai, M. Hirai, A. Hirai, M. Chiba, S. Kasuga, H. Akai and T. Toyota (1999). Oxidative damage to mitochondrial DNA and its relationship to diabetic complications. Diabetes Res Clin Pract 45(2-3): 161-8.

Szabo, C. (2005). Roles of poly(ADP-ribose) polymerase activation in the pathogenesis of diabetes mellitus and its complications. Pharmacol Res 52(1): 60-71.

Tarbell, J. M. (2003). Mass Transport in Arteries and the Localization of Atherosclerosis. Palo Alto, CA, Annual Reviews Inc.

Tarbell, J. M., M. J. Lever and C. G. Caro (1988). The effect of varying albumin concentration of the hydraulic conductivity of the rabbit common carotid artery. Microvasc Res 35(2): 204-20.

Tedgui, A. and M. J. Lever (1984). Filtration through damaged and undamaged rabbit thoracic aorta. Am J Physiol 247(5 Pt 2): H784-91.

Terminella, C., K. Tollefson, J. Kroczynski, J. Pelli and M. Cutaia (2002). Inhibition of apoptosis in pulmonary endothelial cells by altered pH, mitochondrial function, and ATP supply. Am J Physiol Lung Cell Mol Physiol 283(6): L1291-302.

Tesfamariam, B. (1994). Free radicals in diabetic endothelial cell dysfunction. Free Radic Biol Med 16(3): 383-91.

Truskey, G. A., W. L. Roberts, R. A. Herrmann and R. A. Malinauskas (1992). Measurement of endothelial permeability to 125I-low density lipoproteins in rabbit arteries by use of en face preparations. Circ Res 71(4): 883-97.

Turner, M. R. (1992). Flows of liquid and electrical current through monolayers of cultured bovine arterial endothelium. J Physiol 449: 1-20.

Unno, N., M. J. Menconi, A. L. Salzman, M. Smith, S. Hagen, Y. M. Ge, R. M. Ezzell and M. P. Fink (1996). Hyperpermeability and ATP depletion induced by chronic hypoxia or glycolytic inhibition in Caco-2BBe monolayers. American Journal of Physiology-Gastrointestinal and Liver Physiology 33(6): G1010.

Waharte, F., C. M. Brown, S. Coscoy, E. Coudrier and F. Amblard (2005). A two-photon FRAP analysis of the cytoskeleton dynamics in the microvilli of intestinal cells. Biophys J 88(2): 1467-78.

Watanabe, H., W. Kuhne, R. Spahr, P. Schwartz and H. M. Piper (1991). Macromolecule permeability of coronary and aortic endothelial monolayers under energy depletion. Am J Physiol 260(4 Pt 2): H1344-52.

Weiderpass, E., W. Ye, H. Vainio, R. Kaaks and H. O. Adami (2002). Reduced risk of prostate cancer among patients with diabetes mellitus. Int J Cancer 102(3): 258-61.

Weinbaum, S., P. Ganatos, R. Pfeffer, G. B. Wen, M. Lee and S. Chien (1988). On the time-dependent diffusion of macromolecules through transient open junctions and their subendothelial spread. I. Short-time model for cleft exit region. J Theor Biol 135(1): 1-30.

Wieser, W. and G. Krumschnabel (2001). Hierarchies of ATP-consuming processes: direct compared with indirect measurements, and comparative aspects. Biochem J 355(Pt 2): 389-95.

Williamson, J. R., K. Chang, M. Frangos, K. S. Hasan, Y. Ido, T. Kawamura, J. R. Nyengaard, M. van den Enden, C. Kilo and R. G. Tilton (1993). Hyperglycemic pseudohypoxia and diabetic complications. Diabetes 42(6): 801-13.

Wilson, J., M. Winter and D. M. Shasby (1990). Oxidants, ATP depletion, and endothelial permeability to macromolecules. Blood 76(12): 2578-82.

Wu, S., H. Chen, M. F. Alexeyev, J. A. King, T. M. Moore, T. Stevens and R. D. Balczon (2007). Microtubule motors regulate ISOC activation necessary to increase endothelial cell permeability. J Biol Chem 282(48): 34801-8.

Wysolmerski, R. B. and D. Lagunoff (1988). Inhibition of endothelial cell retraction by ATP depletion. Am J Pathol 132(1): 28-37.

Yang, N. C., W. M. Ho, Y. H. Chen and M. L. Hu (2002). A convenient one-step extraction of cellular ATP using boiling water for the luciferin-luciferase assay of ATP. Anal Biochem 306(2): 323-7.

Yao, Y., A. Rabodzey and C. F. Dewey, Jr. (2007). Glycocalyx modulates the motility and proliferative response of vascular endothelium to fluid shear stress. Am J Physiol Heart Circ Physiol 293(2): H1023-30.

Zhang, X., R. H. Adamson, F. R. Curry and S. Weinbaum (2006). A 1-D model to explore the effects of tissue loading and tissue concentration gradients in the revised Starling principle. Am J Physiol Heart Circ Physiol 291(6): H2950-64.

Zimmerman, M. and J. McGeachie (1986). Quantitation of the relationship between aortic endothelial intercellular cleft morphology and permeability to albumin. Atherosclerosis 59(3): 277-82.

Zong, W. X., D. Ditsworth, D. E. Bauer, Z. Q. Wang and C. B. Thompson (2004). Alkylating DNA damage stimulates a regulated form of necrotic cell death. Genes Dev 18(11): 1272-82.

Zweifach, B. W. (1971). Local regulation of capillary pressure. Circ Res 28: Suppl 1:129+.